TECHNISCHE UNIVERSITÄT DRESDEN

School of Science, Faculty of Chemistry and Food Chemistry

ELECTROCHEMICAL AND STRUCTURAL INVESTIGATIONS OF A LAYERED AU,PT-YSZ MIXED POTENTIAL GAS SENSING ELECTRODE

DISSERTATION

For obtainment of academic degree

DOCTOR RERUM NATURALIUM
(DR. RER. NAT.)

Submitted to

School of Science, Dresden University of Technology

By

M.Sc. Zhang, Xin

Born on 23.10.1984 in Yunnan, PR. China

Supervisor: Prof. Dr.rer.nat. habil. Ulrich Guth
Prof. Dr.rer.nat. Heinz Kohler

Date of submission: 12.02.2019
Date of defense: 28.08.2019

.....
Signature of Doctoral candidate

Bibliographic certificate

Zhang, Xin

ELECTROCHEMICAL AND STRUCTURAL INVESTIGATIONS OF A LAYERED AU,PT-YSZ MIXED POTENTIAL GAS SENSING ELECTRODE

Year – 2019 Pages – 89 Appendix – 5

Dissertation

Technische Universität Dresden
Faculty of Chemistry and Food Chemistry

CONTENTS

LIST OF TABLES

LIST OF FIGURES

LIST OF SYMBOLS

YSZ	Yttrium stabilized Zirconia
HCs	Hydrocarbons
$VOCs$	Volatile organic compounds
O^{2-}	Oxide ion
$O^{\delta-}$	Spillover oxygen
j_{CO}	Anodic current density for electrochemical oxidation of CO
j_{CO}^{0}	CO conc. dependent exchange current density
B_1	Gas species (CO) dependent constant
m	Gas concentration (CO) related constant
C_{CO}	CO concentration
α_1	Transfer coefficient for CO electrochemical oxidation
φ	Electrode potential
φ_{CO}^{0}	Electrode potential at CO thermodynamic equilibrium
j_{O_2}	Cathodic current density for Oxygen reduction reaction
$j_{O_2}^{0}$	O_2 conc. dependent exchange current density
B_2	Gas species (O_2) dependent constant
n	Gas concentration (O_2) related constant
C_{O_2}	O_2 concentration
α_2	Transfer coefficient for O_2 reduction reaction
$\varphi_{O_2}^{0}$	Electrode potential at O_2 thermodynamic equilibrium
F	Faraday constant
R	Molar gas constant
T	Temperature
φ_m	Mixed-potential
A	Transfer coefficient related constant
φ_o'	Mixed-potential constant under fixed O_2 conc.
φ_o''	Mixed-potential constant under fixed CO conc.
D_{CO}	CO diffusion coefficient
δ	Diffusion boundary layer thickness
i_{CO}	Anodic current for electrochemical oxidation of CO
i_{O_2}	Cathodic current for Oxygen reduction reaction

$j_{CO}^{x_1}$	Anodic current density for EOC at depth x_1
$i_{CO}^{x_1}$	Anodic current for EOC at depth x_1
$j_{O_2}^{x_1}$	Cathodic current density for ORR at depth x_1
$i_{O_2}^{x_1}$	Cathodic current for ORR at depth x_1
$i_{net}^{x_1}$	Net exchange current at depth x_1
$i_{CO}^{x_2}$	Anodic current for EOC at depth x_2
$i_{O_2}^{x_2}$	Cathodic current for ORR at depth x_2
$i_{net}^{x_2}$	Net exchange current at depth x_2
$i_{CO}^{x_3}$	Anodic current for EOC at depth x_3
$i_{O_2}^{x_3}$	Cathodic current for ORR at depth x_3
$i_{net}^{x_3}$	Net exchange current at depth x_3
$i_{CO}^{x_n}$	Anodic current for EOC at depth x_n
$i_{O_2}^{x_n}$	Cathodic current for ORR at depth x_n
$i_{net}^{x_n}$	Net exchange current at depth x_n
i'_{net}	Overall net exchange current at the APE
i_{ORR}^{A}	Cathodic current for ORR at point A
i_{ORR}^{B}	Cathodic current for ORR at point B
i_{ORR}^{C}	Cathodic current for ORR at point C
i_{OER}^{D}	Cathodic current for OER at point D
i_{OER}^{E}	Cathodic current for OER at point E
i_{OER}^{F}	Cathodic current for OER at point F
k_{ε}	Forward rate constant of thermo-dynamic reaction of oxygen
$k_{-\varepsilon}$	Backward rate constant of thermo-dynamic reaction of oxygen
a_O	Surface oxygen activity on APE
a_{σ}	Vacant site activity on APE

LIST OF REACTIONS & EQUATIONS

LIST OF ABBREVIATIONS

APE	Layered Au,Pt-YSZ electrode
CGR	Carbon monoxide gas phase reaction
conc.	Concentration
CV	Cyclic voltammetry
EIS	Electrochemical impedance spectroscopy
EOC	Electrochemical oxidation of Carbon monoxide
Expr.	Expression
Eq.	Equation
ESEM	Environmental scanning electron microscopy
GD-OES	Glow-discharge optical emission spectroscopy
LEES	Liquid electrolyte based electrochemical systems
MPE	Mixed potential electrode
OCP	Open-circuit potentiometry / open-circuit potential
OER_{CV}	Oxygen evolution process occurring in CV
ORR	Oxygen reduction reaction
ORR_{CV}	Oxygen reduction process occurring in CV
RE	Reference electrode
SE	Sensing electrode
SEES	Solid state electrochemical systems
SOEC	Solid oxide electrolysis cell
SOFC	Solid oxide fuel cell
TPB	Triple phase boundary
XRD	X-ray crystallography

ACKNOWLEDGEMENTS

First of all, I would like to express my sincere gratitude to my supervisors Prof. Dr. habil. Ulrich Guth and Prof. Dr. Heinz Kohler for giving me the opportunity to do my doctorate under their guidance, and for their continuous support of my research work. Their patient, motivating and encouraging guidance helped me in all the time of research and writing of this dissertation. I could not have imagined having better supervisors for my Ph.D study, and would never forget those interesting and helpful discussions with them and their insightful and inspiring comments/suggestions during my Ph.D research work.

In addition, a special gratitude to the previous and the current ISIS-sensor group colleagues: Dr. Navas Illyaskutty, Mr. Binayak Ojha, Mr. Jens Knoblauch, Mr. Nils Donker and so on. It was fantastic to work with these fellow lab-mates over the past years. Thank you for the stimulating discussions and for all the fun we have had in the last several years.

Many sincere thanks also goes to Dr. Matthias Schwotzer, Ms. Yanhong Wu, Dr. Jens Zosel, Dr. Frank Hammer and Dr. Marko Völkel, who gave access to their laboratory and research facilities. Without their precious support it would not be possible to conduct all of this research.

A special gratitude goes to Friedrich und Elisabeth Boysen-foundation, Karlsruhe University of Applied Sciences, LAMTEC Meß- und Regeltechnik für Feuerungen GmbH & Co KG and Hybrid sensor net e.V. for helping and providing financial support for this work.

Last but not the least, I am deeply grateful to my parents, my wife, my daughter and generally my families for their loving considerations, great confidence in me and supports in all means all through these years.

Zhang Xin

Karlsruhe, 12.02.2019

1. INTRODUCTION

1.1 Background

Solid electrolyte based gas sensors have been extensively studied over the last five decades, especially with growing concerns to environmental issues, for example the exhaust pollutants from industries, automobiles and even domestic wood-fueled fireplaces [1-15]. The sensors used in most of these applications are based on thermodynamic principle. Their signals obey the Nernstian relation in a wide range of temperature (400 to 1600 °C) and oxygen partial pressure (10 to 10^{-20} bar). Therefore this type of sensors is also named as Nernstian sensors [16-19].

Among the various gas sensors, the group of devices based on the kinetics determined mixed-potential mechanism has attracted particular attention due to its promising features related to analysis of combustible gas components in high-temperature applications. In difference to the mixed-potentials measured at electrodes in liquid electrolyte based electrochemical systems, those established at electrodes in YSZ solid electrolyte based electrochemical systems are found to be very stable. A mixed potential sensor combines an oxygen electrode as a reference (equilibrium electrode) and a second electrode, which shows a low oxygen sensitivity but a high sensitivity to combustibles (non-equilibrium electrode). It is generally believed that the chemisorption of oxygen which is the first step in electrochemical reaction occurs on the reference electrode with a high rate, but it is hindered on the mixed potential electrode.

Various groups of researchers have exerted a lot of efforts in developing mixed potential type gas sensors based on Yttrium Stabilized Zirconia (YSZ) with special focus on electrode materials and made significant progress in achieving high performance of such type of sensors. The status of research was reviewed in [20-23]. It was shown, that the response behavior of this type of sensor is highly influenced by choice of the material of the mixed potential electrode (MPE) and its morphological structure, thermal stability and catalytic activity [24-49]. For simplification instead of the term ‘non-equilibrium electrode’, the abbreviation ‘MPE’ will be used in this work with the consideration that the mixed potential is a result of both the anodic and cathodic processes at the electrode. In the early developments, noble metals like Pt or transition metals like Mo, and noble metal alloys such as Pt/Au, Pt/Ag, Pt/Rh, Pt/Cu and Pt/Ni were adopted for detection of CO and HCs [24, 25]. However, due to the recrystallization of the noble metals and noble metal alloys at elevated temperatures and the change of their catalytic properties by irreversible gas reactions (poisoning), the long term stability of the MPEs is not satisfying [22, 27, 50]. To achieve better long term stability, oxides of different kinds, for example spinel-type oxides ($CdMn_2O_4$, chromites), perovskite-type oxides (La_{1-x} $Sr_xCr_{1-y}Ga_yO_{3-\delta}$ with x= 0...0.02 and y= 0...0.3), SnO_2, Ta_2O_5, Nb_2O_5, CeO_2, and many other oxides [28-34, 38, 51] were attempted to be used as materials for MPE. Since then, substantial development of this type of gas sensors has been achieved.

In recent developments of this type of sensors, the combination of Au/AuPt-alloy and oxides was found to be a promising MPE material. With this kind of material combination, satisfactory sensing characteristics were achieved using different kinds of electrode design [26-31, 43, 44, 48, 52-55]. Guth et al. and Ueda et al. reported uniformly admixed Au-oxide composites as mixed potential electrodes for sensing of carbon monoxide, propane, propene or toluene, separately [28-31, 53]. A broad range of oxides, including Ga_2O_3, Y_2O_3, Al_2O_3, ZrO_2, In_2O_3, Ta_2O_5, Nb_2O_5, CeO_2, Gd_2O_3, La_2O_3, Pr_6O_{11}, Sm_2O_3 and so on, has been examined as the oxide additions of the composited electrodes. According to their results, the sensing behavior of such type of electrodes was found to be mainly determined by the following two factors: i) the electrode morphology, which is strongly influenced by the kind of the oxide addition, and ii) the corresponding catalytic activity of the composited electrode material for chemical oxidation processes within the electrode layer [56] and/or electrochemical reactions proceeding at the triple phase boundary (TPB).

Moreover, it was found by Viricelle et al. [54] that the addition of YSZ in the Au electrode could improve the sensing performance of the electrode compared to the pure Au electrode in terms of the response time and the sensitivity to NO_2 between 450 and 550 °C. This improvement of the sensing performance was accompanied by a decreased polarization resistance in air characterized by electrochemical impedance spectroscopy [54]. It was assumed that the addition of YSZ prevent the agglomeration of gold and consequently stabilize the morphology of the electrode. Moreover, an AuPt alloy material by surface modification with ZrO_2 nanoparticles was also reported to be optimal for NO_2 sensing at elevated temperatures. The sensitivity to NO_2 was highly dependent on the Au/Pt ratio, and the maximum was found for the composite consisting of 85 % Au and 15 % Pt [55].

In addition to those Au/AuPt alloy-oxide composites with uniform material distribution as mentioned above, Breedon et al. investigated the effect of a micro-dimensional Au mesh addition on the gas sensitivity of a screen printed Pt electrode patterned onto yttria-stabilized-zirconia [26]. This kind of electrode, combining the Au mesh and the Pt electrode, shows a non-uniform material distribution with respect to the Au/Pt ratio, which is clearly different to the AuPt alloy electrode reported in [55]. However, a mixed-potential characteristic was still observed at the Pt(+Au mesh) electrode under exposure to H_2 at 550 °C, and the sensing performance could be further improved by coating the entire electrode structure with YSZ.

In spite of those encouraging experimental results, the role of Au addition which is well known as a CO oxidation catalyst [57-59], especially its effect on the electrode processes contributing to the mixed potential formation, has not yet been fully understood. Detailed insights regarding the influence of Au on the electrochemical behavior of metal+oxide-MPEs would be beneficial for better understanding the sensing behavior of such type of sensors, and for achieving further technological improvements in the future.

In order to clarify the mechanism of the electrode reaction, most investigations in the past were focused on the measurement of the mixed potential. However, this value is only a general result of the underlying complicated mechanisms of potential formation which have to be disclosed by further electrochemical investigations. Although Au-oxide composites and Au,Pt alloy/composites were often studied as an electrode material [54, 55, 60], the ratio Au/Pt, i.e. how much gold is needed in order to suppress the oxygen reaction and/or to promote the reaction with combustibles on the electrode, is still unknown. Moreover in case of the Au,Pt-YSZ electrode with non-uniformly distributed material [26], the effects of Au distribution on the sensing characteristics of the electrode are needed to be further investigated and clarified as well.

On the other hand, O_2,Pt/YSZ, as one of the simplest and best-characterized model-type electrode systems in solid state electrochemistry, has been widely investigated in many aspects [61-78]. These studies bring an in-depth understanding of this kind of solid state gas electrode. One of the major concerns in the investigations is the mechanism of the electrochemical oxygen exchange reaction at the O_2,Pt/YSZ electrode system due to its fundamental relevance and crucial importance in scientific and technological applications. Most prominent examples are solid oxide fuel cells (SOFCs), solid oxide electrolysis cells (SOECs), oxygen sensors and the non-faradic electrochemical modification of catalytic activity in catalysis [79-85]. Dissociative adsorption of oxygen on the Pt surface, surface diffusion of atomic oxygen, and charge transfer reactions at the TPB have been taken into account in the clarification of the oxygen exchange mechanism [86, 87].

Despite of those outstanding research efforts in the past, changes at the O_2,Pt/YSZ electrode system during electrochemical operations or aging processes at elevated temperatures are still crucial questions not fully clarified and needed to be further investigated [61, 64, 73, 77, 88-90], since they significantly influence the catalytic and electrochemical characteristics of the electrode. These changes include: i) irreversible processes, which are related to the accumulation/agglomeration of impurities and the corresponding segregation of the TPB; ii) reversible processes, which are attributed to the formation/decomposition of a Platinum oxide (PtO_x) 'phase'. In particular, the mechanism of PtO_x formation/decomposition is systematically studied by combining different kinds of electrochemical methods and in-situ/ex-situ surface analytical approaches [61, 64, 73, 77, 88]. Different regions within the electrode system including: i) the interface Pt/YSZ, ii) the TPB O_2/Pt/YSZ, and iii) the Pt surface, i.e. the interface Pt/O_2, have been considered and discussed for potential PtO_x formation [61, 64, 73, 88]. The formation of PtO_x (reaction (1)) is found to be favored under the condition of anodic polarization, and its amount depends strongly on temperature, oxygen partial pressure and oxygen flux towards the electrode during polarization.

$$Pt + xO^{2-} \xrightarrow{anod.\ pol.} PtO_x + 2xe^- \quad (1)$$

$$PtO_x + 2xe^- \xrightarrow{cath.pol.} Pt + xO^{2-} \quad (2)$$

On the other hand, the cathodic polarization is demonstrated to be able to promote an electrochemical reduction of the pre-formed PtO_x (reaction (2)) [64, 88]. The formation/decomposition of PtO_x can significantly change the catalytic properties and kinetics of the O_2,Pt/YSZ electrode, and accordingly affect the electrochemical processes proceeding at the electrode.

Similar changes may probably occur at the Pt-YSZ based MP electrode modified by Au addition as well. These changes of the micro- and nano-structure of the electrode, especially the ones induced by thermal treatment during aging processes at elevated temperatures, can be of high relevance with long-term sensing stability of this kind of electrode. Besides, the kind of structural changes caused by electrochemical operation is also expected to change the catalytic properties and electrochemical characteristics of the electrode, and accordingly influence its gas sensing behaviors. However, these correlations between these changes induced by thermal treatment or electrochemical operation and the sensing characteristics were rarely investigated in the field of mixed potential type gas sensors in the past.

Except for those material scientific and engineering studies on mixed-potential type gas sensors stated above, the investigations reported in [51, 91, 92] reveal that the operating temperature of such kind of sensors also plays an important role on the sensing performances. The potential difference ΔU between mixed-potential electrode and reference electrode, response time and sensitivity typically depend on both, the electrode material and the operating temperature [51, 92]. By using these temperature-dependent features, Mori et al. have proposed a method to discriminate various volatile organic compounds (VOCs) using a set of ΔU-data measured isothermally at different temperatures [91].

So far, numerous investigations have been carried out to study the response behaviors of mixed-potential type gas sensors at isothermal operation [30, 93-96]. However, only some of those research activities emphasized the influence of temperature on the sensing performances at several discrete temperatures [95, 96] and nearly no results of the sensor response at continuous temperature variation are available in literature. On the other hand, temperature dependent dynamic sensor responses of SnO_2 based semiconductor sensors have been successfully utilized in the past to realize gas species identification in combination with numerical analysis [97-100]. It is expected that mixed potential gas sensors show gas component specific responses as well because of the specific electrode processes at continuous variation of temperature. Especially In addition to those investigations on mixed potential gas sensors under steady state conditions, dynamic methods, which means time dependent change in temperature or electrical polarization on the electrode, open up new possibilities to enhance the sensitivity and selectivity of such type of sensors.

1.2 Outline

In this work, the role of gold in gold-platinum admixture based mixed potential electrodes will be studied. For that purpose, layered Au,Pt-YSZ mixed potential gas sensing electrodes are going to be investigated by combining different kinds of electrochemical methods and material analytical approaches, in order to achieve a better understanding and a deeper insight of the following aspects, as illustrated below (Fig. 1):

- The role of Au on the mixed-potential formation at the layered Au,Pt-YSZ electrodes with non-uniform material distribution, i.e. the correlations between the electrochemical characteristics of the electrode and its material properties
- The Influence of temperature and different gas atmospheres on the electrochemical (Open Circuit Potential, Cyclic Voltammetry and Electrochemical Impedance Spectroscopy) characteristics of the electrode under isothermal operation
- The behaviors of the electrodes under dynamic conditions, i.e. time dependent change in temperature or electrical polarization on the electrodes, for gaining better sensing characteristics.
- The effects of the high temperature aging process and the electrochemical treatment on the electrochemical characteristics of the electrode

The morphological and structural properties of the layered Au,Pt-YSZ electrodes prepared under different conditions in terms of the Au layer thickness and the sintering temperature of the electrode are going to be studied by environmental scanning electron microscopy (ESEM), X-ray diffraction crystallography (XRD) and glow-discharge optical emission spectroscopy (GD-OES), and correlated with open-circuit potential (OCP) measurements under CO exposures and cyclic voltammetry (CV) measurements in synthetic air at 600 °C. Based on these results, a qualitative model is proposed to interpret the sensing mechanism of the layered Au,Pt-YSZ electrodes.

After that, at a selected temperature (600 °C), the sensors are going to be further investigated by CV and EIS measurements under exposure to various gas atmospheres with different CO and O_2 concentrations. By analysis of these dynamic electrochemical characteristics of the sensors, the electrode processes involved in the mixed potential formation and their possible interactions under electrical polarization conditions are then discussed and elucidated.

In order to study the influences of temperature, additional electrochemical investigations including OCP, CV and electrochemical impedance spectroscopy (EIS) measurements will be carried out in an extended temperature range from 500 °C – 700 °C, while the sensors are operated under isothermal condition. The OCP sensing responses at elevated temperatures are correlated with the corresponding dynamic electrochemical behaviors (CV and EIS characteristics) of the sensors

characterized under the same temperatures. Moreover, the OCP response behaviors are going to be studied under thermo-cyclic operation as well.

With regard to the high temperature aging effect, OCP and EIS measurements are firstly conducted on freshly fabricated sensors. After the aging process, the OCP and EIS behaviors of the same individuals are then comparatively studied under the same experimental conditions. This kind of comparative study of the OCP and EIS behaviors is later also applied to investigate the effect of cathodic polarization on the electrochemical characteristics of the sensors, especially in relation to the response sensitivity and long term stability. The differences in the OCP and EIS behaviors before and after the aging process and the cathodic polarization will be discussed in context with the irreversible/reversible changes at the TPB of the electrodes.

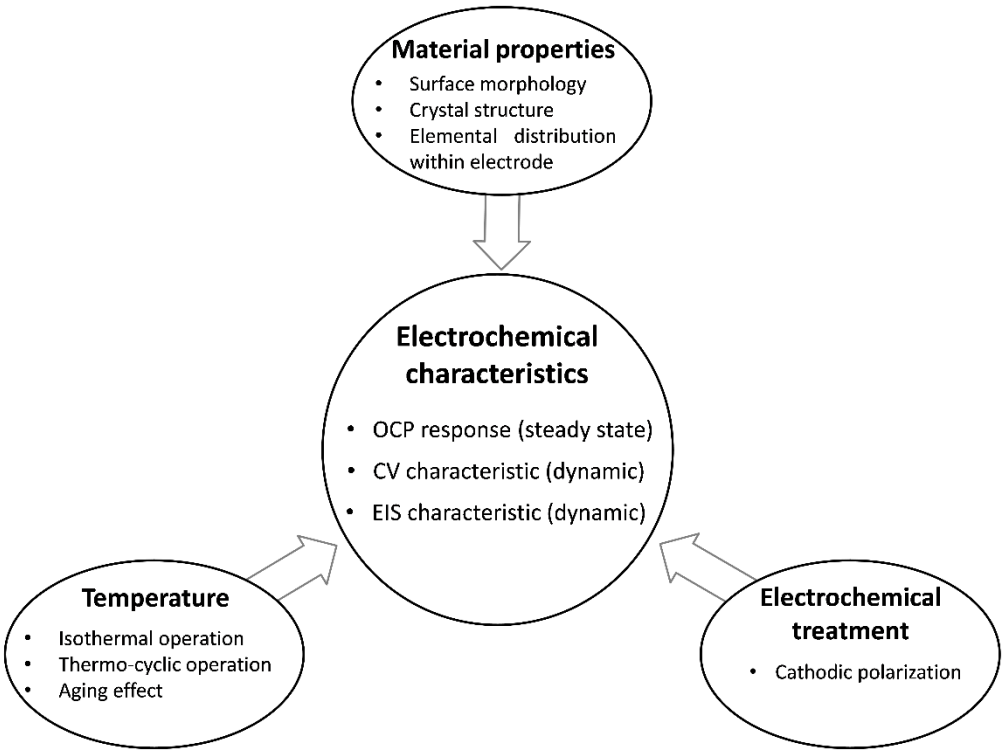

Fig 1: *Schematic representation of the scope of investigation*

2. THEORY OF MIXED-POTENTIAL FORMATION

Mixed potential theory is originally proposed in electrochemistry to describe generation of the interfacial potential at ion-selective membranes. It relates the potentials and currents from differing constituents to come up with a 'weighted' potential at zero net current, i.e. it is an electrode potential resulting from a simultaneous action of more than a single ionic exchange process across the interface, while the net electrode current is zero [101, 102]. The concept of mixed potential for YSZ based sensors was first introduced to explain non-ideal behavior of an oxygen sensor in the mixed gases of air and fuel at temperatures below 500 °C by Fleming [103]. A detailed theoretical model was later proposed by Miura [51] to interpret the sensing mechanism of YSZ based mixed-potential type gas sensors. For further elucidation of this model, we consider a simple case of a sensor that consists of a sensing (SE/MPE) and a reference electrode (RE) on a YSZ solid electrolyte exposed to a simple gas mixture, e.g. carbon monoxide of several hundred ppm in air (Fig. 2). Material composition is assumed to be uniformly distributed at the sensing/mixed-potential electrode stated above.

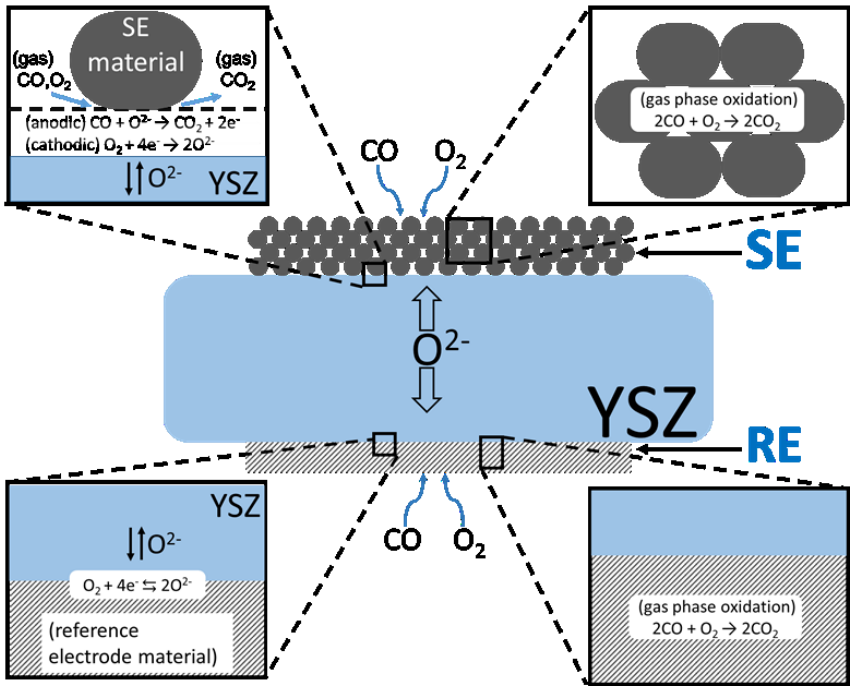

Fig. 2: *Illustration of the electrode processes contributing to the potential formation on the SE and the RE of a mixed-potential type gas sensor. Both electrodes are exposed to the same gas mixture containing CO, O_2 and N_2.*

The RE is routinely made of highly catalytic active materials, for example platinum (Pt). This means at elevated temperatures, the CO (several 100 ppm level) first reacts with the O_2 (vol.% level) via the gas phase reaction (3) (CGR) at/in the electrode layer forming a reaction equilibrium. The potential formed at the RE is determined by the thermodynamic equilibrium among the residual O_2 from the gas phase, the electrons from the RE and the O^{2-} ions from the YSZ according to the reaction (4)

proceeding at the triple phase boundary (TPB). Correspondingly, the potential is expected to show a Nernstian behavior at the RE/YSZ half-cell.

$$2CO + O_2 \rightarrow 2CO_2 \quad \text{(CGR)} \quad (3)$$

$$\frac{1}{2}O_2(g) + V_O^{\circ\circ}(YSZ) + 2e^-(electrode) \rightleftarrows O_O^x(YSZ) \quad (4)$$

However, the situation of potential formation at the SE is different. At this electrode the thermodynamic equilibrium of oxygen reaction (reaction (4)) is not achieved, and the electrode potential shows a non-Nernstian behavior. The half-cell potential is determined by an anodic reaction with CO (reaction (5)) and a cathodic reaction with O_2 (reaction (6)) occurring simultaneously at the TPB:

$$CO(g) + O_O^x(YSZ) \rightarrow CO_2(g) + V_O^{\circ\circ}(YSZ) + 2e^-(MPE) \quad \text{(EOC)} \quad (5)$$

$$\frac{1}{2}O_2(g) + V_O^{\circ\circ}(YSZ) + 2e^-(MPE) \rightarrow O_O^x(YSZ) \quad \text{(ORR)} \quad (6)$$

When the gas mixture composed of CO balanced with air flows over the SE, at first it penetrates the electrode layer, where part of CO reacts with the O_2 via the gas phase reaction (CGR) (reaction (3)). The residual CO together with the O_2/N_2 mixture then reaches the TPB, at which the electrochemical reactions (5) and (6) proceed and directly contribute to the potential formation. Under the zero current (i=0) condition the mixed potential of the half-cell represents the state, when the electron transfer rate of the electrochemical oxidation of CO (EOC, (3)) equals that of the oxygen reduction reaction (ORR, (6)). That is to say, the potential formed at the SE is determined by the balance of the rates of the CGR (3), the EOC (5) and the ORR (6) proceeding at different locations of the electrode.

The mixed potential formation can be quantitatively deduced as a function of CO and O_2 concentration according to the Butler-Volmer equation [20, 22, 38]. Under the assumption that the rate-determining steps are the kinetics of the electron transfer reactions (5) and (6), the corresponding current densities for the anodic (j_{CO}) and the cathodic (j_{O_2}) reaction can be expressed as following:

$$j_{CO} = j_{CO}^0 exp\{2\alpha_1 F(\varphi - \varphi_{CO}^0)/RT\} \quad (7)$$

$$j_{O_2} = j_{O_2}^0 exp\{-4\alpha_2 F(\varphi - \varphi_{O_2}^0)/RT\} \quad (8)$$

where φ is the electrode potential, F is the Faraday constant, R is the molar gas constant, T is the temperature in Kelvin, φ^o is the equilibrium electrode potential of the correspondingly involved reaction (5) or (6), j_{CO}^0 and $j_{O_2}^0$ are the corresponding exchange current densities and α is the transfer coefficient. The exchange current densities are assumed to obey the following kinetic relationships:

$$j_{CO}^0 = B_1 C_{CO}^m \quad (9)$$

$$j_{O_2}^0 = -B_2 C_{O_2}^n \quad (10)$$

where C signifies the concentration of CO and O_2, and B_1, B_2, m and n are constants. j_{CO}^{o} and j_{O_2} are opposite in sign, and the mixed-potential is derived by solving Eqs. (7) and (8) under the condition $|j_{CO}| = |j_{O_2}|$ or $j_{CO} + j_{O_2} = 0$, as depicted in Fig. 3a and given in Eq. (11)

$$\varphi_m = \varphi_o + \frac{nRT}{(4\alpha_2 + 2\alpha_1)F} \ln C_{O_2} - \frac{mRT}{(4\alpha_2 + 2\alpha_1)F} \ln C_{CO} \tag{11}$$

herewith,

$$\varphi_o = \frac{RT}{(4\alpha_2 + 2\alpha_1)F} \ln \frac{B_2}{B_1} + \frac{2\alpha_2 \varphi_{O_2}^0 + \alpha_1 \varphi_{CO}^0}{2\alpha_2 + \alpha_1} \tag{12}$$

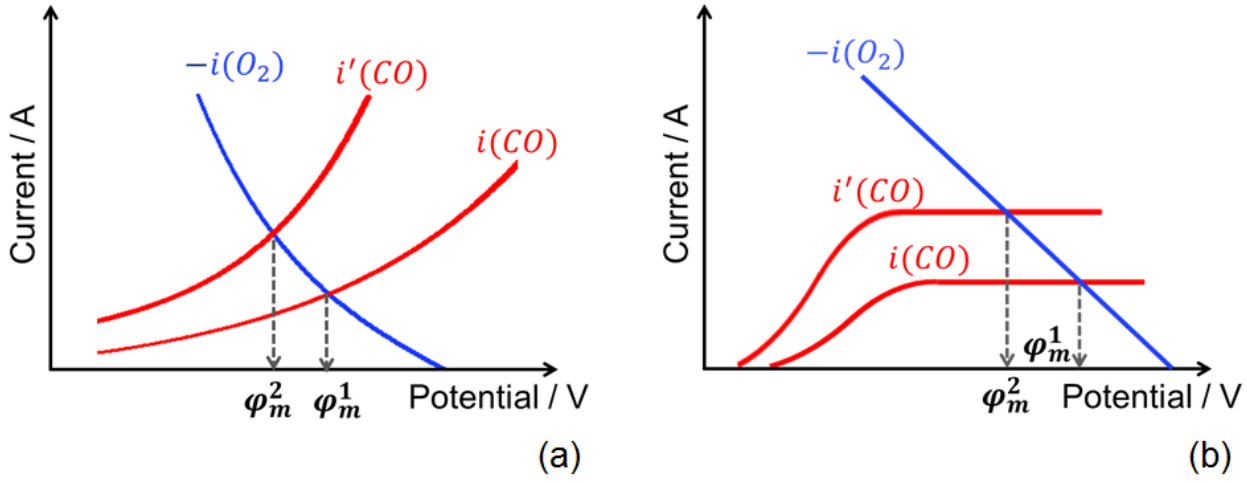

Fig. 3: *Illustration of (a) electron transfer reaction kinetics and (b) diffusional transport controlled mixed-potential formation*

The expression of mixed-potential as a function of CO and O_2 concentration can be simplified to Eq. (13):

$$\varphi_m = \varphi_o + nA \ln C_{O_2} - mA \ln C_{CO} \tag{13}$$

with,

$$A = \frac{RT}{(4\alpha_2 + 2\alpha_1)F} \tag{14}$$

Under the condition that the CO- or the O_2 concentration is kept constant, Eq. (13) is further simplified to either of the following equations:

$$\varphi_m = \varphi_o' - mA \ln C_{CO} \qquad (C_{O_2} constant) \tag{15}$$

$$\varphi_m = \varphi_o'' + nA \ln C_{O_2} \qquad (C_{CO}\ constant) \tag{16}$$

Where φ_o' and φ_o'' are constants.

These equations indicate that the yielding mixed potential is linearly related with the logarithmic variation of CO concentration under fixed oxygen concentration (Eq. (15)), or linearly related with the logarithmic variation of oxygen concentration under fixed CO concentration (Eq. (16)). The slope of

these correlations, namely $-mA$ or nA, are determined by the kinetic parameters such as α and m (or n).

However, taking the kinetics of the electron transfer reactions as the rate determining steps is not a necessary assumption in all cases of mixed potential formation. If CO is highly consumed via the gas phase reaction (CGR, reaction (3)) in the electrode layer (Fig. 2), the anodic current density for the EOC (reaction (5)) proceeding at the TPB may obey the following relationship in the case of a diffusion based mass transport limitation:

$$j_{CO} = 2FD_{CO}\frac{C_{CO}}{\delta} \tag{17}$$

where D_{CO} is the diffusion coefficient of carbon monoxide and δ is the diffusion boundary layer thickness [22]. In addition, if we further assume the mixed potential occurs at potentials near the equilibrium $\varphi^0_{O_2}$, the oxygen reduction kinetics may be represented by the low overpotential linear approximation of the Butler-Volmer equation:

$$j_{O_2} = j^0_{O_2} 4F(\varphi - \varphi^0_{O_2})/RT \tag{18}$$

Combining this linear oxygen reduction kinetics (Eq.(18)) with the diffusional mass transport limited EOC kinetics (Eq. (17)) under the equilibrium condition (Fig. 3b) yields [22]:

$$\varphi_m = \varphi^0_{O_2} - RT\frac{D_{CO}C_{CO}}{2B_2\delta C^n_{O_2}} \tag{19}$$

This indicates, the mixed-potential may also show a linear dependence on the CO concentration under fixed O_2 concentration (Eq. (19)), in case that the rate-determining process is the limitation of the CO transport to the TPB by diffusion and the oxygen reduction kinetics may be represented by the linear approximation of the Butler-Volmer equation at low overpotential.

The deduction of the mixed-potential stated above is based on the balance of the current densities for the two different kinds of electrochemical reactions occurring at the TPB. Following the assumption of the even distribution of electrode material, the anodic and the cathodic current densities are also evenly distributed along the TPB, which indicates the EOC (5) and the ORR (6) proceed at a uniform rate at different reaction sites, separately. Correspondingly, if we integrate the anodic current density for the EOC (5) and the cathodic current density for the ORR (6) over the whole area of the TPB (Eqs. 20 and 21) respectively, this would result in a balance of the anodic current and the cathodic current flowing across the TPB,

$$i_{CO} = \int j_{CO} dA = A \cdot j_{CO} \tag{20}$$

$$i_{O_2} = \int j_{O_2} dA = A \cdot j_{O_2} \tag{21}$$

where A is the area of the TPB. From another point of view this means, the mixed potential is formed, when the anodic current (i_{CO}) produced by the EOC is equal to the cathodic current (i_{O_2}) produced by the ORR, and accordingly the net current ($i_{net} = i_{CO} + i_{O_2} = 0$) across the TPB is zero.

According to the model introduced above it can be concluded that, the mixed potential formation is enhanced (the φ_m more negatively shifted: $\varphi_m^1 \rightarrow \varphi_m^2 \rightarrow \varphi_m^3 \rightarrow \varphi_m^4$) by enhancing the EOC and/or depressing the ORR, and reduced by depressing the EOC and/or enhancing the ORR, respectively (Fig. 4). In addition, it has to be noted that, part of CO would be consumed before reaching the TPB in a non-electrochemical way via the CGR, which may reduce the local concentration of CO at the TPB. This will decrease the rate of the EOC, and accordingly depress the mixed-potential formation in an indirect way.

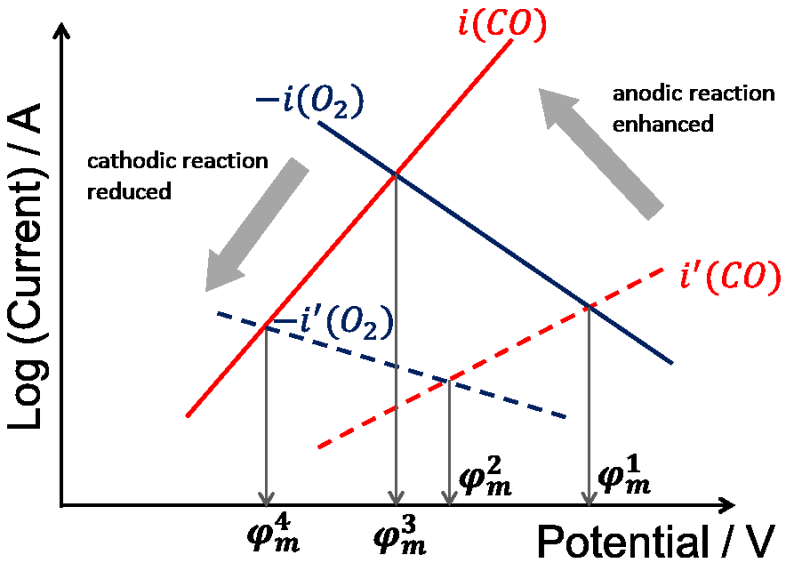

Fig. 4: *Schematic representation of the mixed potential formation in four kinds of situations according to the differences in the kinetics of the electron transfer reactions, taking the assumption of Butler-Volmer rate-determining kinetics as an example*

So far, the mixed potential generating mechanism (Fig. 2, Eqs. 11&19), and correspondingly the role of different involved electrode processes on the mixed potential formation (Fig. 4) have been discussed in detail. However, these discussions are based on the assumption of a constant temperature, i.e. the sensor is isothermally operated.

On the other hand, it's pretty obvious that the electrode processes contributing to the mixed potential formation, like gas adsorption/desorption, surface/pores diffusion, gas phase reaction within the electrode layer (reaction (3)) and the electrochemical reactions at the TPB (reactions (5) & (6), Eqs. (7) & (8)), are strongly influenced by the temperature, even though the corresponding temperature dependencies are not clear up to now. In spite of that, it can be still inferred according to [22] that, these processes for different gas species probably show distinct dependencies on the temperature, since an individual kind of gas species would be involved in these processes at variation of the

temperature in a specific manner [104]. Generally those chemical and electrochemical processes can be described by Arrhenius-like equations based on the assumption of activated processes with different activation energies.

In particular when the temperature is continuously varied, for example the sensor is thermo-cyclically operated (Sec. 3.3), these potential forming processes may probably show different temperature behaviors which depend on the kind of gas species involved, and interact with each other in a complex way. As a consequence, temperature dependent profiles of mixed potential formation under thermo-cyclic condition are expected to show gas component specific characteristics. This aspect is discussed in detail in Sec. 4.5.

3. EXPERIMENTS

3.1 Sensor element

The sensor element studied in this work is commercially available (CarboSen, Lamtec Mess- und Regeltechnik für Feuerungen GmbH&Co, Walldorf, Germany). As schematically shown in Fig. 5, a CarboSen sensor element is comprised of two identical layered Au,Pt-YSZ electrodes (3.3mm x 1.5mm) on top of a porous YSZ layer (4mm x 3.5mm) and a buried Pt reference electrode (Pt-RE). The Pt-RE is located between an alumina substrate (17mm x 3.5mm) and the YSZ-layer. A thick-film Pt resistive heater is positioned on the reverse side of the substrate to heat up the sensor element to operating temperature up to approx. 850 °C.

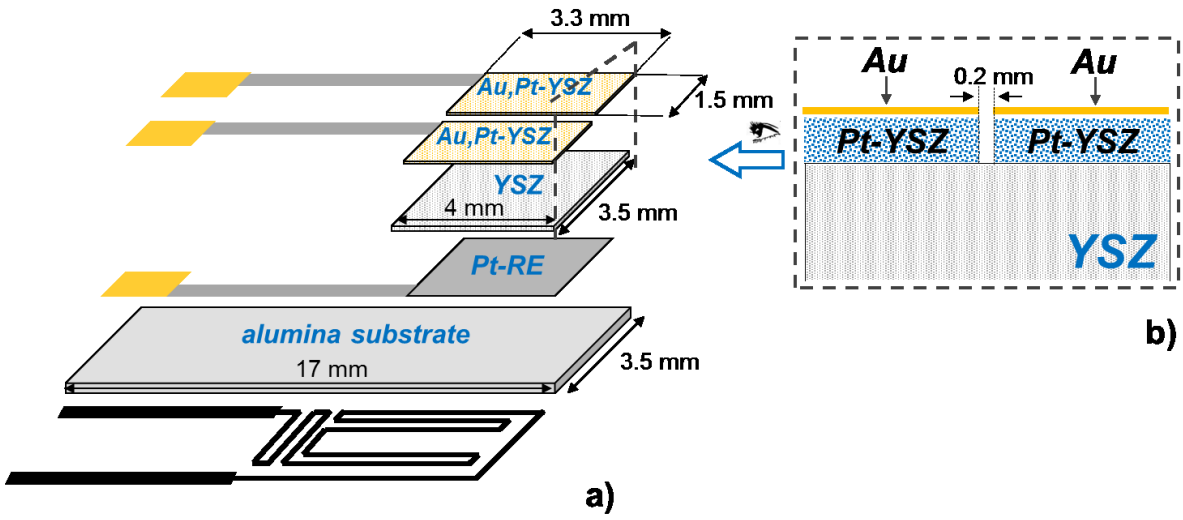

Fig. 5: *Schematic drawing of a CarboSen sensor element in exploded view (a) and the structure of the layered Au,Pt-YSZ electrode in cross-sectional view (b)*

According to the technical information offered by Lamtec Mess- und Regeltechnik für Feuerungen GmbH&Co, the YSZ layer was fabricated by screen printing. On its top the layered Au,Pt-YSZ electrodes (APE) were prepared layer by layer (Fig. 6) in two steps: the thick-film Pt-YSZ parts (90 mass% Pt and 10 mass% YSZ) were first screen printed and sintered, and afterwards the thin gold films were deposited by PVD-technique and again sintered. The distance between these two electrodes is approx. 0.2mm (Fig. 5b).

Sensor elements with two different thicknesses of the Au layer are available, and according to different sintering processes of the as-prepared APEs the sensors are classified into type I, type II and type III (TABLE 1). The amount of gold deposited at the type II- and the type III-APE is the same, which is about the double of that at type I-APE (Völkel and Hammer 2015, personal communication). However, the exact thicknesses of Au layer on these types of APEs are not available from the manufacturer.

Table 1: *Preparation parameters of the thin-film Au layer for diffferent types of CarboSen sensor elements*

	amount of Au deposition [arbitrary unit]	sintering temperature [°C]	sintering time [min]
type I	1	850	10
type II	2	850	10
type III	2	1050	240

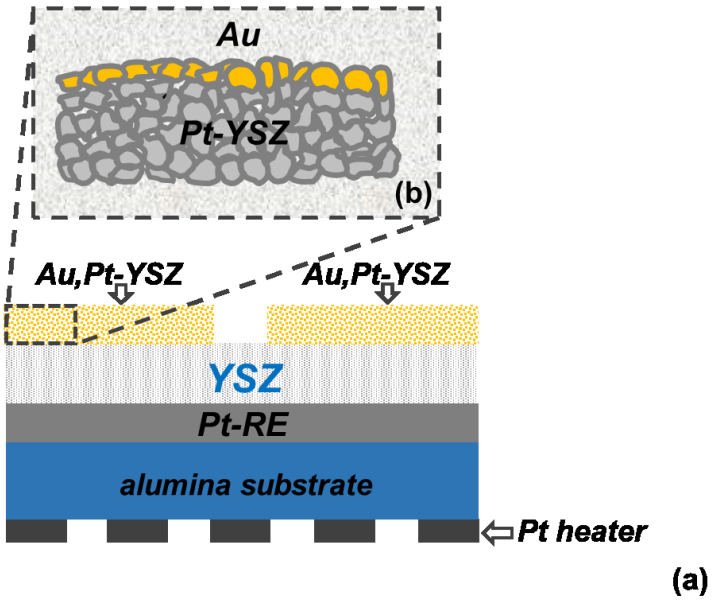

Fig. 6: *Schematic drawing of the layer structure of (a) the CarboSen sensor element and (b) the as-prepared Au,Pt-YSZ mixed potential sensing electrode before sintering in cross-section view*

3.2 Electrode material characterization

An ESEM type XL 30 FEG, Philips Inc. equipped with an EDX system [Inst. for Functional Interfaces, Karlsruhe Institute of Technology (KIT)] was used to study the surface morphological structures of the different types of APEs listed in Table 1.

In addition, for further studies of the crystal structure of the APEs, and the Au distribution from the top surface into the bulk of the electrodes, two layered Au,Pt-YSZ model samples were self-prepared and sintered on an alumina substrate in analogy to the type II- and the type III-APE of the commercial sensors, respectively. A commercial Pt paste (ESL 5570, ElectroScience, U.S.A) containing 92 mass% Pt and 8 mass% YSZ, which is similar to that used for the CarboSen sensor (Sec. 3.1), was taken to fabricate the Pt-YSZ part of the model sample by micro-dispensing and afterwards was fired at 1200 °C for 90 min. After deposition of the thin-film Au layer by sputtering technique (sputtering power: 100W, time: 12s), the model samples were fired separately at 850 °C for 10 min and 1050 °C for 240 min, which are in equivalence with the APE sintering procedure of the commercial sensors.

However, the thickness of the thin film Au layers on the model samples was estimated to be approx. 25 nm before sintering, which is probably not the same as the corresponding Au-layer thickness of the commercial APEs. The model samples were made in a larger size (7mm x 7mm) due to the technical requirements of the analytical instruments. In a later step the depth profile of the metal components was estimated by Glow Discharge Optical Emission Spectroscopy (GD-OES) using a GD Profiler 2^{TM} (HORIBA, Kyoto, Japan) in collaboration with HORIBA Trading Co., Ltd. Shanghai China, and the XRD study was carried out with a MiniFlex X-ray diffractometer (Rigaku Inc., Tokyo, Japan).

3.3 Steady state and dynamic electrochemical measurements

For experimental investigations of the electrochemical characteristics of the sensors under various gas conditions, an automated test system (Fig. 7) was employed, which enables not only the adjustment of gas compositions at a constant flow rate (200 ml/min) but also the sample and record of sensor signals. This automated sensor test system is a standard test setup used at the Institute of Sensor and Information Systems (Karlsruhe University of Applied Sciences), which consists of a gas mixing setup, a sensor test cell and a data acquisition and control unit as schematically shown in Fig. 7a.

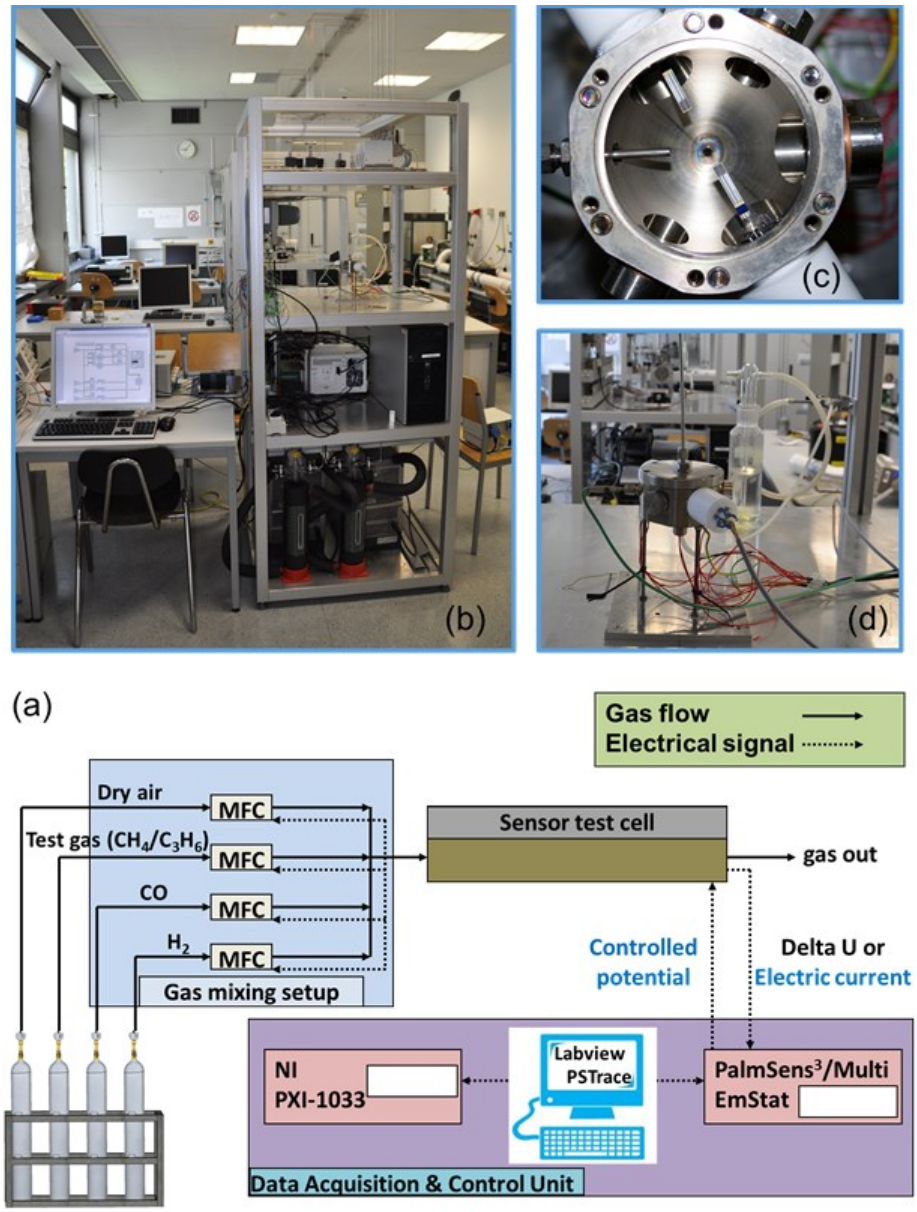

Fig. 7: *Schematic drawing of the automated sensor test system (a) and photographs giving an overview of this system (b), and the sensor test cell openned (c) and arranged in the measurement setup (d).*

The gas compositions were adjusted to predetermined values by mixing gas flows of parent gases (5000 ppm H_2, CO or C_3H_6 in synthetic air) with dry synthetic air and N_2. The flow rates of the gas flows were controlled by mass flow controllers via a Labview program (Fig. 7a). Under well-defined

gas atmospheres, the steady state (OCP) and the dynamic (CV and EIS) electrochemical measurements were carried out using an electrochemical working station (PalmSens3/MultiEmStat, PalmSens, The Netherlands), while the corresponding electrochemical data were sampled via the operating softwares (PSTrace/MultiTrace, PalmSens, The Netherlands).

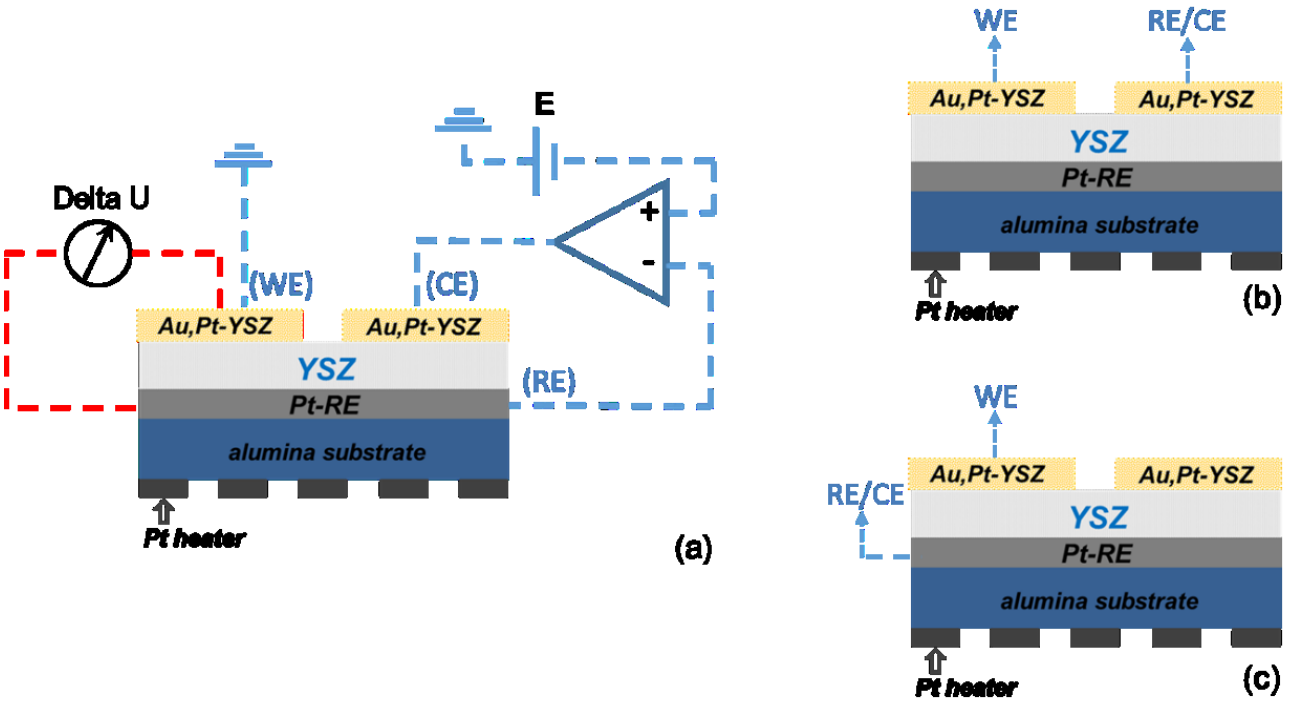

Fig. 8: *The electrical wiring arrangements for (a) OCP measurements (on the left red dashed line), CV measurements (on the right blue dashed lines), (b) EIS measurements and (c)sensor regeneration*

Sensing behaviors (OCP response) of the sensors were studied by measuring the potential difference (ΔU) between the APE and the Pt-RE (red dashed line in Fig. 8a) at isothermal and thermo-cyclic operation, separately. Working temperatures of the sensors were characterized using an infrared camera (PYROVIEW 320L, DIAS Infrared GmbH, Dresden, Germany).

In isothermal experiments, the OCP responses were measured for all the three types of sensors under exposure to various concentrations of target gases (H_2, CO, CH_4 and C_3H_6) balanced with different O_2/N_2 admixtures, while the sensors were operated isothermally at a certain temperature in the range between 500 °C and 700 °C. The detailed experimental conditions for different types of sensors are listed in TABLE 2.

Thermo-cyclic experiments were carried out on a type II-sensor under exposure to H_2, CO, and C_3H_6 containing gases, separately. The corresponding OCP data were sampled at simultaneous sensor operation with a triangular scanning heating voltage with a period of 300 sec, which resulted in a linear variation of the sensor operating temperature ranging between 410°C and 670°C as checked by IR-camera.

Table 2: *Detailed experimental conditions (gas compositions and temperatures) for the type I, II and III sensors (Gas flow at all experimental settings was 200 ml/min)*

	CO			H_2 / C_3H_6			CH_4		
	conc. range/step variation [ppm]	O_2 Vol.%	T [°C]	conc. range/step variation [ppm]	O_2 Vol.%	T [°C]	conc. range/step variation [ppm]	O_2 Vol.%	T [°C]
type I	0 – 1000 / 250	5 — 20	600	—	—	—	—	—	—
type II	0 – 1000 / 250 or 0 — 2000/500	5 — 20	500 — 700	0 — 2000/500	7 — 20	650	0 — 1000/250	20	650
type III	0 — 1000 / 250 or 0 — 2000/500	5 — 20	500 — 700	0 — 2000/500	7 — 20	650	0 — 1000/250	20	650

Complementarily, the dynamic electrochemical behaviors of the electrodes were firstly investigated by CV and EIS measurements at 600 °C in various gas atmospheres at different CO (0 – 1000ppm) and O_2 concentrations (5 – 20 vol.%). In a later step, the CV and the EIS characterizations of the electrodes were extended in a broader temperature range (500 – 700 °C), which are the same as adopted in the OCP measurements, but only under exposure to synthetic air.

A three-electrode configuration was used in the CV measurements, as shown in Fig. 8a (blue dashed line). Every CV measurement was done with five scans at a potential scan rate of 50 mV/s. In Chap. 4, all the CV results are discussed using the last scan, when the cyclic voltammogram had approached to steady state. Each potential scan started from the equilibrium potential φ_e and was followed by a negative sweep to $U_{vertex1}$. Afterwards, the scan direction was reversed and then swept positively to $U_{vertex2}$, and in the end went back to φ_e again, as depicted in Fig. 9. Different sets of negative and positive and negative U_{vertex} were applied to characterize different types of sensors, which are described in TABLE 3.

The EIS measurements were conducted on the sensors using a two-electrode configuration (Fig. 8b). A sinusoidal voltage with a frequency sweep from 10 kHz down to 10 or 2 mHz and a perturbation of 10 mV was applied on the electrochemical cell Au,Pt-YSZ/YSZ/ Au,Pt-YSZ to study its EIS characteristic, which is a combination of an interfacial part (electrode/electrolyte) and a bulk part (electrolyte). Electrical equivalent circuit parameters describing the interfacial processes were extracted from the EIS data, and plotted over the O_2 concentration or the operating temperature (Arrhenius plot) to get an insight on the processes involved in the electrochemical cell and especially the electrochemical reactions proceeding at the electrode/electrolyte interface (Sec. 4.2 & 4.4).

Table 3: *Vaired parameter sets used in the CV measurements for different types of sensors*

	Parameter set 1			Parameter set 2		
	$U_{vertex1}$ [V]	$U_{vertex2}$ [V]	T [°C]	$U_{vertex1}$ [V]	$U_{vertex2}$ [V]	T [°C]
type I	--0.8	0.5	500 – 600	—	—	—
type II	--0.8	0.5	500 – 600	--0.4	0.3	600
type III	-0.5	0.5	600	--0.4	0.3	600

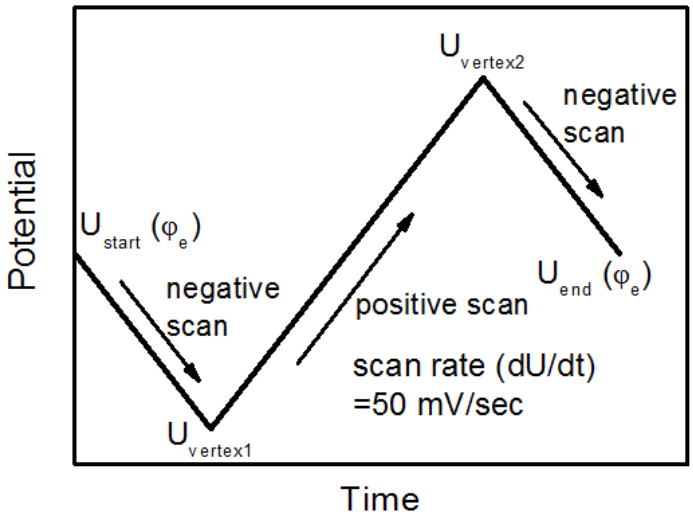

Fig. 9: *Illustration of a potential scan used in the CV experiments*

3.4 Stability tests and regeneration of sensors

Long term stability of the sensors was studied by OCP and EIS measurements (Sec. 3.3), while they were operated i) under gas exposure or ii) in ambient air. In the stability tests under gas exposure, a type II and a type III sensor were operated at 650 °C and exposed to H_2, CO, and C_3H_6 balanced with O_2/N_2 mixtures, separately. Concentrations of these gases were changed from 0 ppm to 2000 ppm at varied O_2 concentrations ranging from 7 – 20 vol.%. In order to evaluate the sensitivity variation under these gas exposures, the OCP responses at a concentration of 1000 ppm test gas balanced with synthetic air were sampled separately for each gas species in the beginning, at the intermediate time of the procedure and the end of the test, as depicted in Fig. 10. The duration of gas exposure is the same for all the three different kinds of gas species, which is approx. 12h. In addition, ex-situ observations on the optical changes of the electrode surfaces were carried out with a digital microscope ((VHX-500F, KEYENCE Corp, Japan) in the experimental procedure.

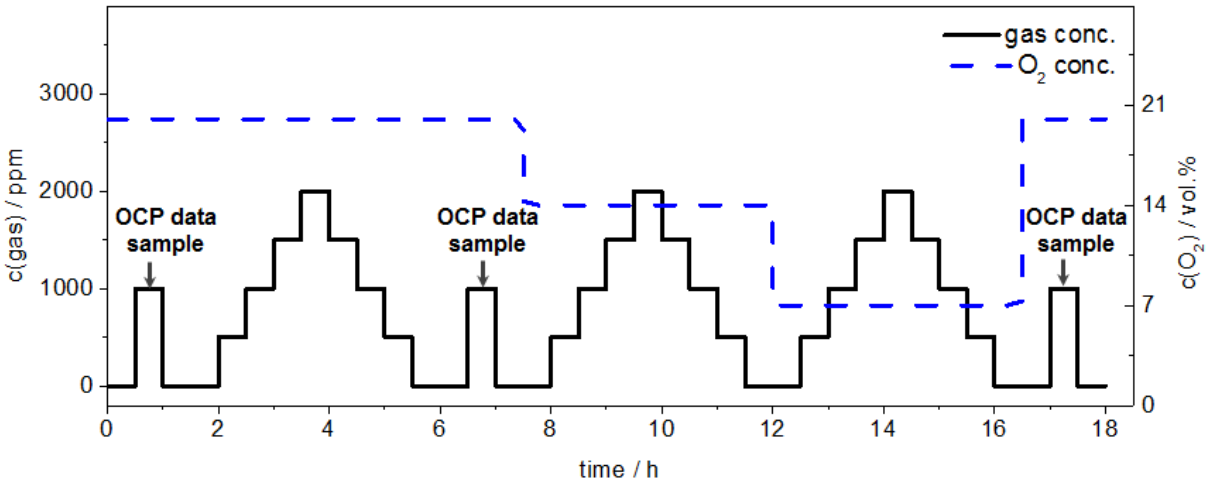

Fig. 10: *Gas (H_2, CO or C_3H_6) concentration profiles used in the stability tests under gas exposures*

With respect to the stability tests under ambient air condition, another fresh individual of type III sensor was operated at 600 °C for 100 days. The OCP responses of the sensor were characterized under exposure to CO balanced with synthetic air (c(CO)=1000 ppm) at 600 °C on the 1st, 47th and 100th day separately, while the corresponding EIS characteristics were studied at the same temperature but only in synthetic air. Except for the operation in these measurements, the sensor was kept in ambient air at 600 °C over this period of 100 days. After that, the sensor was tried to be regenerated by negative electrical polarization using a two-electrode configuration (Fig. 8c). Potential scans between the equilibrium potential φ_e and -0.6 V with a scan-rate of 50 mV/s were applied to the Au,Pt-YSZ/YSZ/Pt cell at elevated temperatures (600 °C – 700 °C) at 5 vol.% O_2 or in synthetic air. These scans were repeated, and afterwards the OCP and EIS measurements were carried out under the same conditions as stated above.

4. RESULTS AND DISCUSSION

4.1 Correlation of structural properties of layered Au,Pt-YSZ electrode with its electrochemical characteristics

4.1.1 Structural properties of the layered Au,Pt-YSZ electrode

Structural properties of three types of APE (Sec. 3.1) were studied with respect to the morphological and the crystal structure of the electrode, and the distribution of elemental composition within the electrode layer separately. Fig. 11a shows that the sensor element comprises a porous APE electrode layer (thickness: approx. 15 µm) on top of a less porous YSZ-layer (thickness: approx. 45µm) and a thin Pt-RE layer which is located between a compact alumina substrate and the YSZ-layer.

The Au on the YSZ layer between the electrodes does not hold the shape of a continuous layer but is crystallized after sintering process. As shown in Fig. 11e, almost all the Au was crystallized on the YSZ layer at the type I-sensor with thinner Au deposition, while only part of the Au got crystallized at the type II-sensor with thick Au deposition (Fig. 11f). In addition it is found from Fig. 11g that, the size of Au crystals on the YSZ layer is larger at the type III-sensor sintered at 1050 °C compared to those at the type I- (Fig. 11e) and the type II-sensor (Fig. 11f) sintered at 850 °C.

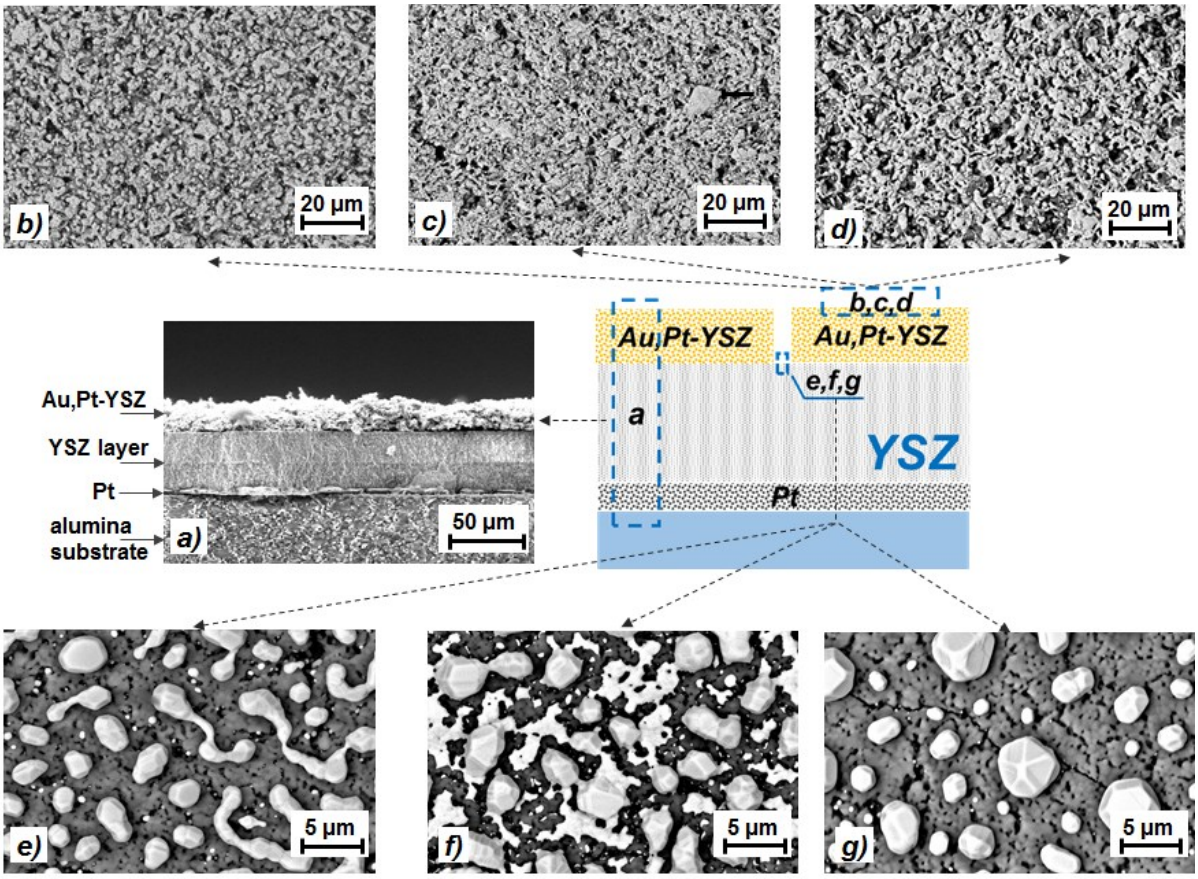

Fig. 11: *ESEM images of the layer structure of the sensor element (cross section) (a), the Au,Pt-YSZ electrodes (top view) of type I (b), type II (c) & type III (d), and the corresponding YSZ layers (top view) between the electrodes (e-g)*

The porous electrode structure is found for all the three types of sensors. No clear difference can be seen in the electrode morphology in terms of porosity and grain size at 1000x magnification (Fig. 11b-d). But, at 5000x magnification it is shown that, the electrode surface of the type II-APE is found to be covered by an inhomogeneous bright layer (Fig. 12 b, e.g. the red dashed rims) which was confirmed to be Au by EDX analysis. But, such a well-connected Au layer cannot be observed on the electrode surfaces of the type I- and type III-APE, as depicted in Fig. 12 a and c respectively.

On the other hand, the surface morphology of the type III-APE is seen to be also different from that of the type I-APE. Some parts on the surface of the type III-APE (e.g. Fig. 12 c, the red dashed rim) seem to be covered by a relatively more homogeneous layer compared to that on the type II-APE. However, this homogeneous layer could not be identified as Au by EDX analysis. This is probably due to the higher sintering temperature (1050 °C vs. 850 °C) and the longer annealing time (4h vs. 10min) for this type of APE (Sec. 3.1). That is to say, the sintering process of the type III-APE after the step of thin Au film deposition is assumed to bring about a stronger diffusion (into the inner regions of the electrode) and perhaps a more intensive alloying of Au with Pt at the higher sintering temperature (1050 °C) for a longer sintering time (240 min) compared to the other two APEs.

These observations of different electrode surface morphologies due to different sintering conditions (Sec. 3.1) and the corresponding interpretations, are also well correlated with the XRD and the GD-OES analysis of the model samples prepared in analogy to the corresponding commercial APEs (Fig. 13), which are discussed in detail in the following paragraph.

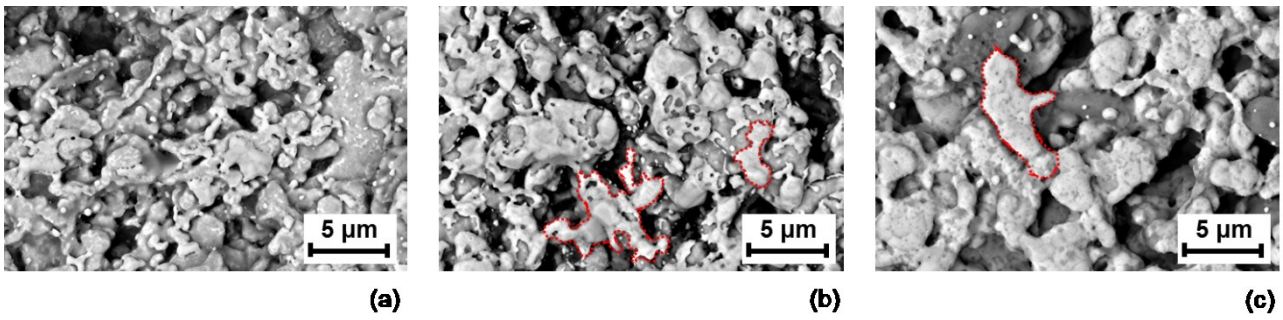

Fig. 12: *ESEM images of all the three types of APE at 5000x magnification (a: type I, thinner Au deposition, sintered@850°C; b: type II, thicker Au deposition, sintered@850°C; c: type III, thicker Au deposition, sintered@1050°C)*

The crystal structure of the APEs, and correspondingly the elemental distribution within the electrode layer were investigated by XRD and GD-OES analysis of two self-made model samples, which were prepared in the very similar procedure to the type II- and the type III-APE of the commercial sensor, respectively (Sec. 3.2). However it has to be noted that, there are still some discrepancies in the preparation of the commercial APEs and the model samples, like the difference in the Pt pastes used for the fabrication of the thick film Pt-YSZ body and the thickness of the thin film Au layer deposited by PVD technique (Sec. 3.2). Despite of those discrepancies, both the commercial APEs and the model

samples possess a similar layered structure with a porous thick film Pt-YSZ body covered by a thin film Au layer.

Accordingly, it is assumed that the XRD and the GD-OES analytical results of the model samples also hold for the commercial APEs. Fig. 13 shows the XRD patterns of the model samples with the same amount of Au deposition but sintered at the two different temperatures. Both types of model samples, no matter if sintered at the lower or the higher temperature, show mainly the characteristic peaks of polycrystalline Pt and ZrO_2 (Fig. 13 a&d). However by carefully checking the zoomed views of the XRD patterns in the range where the Au peaks are expected, several small characteristic peaks of Au (at $2\theta = 38.94°$, 45.24° and 65.62°) were observed for the model sample sintered at 850 °C (Fig. 13 b&c), while these Au peaks were not found for the model sample sintered at 1050 °C (Fig. 13 d-f). This is a clear indication that part of the Au forms a separate crystalline phase when sintered at the lower temperature (850 °C). But this was not observed when the sample was sintered at 1050 °C.

From the ESEM and the XRD analytical results, it could be tentatively concluded that by sintering at the higher temperature the Au reaches deeper regions of the electrode layer by diffusion and tends to alloy more intensively with Pt rather than to form a separate crystalline phase on the electrode surface. This interpretation is in good consistence with the binary alloy phase diagram of Pt-Au system as shown in the appendix [105], and is supported by the results of the GD-OES analytical experiments shown below (Fig. 14).

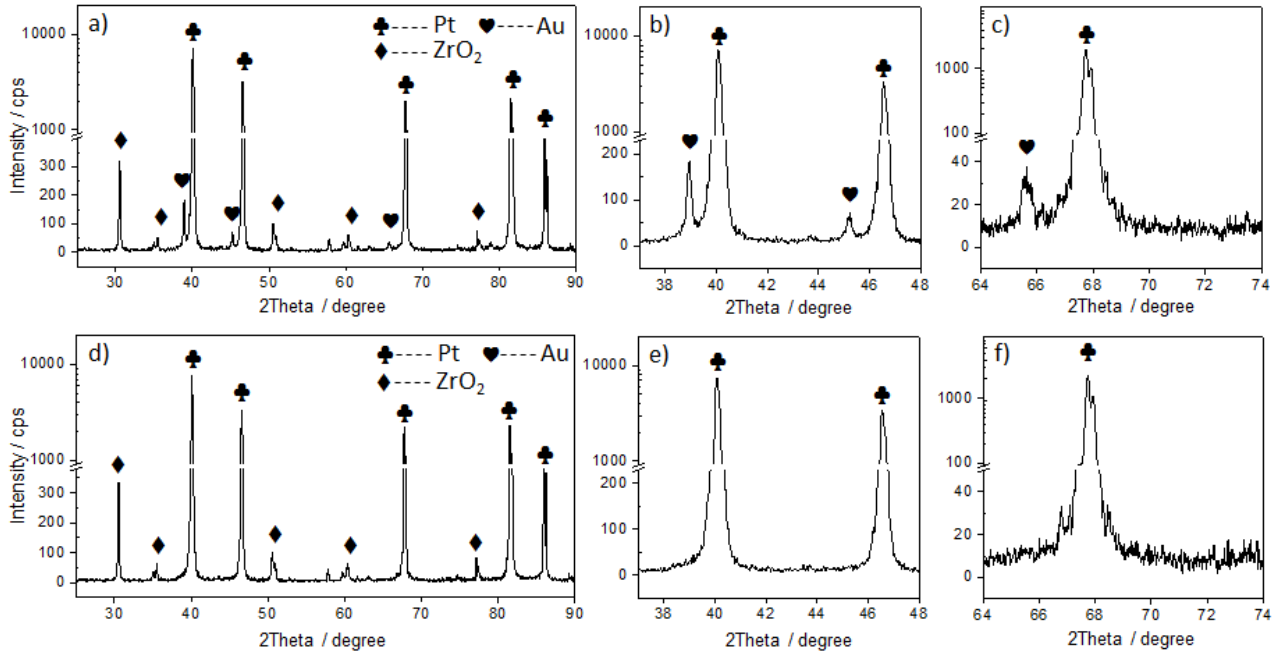

Fig. 13: *Overview of the X-ray diffraction patterns of the self-prepared model samples sintered at 850 °C (a) and 1050 °C (d), and the corresponding zoomed views in the Au peak range for the low temperature (b,c) and the high temperature (e,f) sintered samples, respectively*

GD-OES analytical experiments reveal that the Au distribution from the top surface into the bulk of the Au,Pt-YSZ electrodes is strongly influenced by the sintering conditions as depicted by the depth

profiles of metal components (Pt, Zr, Al and Au) of the self-prepared Au,Pt-YSZ samples sintered at 850 °C and 1050 °C in Fig. 14a and Fig. 14b, respectively. Except the Au-depth profile, the distributions of the other metal components (Pt, Zr and Al) within the sample layers are very similar for both types of the model samples. After a small peak observed at about 15 s, the Pt content is almost kept constant till approx. 210 sec, and after that reduces dramatically. The Zr-content rises rapidly in the very beginning, and afterwards only increases with a very slow rate. Similar to the Pt-content, there is a clear reduction of the Zr-content after 220 s. At the same time of analysis the Al-content rises and grows significantly. This is an indication of the transition from the Au,Pt-YSZ sample to the alumina substrate.

On the other hand, a significantly distinctive Au distribution within the sample layer is observed for both types of model samples. The Au content in the sample sintered at 850 °C is sharply decreased from the very beginning, and approaches to zero after about 100 s (Fig. 14a). However, a much more moderate Au gradient decrease with a clearly smaller surface concentration was found for the sample sintered at 1050 °C, and even after 200s a very slight analytical response of the Au content was detected (Fig. 14b).

The total thicknesses of both samples were measured to be approximately 15 μm. Correspondingly, if assuming a constant rate of erosion, the thickness of the layer where the Au-content declines from the surface concentration to about zero is estimated to be about 3-5 μm for the sample sintered at 850 °C, while the Au content is detectable almost over the whole thickness of the sample layer sintered at 1050 °C. This means, that the Au partly diffuses from the top surface into the Pt-YSZ thick-film layer during the firing process after the step of thin Au film deposition at 850 °C (10 min) and 1050 °C (240min), respectively (Sec. 3.1 & 3.2). The corresponding Au distribution gradients over the thickness of the samples are highly dependent on the sintering temperature and time.

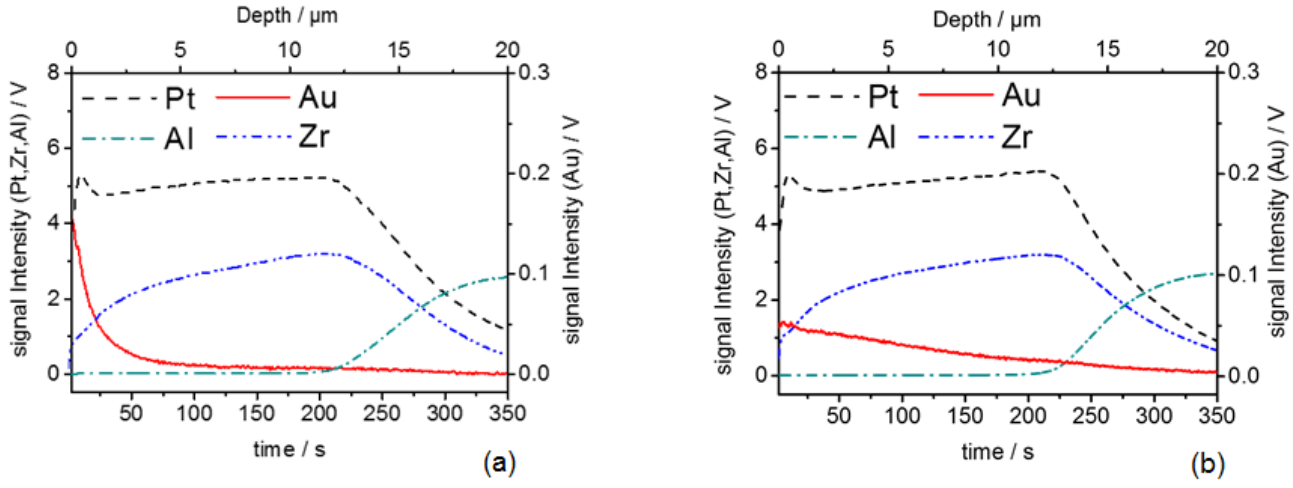

Fig. 14: *GD-OES analysis of elemental depth profile of the self-prepared model sample sintered at (a) 850 °C and (b) 1050 °C*

From these material analysis results stated above, it can be concluded that the higher sintering temperature (1050 °C) of the APE/the model sample results in not only a more uniform morphology of the electrode surface without a separate crystalline phase of gold (ESEM & XRD), but also in a better alloying of Au and Pt [105] in the inner parts of the electrode by diffusion of Au during the sintering process (GD-OES). These clear differences, in the morphological, crystal and structural properties of the APEs due to the different amount of Au deposition and sintering conditions (Sec. 3.1 & 3.2), are assumed to be the reasons for different catalytic activities over the electrode layer, and probably for their different electrochemical behaviors as well.

4.1.2 Mixed-potential formation at the layered Au,Pt-YSZ electrode - a qualitative model

Due to the special structural properties of the APEs (Sec. 4.1.1), it seems to be not sufficient to interpret the potential formation processes at such kind of electrodes by applying the well-accepted model of the mixed-potential forming mechanism proposed by Miura et al [20, 51], as introduced in Chap. 2. This model is frequently cited in the discussions of mixed potential gas sensing behaviors [20-22, 38, 51, 106]. It deals with the potential forming mechanism of the kind of mixed potential electrode (Fig. 15a), at which the potential is formed uniformly and only at the interface between the MPE and the solid electrolyte, due to the assumption that the material compositions are evenly distributed in the electrode, and don't contain ZrO_2 as an additive.

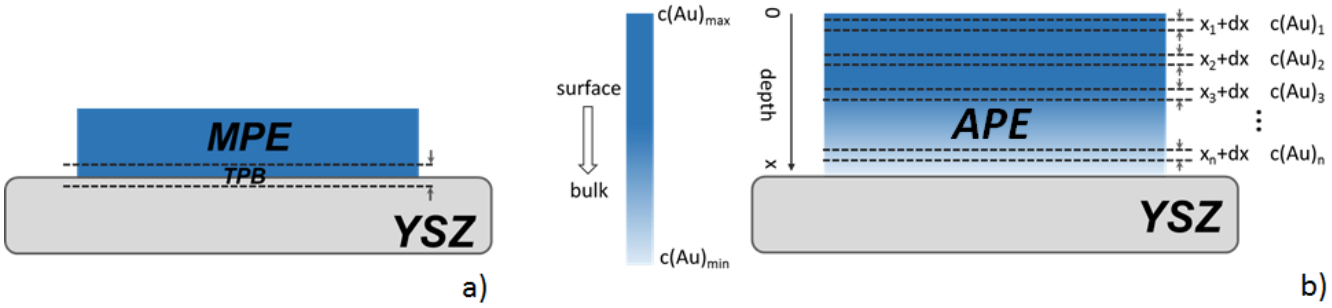

Fig. 15: *lillustrations of the mixed-potential electrode/YSZ half-cell with a uniform electrode material distribution (a), and the layered Au,Pt-YSZ electrode/YSZ half-cell (b)*

However with respect to the potential formation at the APEs, the situation is clearly different. From Fig. 14, it has to be concluded, that the mixed potential formation of the APE can proceed over the whole electrode layer due to the addition of ZrO_2 (extension of the TPB), but the formation of the mixed potential is not uniform, as in the Au,Pt-YSZ-composite the Au concentration shows a gradient from top to the inner parts of the electrode dependent on the sintering condition. This indicates, the EOC (reaction (5), Chap. 2) might probably proceed at non-uniform rates at different deepness of the porous electrode layer depending on the Au concentration, and the same should also hold for the ORR (reaction (6), Chap. 2).

Consequently, we have to infer that over the thickness of the APE, the current densities show an uneven distribution in correlation with the Au concentration gradient from the surface to the bulk of the electrode (Fig. 14). But, if we only consider the case of a certain layer of the APE at the depth x with an infinitesimal thickness dx (Fig. 15b), a uniform electrode material distribution with a constant Au concentration can be assumed within this infinitesimal thickness dx. As a consequence, it is postulated that at this layer at the depth x the anodic and the cathodic current densities are evenly distributed, but mostly they are not balanced to zero.

At the depth x_1 close to the electrode surface where the Au concentration is higher compared to that in the inner part of the electrode (Fig. 15b), the anodic current density is deemed to be higher than the cathodic one, since the EOC (reaction (5), Chap. 2) is more favored at the reaction sites with higher Au concentration compared to the ORR (reaction (6), Chap. 2) [52]. As a result, by integrating

these two current densities in the layer at the depth x_1 (Eqs. (22) and (23)), a positive net current (Eq. (24)) is expected. The situation of the potential formation is different at the deeper parts of the APE, due to the decrease of Au concentration with depth from the top to the deeper regions of the electrode. The net current (Eq. (25)) at a deeper depth (e.g. x_2) compared to x_1 would become less positive than $i_{net}^{x_1}$, as the EOC (reaction (5), Chap. 2) gets less favored at the reaction sites with reduced Au concentration. At a certain depth x_3 ($>x_2$), the EOC (reaction (5), Chap. 2) may even proceed at a same rate as that of the ORR (reaction (6), Chap. 2), which would consequently result in a zero net current at this layer (Eq. (26)). However, when reaching an even deeper part of the APE (e.g. at depth x_n), the net current ($i_{net}^{x_n}$) is presumed to become negative (Eq. 27), due to the reason that the Au concentration at this depth is so low that the ORR (reaction (6), Chap. 2) is now dominating in relation to the EOC (reaction (5), Chap. 2).

$$i_{CO}^{x_1} = \int j_{CO}^{x_1} dA = A \cdot j_{CO}^{x_1} \tag{22}$$

$$i_{O_2}^{x_1} = \int j_{O_2}^{x_1} dA = A \cdot j_{O_2}^{x_1} \tag{23}$$

$$i_{net}^{x_1} = i_{CO}^{x_1} + i_{O_2}^{x_1} > 0 \tag{24}$$

Even though the net currents at different depth of the APE are dependent on the individual local Au/Pt-ratio and in most cases are not balanced to zero, the corresponding integral of them over the whole electrode layer, which represents the overall net current flowing through the APE (i'_{net}), must be a null (Eq. (28)), since the electrode is operated under the zero current condition.

$$i_{net}^{x_2} = i_{CO}^{x_2} + i_{O_2}^{x_2} > 0 \tag{25}$$

$$i_{net}^{x_3} = i_{CO}^{x_3} + i_{O_2}^{x_3} = 0 \tag{26}$$

$$i_{net}^{x_n} = i_{CO}^{x_n} + i_{O_2}^{x_n} < 0 \tag{27}$$

$$i'_{net} = \int i_{net}^{x} dx = \int i_{CO}^{x} dx + \int i_{O_2}^{x} dx = 0 \tag{28}$$

Following the discussion above, the mixed potential at the APE is proposed to be established under the condition, when the sum of the anodic and the cathodic currents, both non-uniformly distributed over the APE at different depths, are balanced over the whole electrode. In spite of this structural difference of the APE compared to the electrodes with uniform material distribution, it can be still assumed that the chemical oxidation of CO and the electrochemical reactions at the TPB are the two major factors determining the mixed potential formation, which is similar to the electrodes with uniform material distribution as reported in [28, 29, 31, 38, 51, 54, 92]. However, it has to be noted that the kinetics of the CO chemical oxidation (CGR) (reaction (3), Chap.2) depends on the Au distribution with deepness x as well, which is not taken into account in this model. This aspect even more complicates the understanding of the potential formation at the APE. As an essential fact it makes the electrochemical behavior of the APE dependent not only on the original thickness of the

Au-film deposited, but also on the Au concentration gradient over deepness x which is highly influenced by the sintering temperature and time (Sec. 4.1.1) after the step of thin Au film deposition.

4.1.3 Effect of Au thickness and sintering conditions on OCP and CV behaviors of layered Au,Pt-YSZ electrode

Gas response behaviors of type I-, type II- and type III-sensor under exposure to CO mixed with O_2/N_2 mixtures at 600 °C are shown in Fig. 16. Stable and reversible negative potential steps are found for all the three types of sensors in response to stepwise variation of CO concentration in the upward and downward change. By decreasing the O_2 concentration, all the type I – III-sensors show an enhanced sensing response at the same stepwise variation of the CO concentrations.

Since the YSZ layers of the sensors were found to be porous (Sec. 4.1.1, Fig. 11), it is presumed that the gas atmosphere in the vicinity of the buried reference half-cell (Pt/YSZ) is in thermo-dynamic equilibrium with the ambient atmosphere (Sec. 3.1, Fig. 5). In the experiment, the oxygen concentration ranged from 5 to 20 vol.%, while the highest concentration of CO was not higher than 1000 ppm. This means, the Nernst potential generated at the Pt-reference half-cell can be assumed to be almost constant at various CO concentrations under the condition of a certain fixed O_2 concentration. That is to say, the delta U is mainly varied with the potential formed at the APE/YSZ half-cell [27, 52].

In spite of these similarities of the sensing behaviors, the type II-APE with thicker Au deposition sintered at 850 °C exhibits a clearly higher response to CO compared to the type I-APE with thinner Au deposition sintered at the same temperature (Fig. 16). An even higher response is observed at the type III-APE, which has the same thickness of Au deposition as the type II-APE but was sintered at a higher temperature (1050 °C). The difference in the response intensity of these types of sensors (Fig. 16) can be well correlated with their structural properties depending on the thickness of Au deposition and the sintering conditions (Sec. 4.1.1), and qualitatively interpreted by the model of potential formation proposed in Sec.4.1.2.

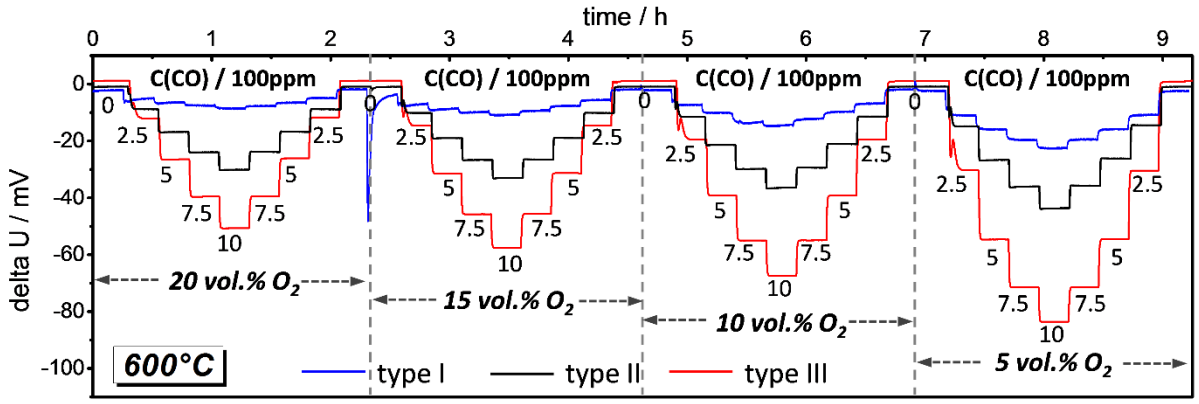

Fig. 16: *Response behaviors of the type I-(thinner Au deposition layer, sintered at 850 °C, blue curve), the type II-(thicker Au deposition layer, sintered at 850 °C, black curve) and the type III-sensor (thicker Au deposition layer, sintered at 1050 °C, red curve) under exposure to CO at different concentrations balanced with O_2/N_2 mixtures of varied O_2 concentrations at 600 °C. All numbers on the curves indicate the CO concentration in 100 ppm.*

With respect to the effect of Au layer thickness on the APEs, the better sensing response of the type II-APE with the thicker Au deposition compared to the type I-APE is firstly attributed to the reduced catalytic activity of this electrode for the gas phase reaction of CO (reaction (3), Chap. 2) by mixing Pt with Au, as already proposed by Vogel et al. in [25]. Due to this fact, it is supposed that CO is less consumed in a non-electrochemical way at the type II-APE, which consequently increases the local concentration of CO at the TPB, resulting in an enhanced anodic reaction and accordingly an increased response to CO (Fig. 4, Chap. 2). In addition, the thicker Au layer at the type II-APE is assumed to suppress the catalytic activity for the oxygen reduction reaction (reaction (6), Chap. 2), which results in a reduced cathodic current density and accordingly induces a larger deviation of mixed-potential from the equilibrium potential with oxygen. This could be the second reason for the better sensitivity of the type II-APE in comparison with the type I-APE, as discussed in Chap. 2 (Fig. 4).

With respect to the influence of the sintering conditions, the higher sintering temperature (1050 °C) and longer sintering time (240min) of the type III-APE results in a more even electrode surface morphology (Fig. 12 & 13), a more homogeneous Au/Pt-ratio in the inner parts of the electrode (Fig. 14) and probably a better Au-Pt alloying [105] compared to those of the type II-APE. Due to the fact that Au is less catalytically active than Pt [107], it can be inferred that the catalytic activity of the type III-APE for the CGR (reaction (3), Chap. 2) and the ORR (reaction (6), Chap. 2) is even lower than that of the type II-APE. According to the discussion above, the type III-APE is expected to show a stronger response to CO than the type II-APE, which is in good agreement with the experimental observation in Fig. 16.

To prove the hypothesis that the catalytic activity of APE is suppressed by thicker Au deposition and/or higher sintering temperature, the change of the ORR depending on the layer thickness of Au and its distribution at the electrode was investigated by CV measurements on all the three types of sensors in synthetic air, as shown in Fig. 17. The cyclic voltammograms of the type I-, the type II- and the type III-APE show considerable differences. A more pronounced cathodic peak is measured for type I-APE than that measured for the type II-APE (Fig. 17a), while significantly higher currents both in the anodic and the cathodic range are observed for the type II-APE compared to the type III-APE (Fig. 17b).

The CV measurements on these types of sensors suggest that the oxygen reaction kinetics at the APE is reduced by increasing the layer thickness of Au deposition (cf. type I- & type II-APE), while it can be further and even much more decreased by sintering the APE at the higher temperature (cf. type II- vs. type III-APE). According to the model introduced in Chap. 2 and the discussion above, the highest response to CO is expected and indeed found at the type III-APE (Fig. 16) with the lowest activity for the ORR (reaction (6), Chap. 2) among these three types of sensors (Fig. 17). This

indicates a domination of the EOC (reaction (5), Chap. 2) in the potential formation in relation to the ORR (reaction (6), Chap. 2).

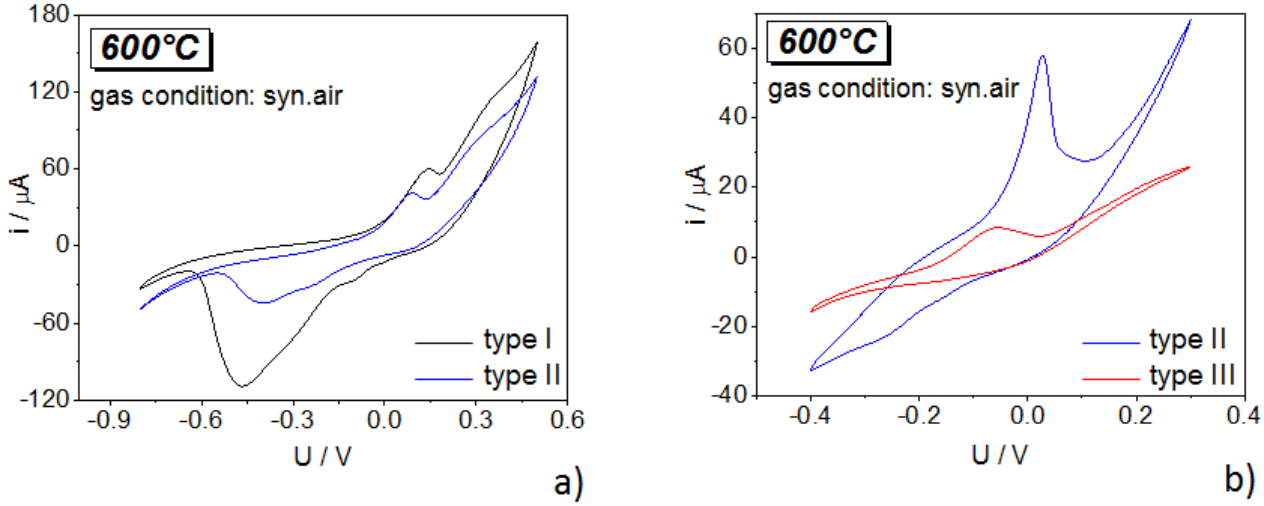

Fig. 17: *Comparisons of cyclic voltammograms for a) type I- & type II-APE and b) type II- and type III-APE in synthetic air at 600 °C. Curves in different colours represent different individuals of sensor elements*

Furthermore, by analyzing the potential steps of the type I–III-sensor elements in Fig. 16, it is found that for the type I- and type II-sensor sintered at 850 °C, the ΔU is linearly changed with the variation of CO concentration under fixed oxygen concentration ranging from 5 – 20 vol.% (Fig. 18 a-d). However, for the type III-sensor sintered at 1050 °C, the corresponding dependence of the delta U on CO concentration is only observed to be linear at 20 and 15 vol.% O_2 (Fig. 18 a&b), but starts to deviate from the linear dependence when reducing oxygen concentration to 10 vol.% O_2 (Fig. 18 c). This deviation gets even larger by further reducing the oxygen concentration to 5 vol.% (Fig. 18 d).

By replotting these data on a logarithmic concentration scale (Fig. 18 e-h) a clear transition from the linear to a logarithmic dependence of ΔU on CO concentration between 20 vol.% O_2 and 5 vol.% O_2 (Fig. 18 g) is disclosed. This change of the ΔU dependence on CO concentration is only observed at the type III-sensor but not at the type I- and type II-sensor, which indicates a transition from the transport controlled to the charge transfer reaction kinetics controlled mixed-potential formation at the APE sintered at 1050 °C between 20 and 5 vol.% O_2. That is to say, at the oxygen concentration higher than 10 vol.%, the rate-determining step in the potential formation at the type III-APE is the diffusion limitation of the CO transport to the TPB. But this starts to make a transition at 10 vol.% O_2, and then changes to the kinetic limitation of the electrochemical reactions occurring at the TPB when the oxygen concentration is further reduced to 5 vol.%.

However, this transition of the rate-determining process in potential formation is not found for the type I- and type II-APE sintered at 850 °C. This is possibly due to the higher catalytic activity of these two types of APE at which the CO is consumed at a higher rate via the gas phase reaction (reaction (3), Chap. 2) especially in the inner part of the porous electrode layer, i.e. the condition of diffusion limited transport of CO holds in the electrode potential formation at all the oxygen concentrations.

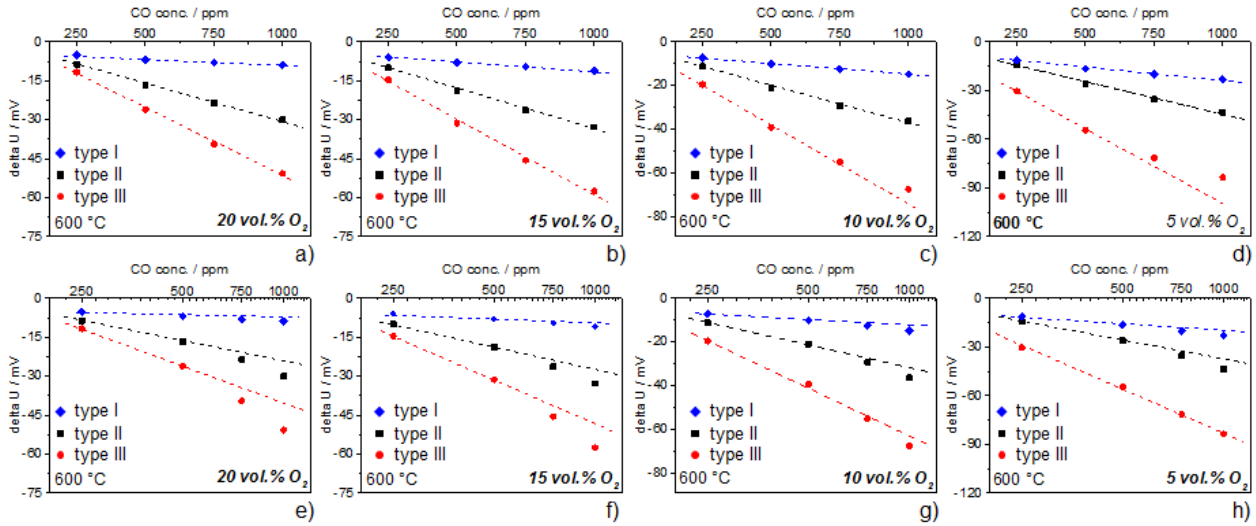

Fig. 18: *Dependence of ΔU at all the three types of sensors on different concentrations of CO under fixed oxygen concentrations on a linear scale (a-d) and a logarithmic scale (e-h)*

4.2 Study of electrode processes at layered Au,Pt-YSZ electrodes by CV and EIS measurement – two examples

As already stated in the introduction (Sec. 1.1), the investigations of mixed-potential type gas sensors in the past were mainly focused on the measurement of the potential difference (ΔU) between the mixed-potential electrode and the reference electrode by open circuit potentiometry [20-22, 26-32, 38, 51, 53, 54, 92, 108]. However, the ΔU value is only a general consequence of the underlying complicated mechanisms of potential formation at open circuit and under steady-state conditions (Fig. 2 & 3). The knowledge about these potential forming processes, e.g. the adsorption/desorption of gas molecules at the electrode surface/TPB, the mass transport processes (diffusion) within the electrode layer and the kinetics of the electron transfer processes at the TPB (Fig. 2), and their interactions cannot be attained by solely carrying out OCP measurements.

It was clearly shown in the previous section (Sec. 4.1) that, the higher CO sensing response of the APE (Fig. 16) was mainly related to the reduced electrode kinetics for the electron transfer reactions with oxygen species (Fig. 17), which is a consequence of the thicker Au layer deposition (Fig. 12) and/or the more uniform Au distribution at the electrode due to the higher sintering temperature and the longer sintering time. The kinetic information of the electron transfer reactions with oxygen species at the TPB was extracted by analyzing the CV characteristics of the sensors (Fig. 17).

But it has to be pointed out that besides the electrode kinetics, the CV study on the APE yields much richer knowledge about the electrode processes involved in the mixed potential formation, especially the dynamic information about those processes and their interactions at non-steady state conditions. That is to say how the electron transfer reactions at the TPB are influenced by the applied electrode potential, and in which way they are related with the mass transport processes occurring in the electrode layer at cyclic potential scans and different gas exposures. On the other hand, these electrode processes can be also studied by EIS measurements, which offer another possibility of the investigation at quasi steady state situations in a broad frequency range, because the polarization perturbation at the electrode used in the EIS measurements (10 mV) is much smaller than that used in the CV measurements (several hundred mV) (Sec. 3.3).

As good complements to the OCP data, the results of the CV and the EIS study help to depict a more comprehensive model of the electrode processes contributing to the mixed potential formation. In this context, two examples of a type III- and a type I-sensor with CV and EIS respectively, are presented and discussed in this section to show the possibility of achieving a better understanding of the electrode processes by dynamic electrochemical methods.

4.2.1 Case study I – CV investigation of a type III sensor

The CV characteristics of a type III sensor at 600 °C sampled with a scan rate of 50 mV/s under exposure to 21, 15, 10 and 5 vol.% O_2 are shown in Fig. 19. A pronounced and relatively narrow anodic peak was observed in the cyclic voltammogram at 21 vol.% O_2, while the peak in the cathodic region was found to be broader at the same O_2 concentration. By decreasing the O_2 concentration from 21 to 10 vol.%, the anodic peak became less and less distinct, and this feature got even vanished at 5 vol.% O_2. For the peaks in the cathodic region, they were kept to be noticeable at all the O_2 concentrations. When the O_2 concentration declined, the cathodic peak was first observed to get a little bit more pronounced from 21 to 15 vol.% O_2, and then, by stepwise further reducing the O_2 concentration to 5 vol.% O_2 the cathodic peak became monotonically smaller and smaller.

This non-monotonical change of current with O_2 concentration is also seen in the electric potential region beyond the anodic peaks at about 0.5 V (Fig. 19a dashed rim). The current in this region was first increased by decreasing the O_2 concentration from 21 to 15 vol.%, but passed a maximum and was reduced again when the O_2 concentration further declined. The currents measured in this region at 21 and 5 vol.% were found to be almost the same.

Moreover, the cyclic voltammograms at all the four O_2 concentrations depict clear current hysteresis (Fig. 19a), i.e. the current difference (Δi) at the same potential but in the positive and the negative potential sweep, respectively (Fig. 19b). This hysteresis reflects the charging and the discharging of the electrode/electrolyte interface, which is affected by the capacitive characteristic of the interface.

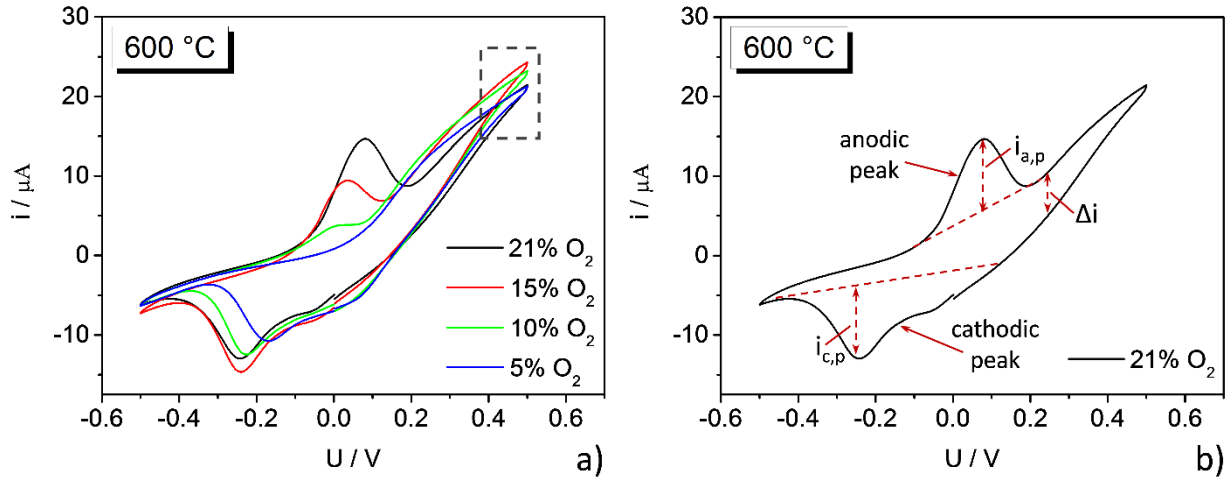

Fig. 19: *CV characteristics of a type III sensor at 600 °C under exposure to 21, 15, 10 and 5 vol.% O_2 (a), and schematic illustration of the baseline for the determination of the anodic & the cathodic peak and the current hysteresis, taking the CV profile at 21 vol.% O_2 as an example.*

A very crucial point for understanding the CV data is how to interpret the underlying mechanisms of anodic and cathodic peak formation. However, for YSZ based solid state electrochemical systems (SEES) there is no common, well accepted model of CV-peak formation up to now. The interpretations of those CV-diagrams are still controversially discussed in literatures [64, 73], and

there are multiple reasons for difficulties in the interpretation of the CV data of the YSZ based SEES and for disagreements, which will be elucidated in detail in the following paragraphs.

On the one hand, the well-established models used for description of liquid electrolyte based electrochemical systems (LEES) [109, 110] cannot be directly applied to YSZ based SEES, because the theory in the wet electrochemistry was proposed and developed to treat the processes in two-phase systems (Fig. 20). In these models, the mass transport processes, including diffusion and adsorption/desorption, are deemed to proceed in the liquid electrolyte and on the electrode surface, respectively, while the electron transfer processes with redox couples are assumed to occur at the electrode/electrolyte interface only. The corresponding CV characteristics of the LEES are interpreted based on those processes and their interactions under electric polarization conditions.

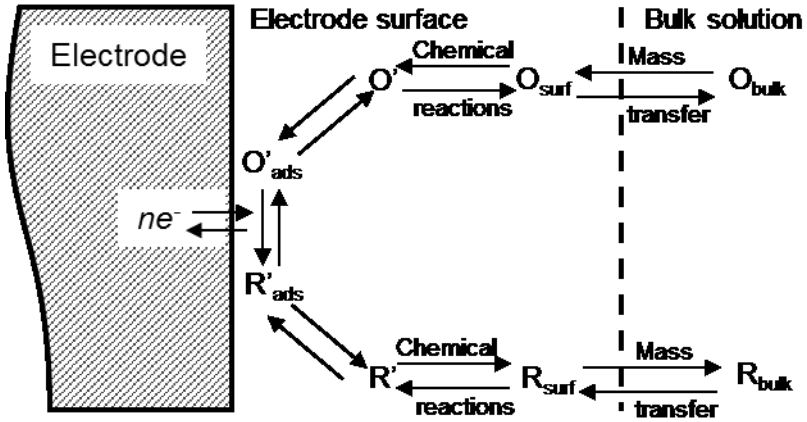

Fig. 20: *General overview of the electrode processes involved in CV measurements for the liquid electrolyte based electrochemical systems (reproduced from [110])*

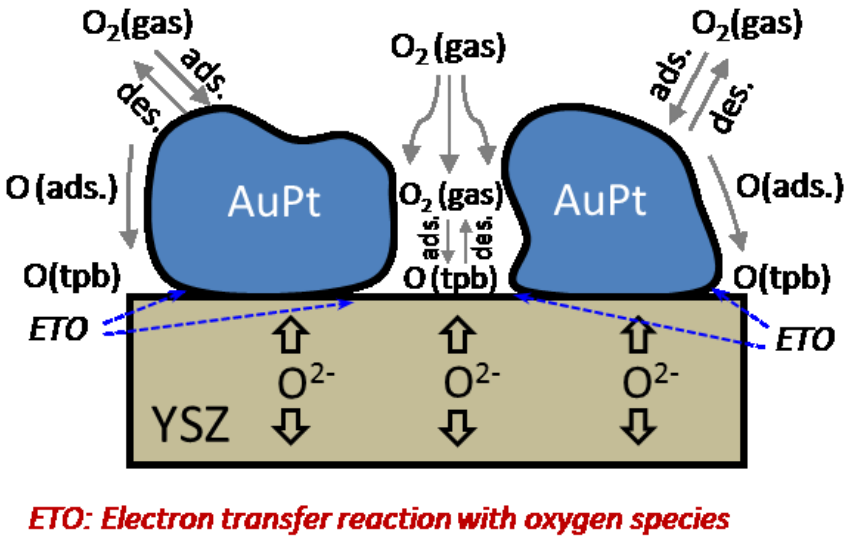

Fig. 21: *Schematic presentation of the possible electrode processes involved in the YSZ based solid state electrochemical system, taking the APE as an example*

However, the situation is clearly different at YSZ based SEES. The most distinct difference from the LEES is that the YSZ based SEES is a three phase system (Fig. 21), which is comprised of the

electrode, the YSZ and the gas atmosphere. The mass transport processes can proceed in more various ways at different locations of the YSZ based SEES compared to the LEES as described in the following. These processes may include (Fig. 21): i) O_2 diffusion in the gas atmospheres to/from the electrode surface; ii) diffusion of O_2 through the pores in the porous electrode layer to/from the TPB and adsorption/desorption at the TPB; iii) O_2 adsorption/desorption on the electrode surface and surface diffusion of adsorbed oxygen species to/from the TPB. It has to be particularly pointed out that the mass transport processes may not only proceed at the side of the gas atmosphere and the electrode, but also occur between the TPB and the YSZ bulk, and in the YSZ bulk itself (Fig. 22). All of these mass transport processes at both sides of the TPB (Fig. 22) have to be taken into consideration when interpreting the influence of the O_2 concentration on the CV characteristics of the type III sensor (Fig. 19). Furthermore, in difference to the LEES, the electron transfer processes at the YSZ based SEES do not take place at the electrode/YSZ interface, but are deemed to proceed at the TPB, the unique location where the oxygen species from the gas phase, the oxide ions (O^{2-}) from the YSZ and the electrons from the electrode are enabled to interact with each other.

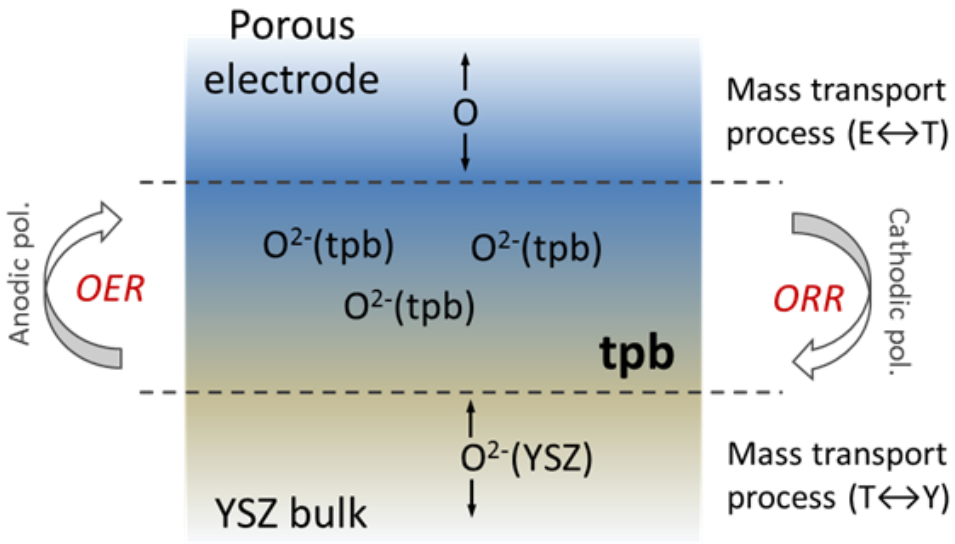

Fig. 22: *Illustration of the current peak formation related processes for the SEES, including the charge transfer reactions at the TPB, and the mass transport processes proceeding from the electrode side to the TPB (E ↔ T) and away from the TPB into the bulk of YSZ solid electrolyte (T ↔ Y).*

On the other hand the previous investigations on the Pt/YSZ system revealed that the reversible changes at the electrode surface or at the electrode/electrolyte interface induced by electric polarization during the CV measurements may be also related to the anodic and the cathodic peak formation in the cyclic voltammograms [64, 73]. They comprise the formation of the spillover oxygen species ($O^{\delta-}$) at the electrode surface and the PtO_x or impurity oxides at the electrode/electrolyte interface in the anodic polarization, and the corresponding reduction processes in the cathodic polarization. These changes have been proven to affect the catalytic activity of the Pt electrode and may influence the CV characteristics of the Pt/YSZ system as well [64, 73, 81, 84, 111].

From all of these aspects addressed above, it can be concluded that the electrode processes involved in the YSZ base SEES are clearly different, and probably much more complicated than those in the LEES. This makes an unambiguous understanding for the CV data of such a system more difficult. Several research groups have tried to interpret the peak formation mechanism in the cyclic voltammograms based on the speculative formation/reduction of the spillover oxygen species ($O^{\delta-}$) at the electrode surface or the PtO_x at the Pt/YSZ interface [73]. However, most of these investigations were carried out under fixed O_2 concentration conditions [64, 73, 88, 112], and therefore the corresponding models were proposed without taking the influence of oxygen concentration into consideration. This makes those models not applicable for the interpretation of the CV data in this work, which were sampled at varied O_2 concentrations (Fig. 19a).

Based on these considerations, a model for interpretation of the CV characteristics of the type III sensor under varied O_2 concentration conditions is proposed here, which, based on a limited data set (Fig. 19a), must be a little bit speculative. For simplification of the discussion, a possible underlying mechanism for the anodic and the cathodic peak formation is only illustrated for 21 vol.% O_2 (Fig. 23), and then the influence of the O_2 concentration in this model is discussed accordingly.

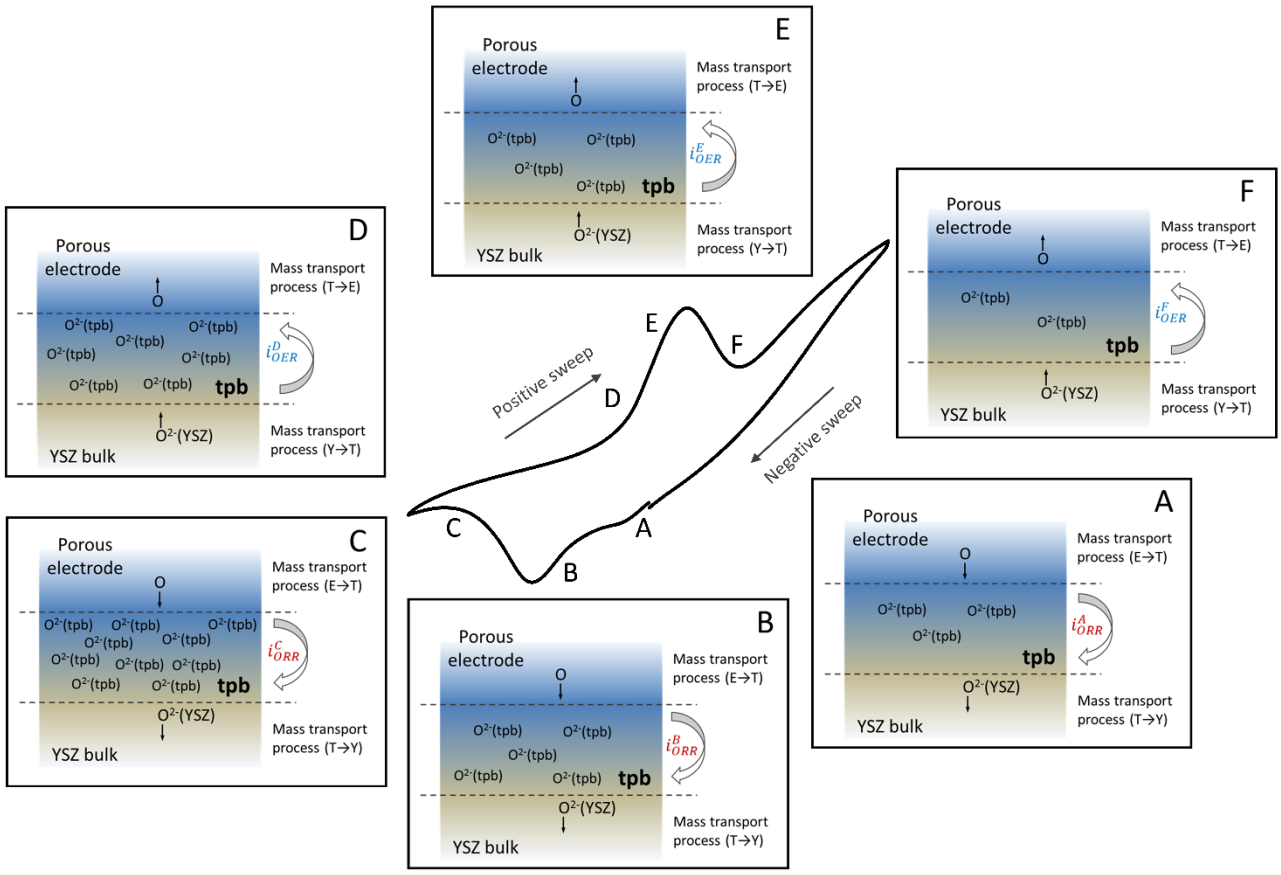

Fig. 23: *Interpretation of the anodic and the cathodic formation processes in the CV profile of the type III sensor at 21 vol.% O_2*

As shown in Fig. 23, when the potential is swept negatively to U_A (Fig. 23 inset A), the current i_{ORR}^{A} starts to incline due to the oxygen reduction reaction (ORR_{CV}) occurring at the TPB (reaction (29)). In an electrochemical way, this faradic process transfers the neutral oxygen species to the oxide ions, both of which are assumed to be located at the TPB.

$$O(tpb) + 2e^- \xrightarrow{cath.\ pol.} O^{2-}(tpb) \qquad (ORR_{CV}) \quad (29)$$

By sweeping the potential to U_B, the faradic current i_{ORR}^{B} is further raised owing to a stronger driving force on the ORR_{CV} by more negative electric polarization. As a result, this would increase the concentration of oxide ions at the TPB (O^{2-}(TPB)) (Fig. 23 inset B), based on the assumption that the transport of the oxide ions from the TPB to the YSZ bulk is slower than the electron transfer process ORR_{CV} at the TPB. When the potential is even more negatively swept, more oxide ions could be accumulated at the TPB due to the transport limitation of the oxide ions away from the TPB to the YSZ bulk, which would consequently further increase the O^{2-}(TPB) concentration (Fig. 23 inset A → B). After the O^{2-}(TPB) concentration exceeds a certain extent, the ORR_{CV} is postulated to be blocked by the accumulation of the oxide ions at the TPB (Fig. 23 inset B → C), and in this way the amount of current i_{ORR}^{C} is expected to be decreased. These series of situations (Fig. 23 inset A → B → C) describe the possible mechanism of the cathodic peak formation, which is based on the competition between the electron transfer process ORR_{CV} and the transport of oxide ions away from the TPB to the YSZ bulk.

For the anodic peak formation (Fig. 23 inset D, E and F), the current is increased from i_{OER}^{D} to i_{OER}^{E} due to the oxygen evolution reaction (OER_{CV}) (reaction (30)) after the positive potential sweep has reached U_D. This process (OER_{CV}) would electrochemically consume the accumulated oxide ions at the TPB, which are produced in the foregoing cathodic polarization procedure, to the neutral oxygen species, and accordingly reduce the O^{2-}(TPB) concentration (Fig. 23 inset D → E). When the pre-formed O^{2-}(TPB) ions are greatly consumed during the positive polarization, the correspondingly induced deficit of these species is expected to depress the OER_{CV}, which is reflected as a reduction of the anodic current in the positive potential sweep (Fig. 23 inset E → F). The current beyond the anodic peak is then solely given by the diffusion of O^{2-} ions from the solid electrolyte (YSZ) to the tpb. That is to say, the formation of the anodic peak is assumed to be originated from the deficit of the oxide ions at the TPB when continuously increasing the positive polarization voltage.

$$O^{2-}(tpb) \xrightarrow{anod.\ pol.} O(tpb) + 2e^- \qquad (OER_{CV}) \quad (30)$$

With respect to the influence of the O_2 concentration, the trend of showing the less pronounced cathodic peak with an exception at 15 vol.% O_2 (Fig. 19a) is presumed to be attributed to the depressed rate of the ORR_{CV} at the reduced O_2 concentration in the gas phase, since the concentration of O(TPB) is supposed to decline with decrease of O_2(gas)-concentration according to e.g. the Langmuir adsorption model. This means, the concentration of the accumulated oxide ions at

the TPB produced during the negative potential sweep is proportional to the O_2 concentration in the gas phase. That is to say, a higher O_2 concentration in the gas phase results in a more production of the oxide ions during the negative polarization, which is reflected as a larger cathodic peak (Fig. 19a). The slightly larger cathodic peak at 15 vol.% O_2 compared to that at 20 vol.% O_2 could result from the electrochemical reduction of the oxidized metallic part of the electrode at the electrode/electrolyte interface by cathodic polarization [64, 71, 88], based on the assumption that those oxidized metallic parts become less stable at a reduced O_2(gas) concentration. Once this electrochemical reduction process takes place at 15 vol.%O_2, the resulting metallic state of the electrode part is assumed to be preserved but not re-oxidized at the electrode/electrolyte interface in the following CV-cycles conducted at the lower O_2 concentrations. Consequently, a further enlargement of the cathodic peak is not observed when again the O_2(gas) concentration is reduced to 10 and 5 vol.%. This hypothetical reduction process may probably increase the electrode kinetics, and can be related to that unexpected higher anodic current around 0.5 V at 15 vol.% O_2 (Fig. 19a, rim).

Concerning the effect of the O_2 concentration on the anodic peak formation, the less pronounced anodic peak at the lower O_2 concentration seems to be well correlated to the smaller cathodic peak at the same O_2 concentration (Fig. 19a). Based on the same discussion in the last paragraph, the decreased concentration of the accumulated oxide ions at the TPB produced during the foregoing cathodic polarization is supposed to be the reason for the smaller anodic peak at the lower O_2 concentration. However, it has to be noted that the anodic peaks are apparently unsymmetric to the cathodic peaks at the same O_2 concentrations. More exactly speaking, the areas under the anodic peaks are clearly smaller than those under the cathodic peaks at 20, 15 and 10 vol.% O_2, and even no anodic peak but only a cathodic peak is found at 5 vol.% O_2. This unsymmetric behavior may probably indicate that not all the oxide ions at the TPB produced during the foregoing cathodic polarization are accumulated at the TPB, but part of them transport into the YSZ bulk after the cathodic peak formation. An extreme situation seems to happen at 5 vol.% O_2, where all the oxide ions produced by cathodic polarization are assumed to be transported away from the TPB, and there is no accumulation of such species in the following positive scan. Consequently no anodic peak was observed at 5 vol.% O_2.

In addition, the CV characteristics of the sensor were also found to be influenced by the presence of CO in the gas atmosphere, as shown in Fig. 24. Surprisingly, the CV profiles at CO exposures, i.e. the shapes of the cathodic and the anodic peaks and their positions on the voltage-scale, were found to be rather similar to those observed at variations of O_2 concentrations (Fig. 19a). These observations motivate the assumption that with and without the CO exposures, the same types of processes dominate the formation of the current peaks in the CV profiles.

But it has to be pointed out that the dependence of the change of the current peaks on CO concentrations is opposite to that on O_2 concentrations. In particular by causing a similar change in

the CV profiles (cf. Fig. 19a and 24), the variation of CO concentration (0 → 1000 ppm) is noted to be much smaller than that of O_2 concentration (20 → 5 vol.%). This could be an indication that, the CO wins the competition of adsorption with O_2 at the TPB, and therefore the concentration of O_{ads}(TPB) is considerably reduced even at such low concentrations of CO. If it is assumed that also in this case the processes with oxygen species (see the model proposed above in Fig. 22 and 23) dominate the CV characteristics of the sensor, this would consequently change the CV profiles under CO exposure, i.e. the cathodic as well the anodic peak are depressed with increase of CO concentration.

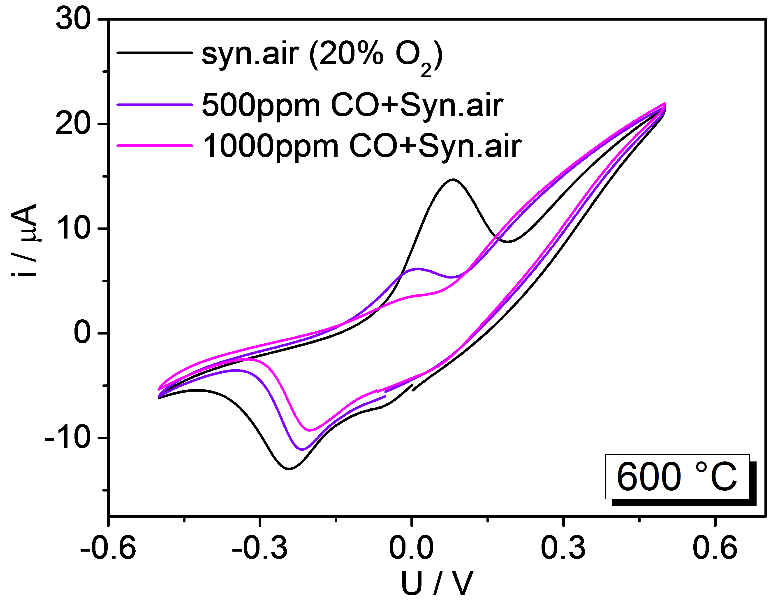

Fig. 24: *CV characteristics of a type III sensor at 600 °C under exposure to 0, 500, 1000 ppm CO balanced with synthetic air*

4.2.2 Case study II – EIS investigation of a type I sensor

Besides the characterizations by CV measurements, a type I sensor was investigated with EIS measurements at 600 °C under exposure to 20, 15, 10 and 5 vol.% O_2 separately, as shown in Fig. 25. All the Nyquist plots of the impedances measured in the range from 10 kHz to 2 mHz were observed to be resolved into two quasi-semicircles (Fig. 25). The first semi-circles in the high frequency regime were found to be smaller than the second ones and almost not influenced by the variation of O_2 concentration. However by decreasing the O_2 concentration, the radius of the second quasi-semicircles in the low frequency regime were noted to be clearly increased.

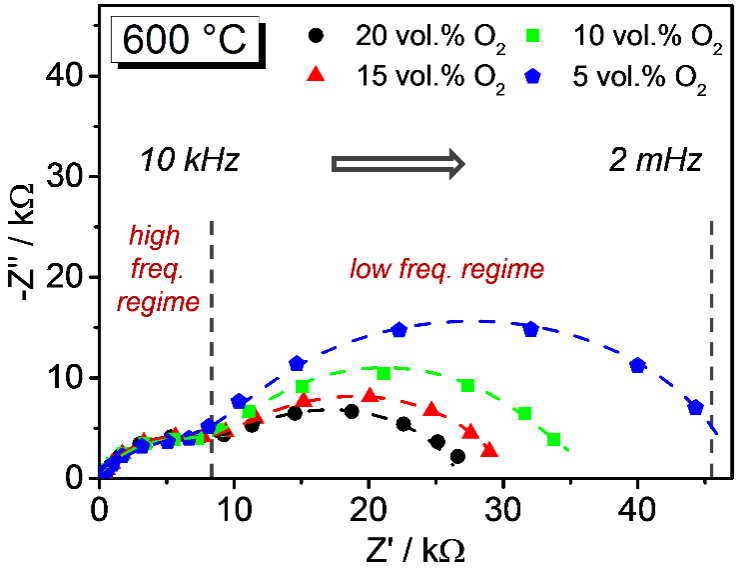

Fig. 25: *EIS characteristics of a type I sensor at 600 °C under exposure to 20, 15, 10 and 5 vol.% O_2 separately*

These well-resolved quasi-semicircles reflect different kinds of charge transport/transfer processes proceeding in the solid electrolyte (YSZ) and at the electrode/electrolyte interface (Au,Pt-YSZ/YSZ), respectively (Fig. 21). Due to the fact that the semi-circles with smaller radius in the high frequency regime are nearly independent on the variation of O_2 concentration (Fig. 25), they are assumed to represent the O^{2-} ion transport process in the solid electrolyte, including the O^{2-} ion transport in the YZS grains and across the grain-grain boundaries. Correspondingly, the larger semi-circles in the low frequency regime showing increased radius by decreasing O_2 concentration are postulated to be related to the electron transfer reaction with oxygen species at the Au,Pt-YSZ/YSZ interface (Fig. 22). These findings are well consistent with the results of the investigations on Pt/YSZ/Pt system, as reported in [113]. Based on these assumptions, it could be inferred that, i) the time constant of the O^{2-} ion transport process in the YSZ is smaller compared to that of the electron transfer reaction with oxygen species at the Au,Pt-YSZ/YSZ interface, and ii) the O^{2-} ion transport process proceeds at a higher rate than the electron transfer reaction at the electrode/electrolyte interface at the quasi-steady-state conditions without significant electrical polarization on the electrode.

For further analysis of the EIS data, these quasi-semicircles in the high and the low frequency regime measured at different O_2 concentrations are extrapolated to the real axis, separately. The polarization resistances of the interfacial electron transfer reactions ($R_{interface}$) at different O_2 concentrations can be calculated by subtracting the interception of the smaller semicircle to the real axis from that of the corresponding larger semicircle to the real axis at the same O_2 concentration. By plotting the $1/R_{interface}$ over the O_2 concentration both on a logarithmic scale, the logarithm of $1/R_{interface}$ was found to be linearly dependent on the logarithm of the O_2 concentration as shown in Fig. 26. The slope of this linear dependence is estimated to be approx. 0.49. According to [114, 115], the $1/R_{interface}$ is proportional to the exchange current density ($j^0_{O_2}$) of the thermo-dynamic equilibrium of oxygen reaction, and can be expressed as following:

$$1/R_{interface} \propto (k_\varepsilon k_{-\varepsilon} a_O a_\sigma)^{1/2} \tag{31}$$

where k_ε and $k_{-\varepsilon}$ are the forward and the backward rate constants of the thermo-dynamic equilibrium of oxygen reaction, respectively. a_O and a_σ are surface oxygen activity and vacant site activity on the APE, respectively. As well described in [110], the $1/R_{interface}$ may be proportional to different orders of oxygen concentration in gas phase, depending on the rate determining step in the electrode process and the corresponding number of electrons involved in the charge transfer step. The value 0.49 observed in this work suggests that the electrode processes of the type I-sensor may include a four-electron transfer step with associatively adsorbed oxygen species controlled by the Langmuir adsorption (Expr. 32), as shown in Expr. 33

$$a_O/a_\sigma \propto C_{O_2} \tag{32}$$

$$1/R_{interface} \propto a_\sigma C_{O_2}^{1/2} \tag{33}$$

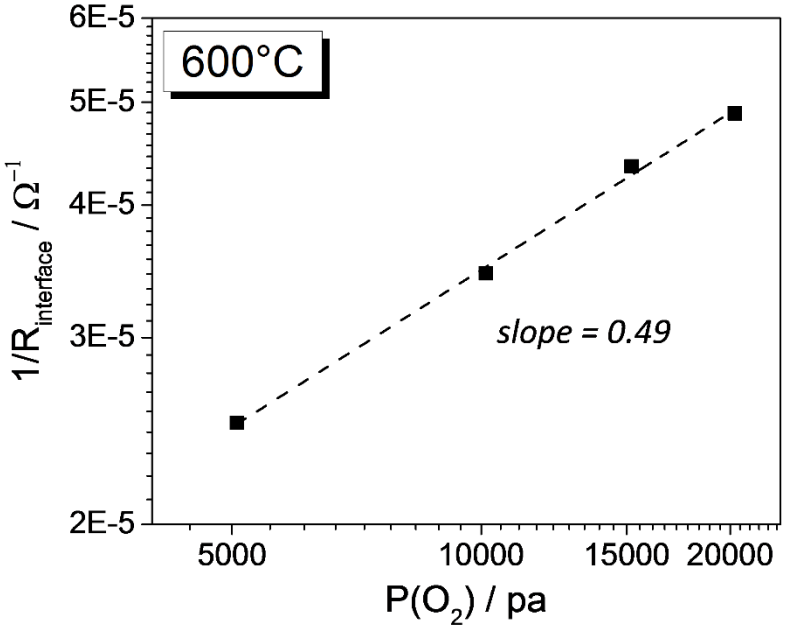

Fig. 26: *Dependence of $1/R_{interface}$ on O_2 concentration on logarithmic scale for the type I sensor at 600 °C*

With these two case studies, it is shown that combined CV and EIS offer possibilities to extract information about the electrode processes involved in the mixed-potential formation, which cannot be resolved and analyzed from the ΔU measurements under OCP conditions only. These aspects will be further discussed in Sec. 4.3 where the long term stability of the sensor is concerned and a sensitivity regeneration concept by cathodic polarization based on the correlation of the sensing characteristics with the electrode kinetics is proposed for the first time.

4.3 Selectivity, response stability and recovery by cathodic polarization

4.3.1 Selectivity and stability of the sensor

In addition to their response to CO, these types of sensor are also sensitive to other oxidizable gas species at elevated temperatures, such as H_2 (hydrogen), CH_4 (methane) and C_3H_6 (propene). As an example, sensing responses of a type II- and a type III-sensor under exposure to these gas species balanced with synthetic air at 650 °C are shown in Fig. 27 a-d and e-g, respectively.

Generally, the measured ΔU vs. reference half-cell Pt/YSZ was negative at all test gas exposures (Fig. 27). By plotting the sensitivity of the type II- and the type III-sensor to different test gas species at 1000 ppm concentration on a logarithmic scale (Fig. 28), the highest response is found in H_2 containing gases for both type II- and type III-sensor, while the lowest response is observed in CH_4 containing gases. This is probably due to the faster kinetics of H_2 adsorption, diffusion & electrochemical oxidation, and the relatively more stable chemical/molecular structural property of CH_4 compared to the other test gas species [116].

On the other hand, stable and reversible response behaviors were only found in CH_4, CO and H_2 containing sample gases (Fig. 27 a-c and e-g). The corresponding measurements under exposure to C_3H_6 resulted in clear asymmetric response comparing upward and downward stepwise changes of concentrations (Fig. 27 d&h). Steps of concentration increase/decrease are observed by a sharp rise/moderate decay of the potential at each instant of concentration change followed by potential relaxation. These two phenomena might reflect a fast potential generating process and an additional, relatively slow process running simultaneously. This slow process might change the location of potential generation, i.e. the APE/YSZ interface continuously, and might cause some irreversible potential changes and instability which is discussed again in more detail below.

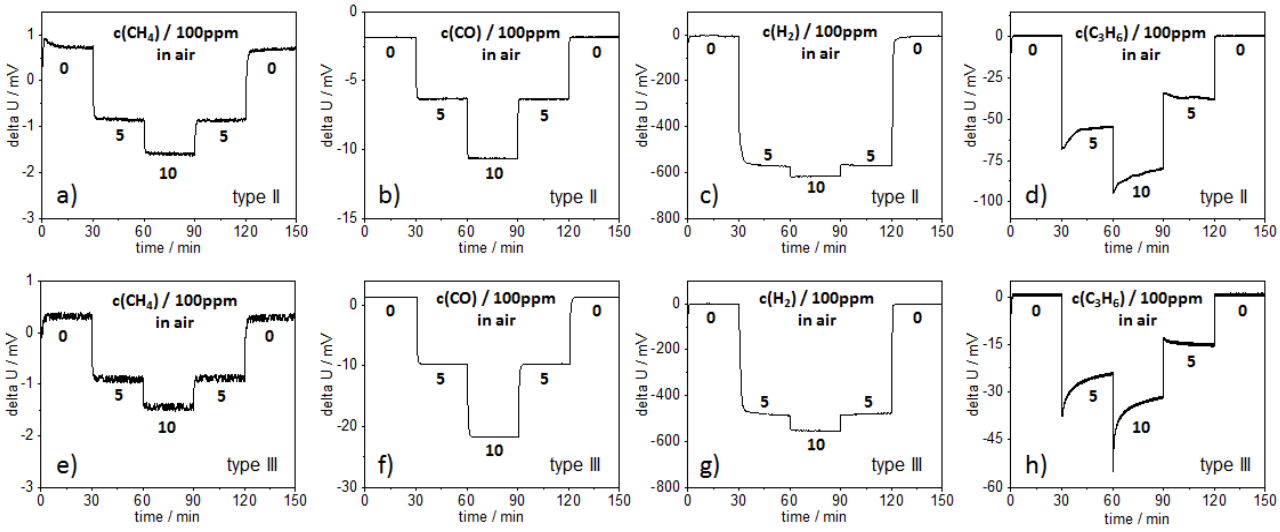

Fig. 27: *ΔU vs. time response behaviors of the type II- (a-d) and the type III-sensor (e-h) at 650 °C under exposure to various concentrations of CH_4, CO, H_2 and C_3H_6 at 20.5 vol.% O_2, separately.*

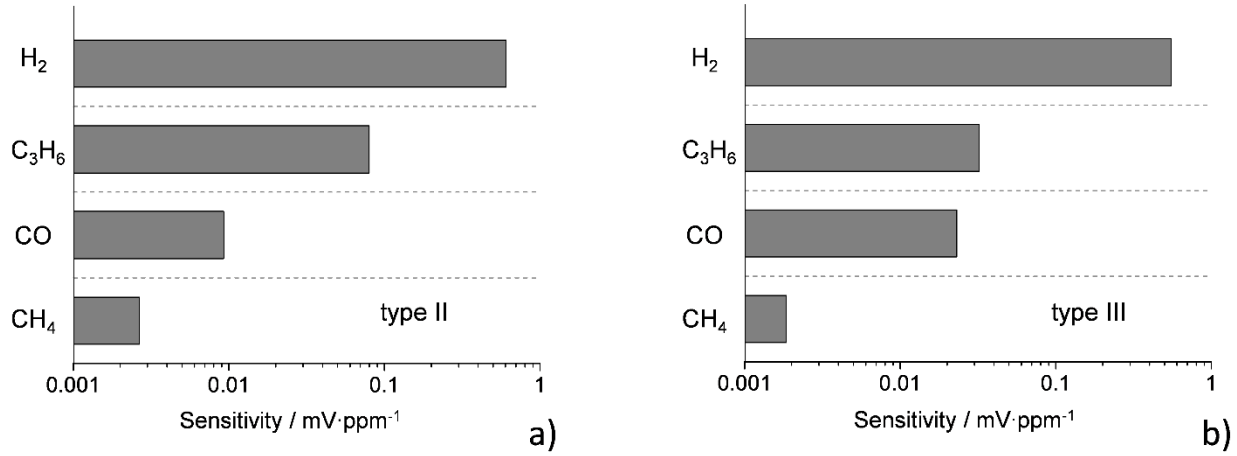

Fig. 28: *Comparison of the sensitivity of (a)the type II- and (b) the type III-sensor at 1000 ppm gas concentration in air (gas= CH_4, CO, H_2 and C_3H_6). The sensitivity is calculated according to* $S = \frac{\partial \Delta U}{\partial c(gas)}$ *at 1000 ppm of different kinds of gas species, respectively.*

Under gas exposure over 12h, both type II- and type III-sensor showed stable response behaviors to H_2 and CO, while clear sensor response losses were observed in C_3H_6 sensing experiments (Fig. 29). During the experiments coking layers are formed at the sensing electrodes of both types of sensor at C_3H_6 exposure (Fig. 30), but not observed in the H_2 and CO sensing tests. Interestingly, the coking layer formed on the type III-APE is distributed more homogeneously than that on the type II-APE, which is a further indication that Pt and Au are alloyed more homogeneously on the sensing electrode of type III-sensor due to the longer annealing procedure at higher temperature in the sensor preparation (Tab. 1, Sec. 3.1). This observation is in good accordance with the results of the surface morphological and crystal studies of the APEs shown in Fig. 12 & 13 (Sec. 4.1.1). These coking layers might be formed by decomposition of C_3H_6 molecules at Pt [117] according to the reaction below :

$$C_3H_6 \xrightarrow{Au/Pt} 3C_{ads} + 3H_2 \tag{34}$$

With respect to the potential drift and degradation only observed under C_3H_6 exposure (Fig. 27 & 21), it is assumed, that some irreversible changes at the location of potential generation, i.e. at the APE/YSZ interface, are responsible for this instability. Hypothetically, this could be correlated with the formation of carbon (coking), but this has to be further investigated.

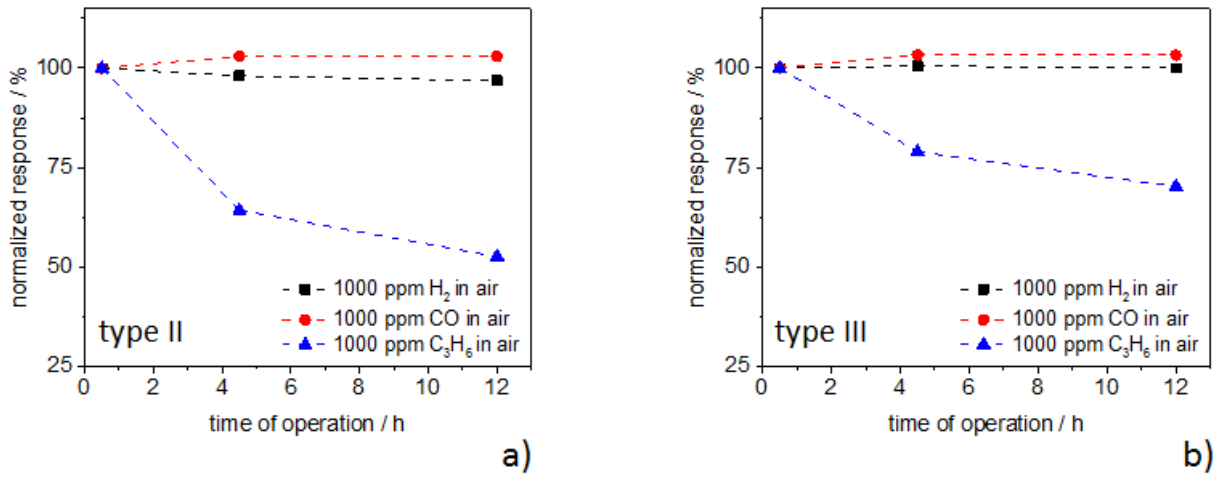

Fig. 29: *Change of response behaviors of (a) a type II- and (b) a type III-sensor measured under the same gas conditions but at different stage of H_2, CO and C_3H_6 test separately*

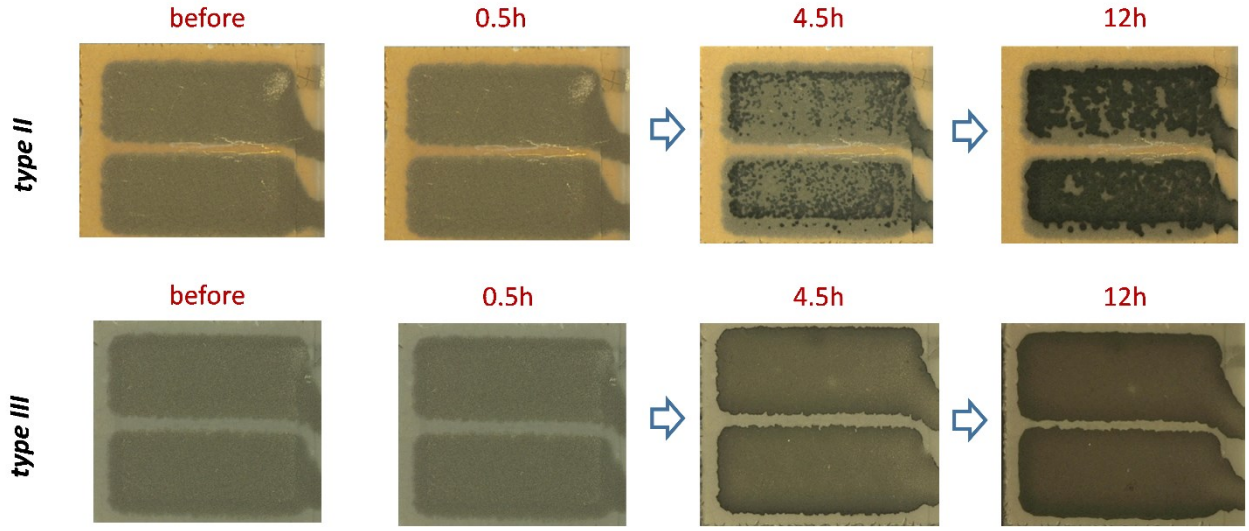

Fig. 30: *Optical images of surface change of the type II- and the type III-APE before and under exposure to propene after 0.5h, 4.5h and 12h*

Furthermore compared to those stability tests under gas exposure for 12h as discussed above, the stability of CO response of the type III-sensor was investigated on a much more extended time scale over 100 days, while the sensors were mainly operated at 600 °C in ambient air. Fig. 31 and Fig. 32 show the sensing responses to CO and the corresponding EIS characteristics of a type III-sensor in synthetic air at 600 °C at different stages of the experiment, respectively. This type III-sensor was a fresh one, which was not exposed to any CO, H_2 or C_3H_6, but only kept in ambient air at room temperature before used in these stability tests.

The ΔU was measured to be -66 mV at a CO concentration of 1000 ppm on the 1st day. This value was slightly increased to -62 mV after 47 days of operation at 600 °C in ambient air. By prolonging the operation time under such condition (600°C, in ambient air) for another 53 days, a drastic reduction of the response to only 33% (-22 mV) of the initial value was surprisingly observed after a total operation time of 100 days. Moreover, it has to be noted that a slightly positive shift of the baseline from 0.3 mV to 2.1 mV was measured in synthetic air (Fig. 31).

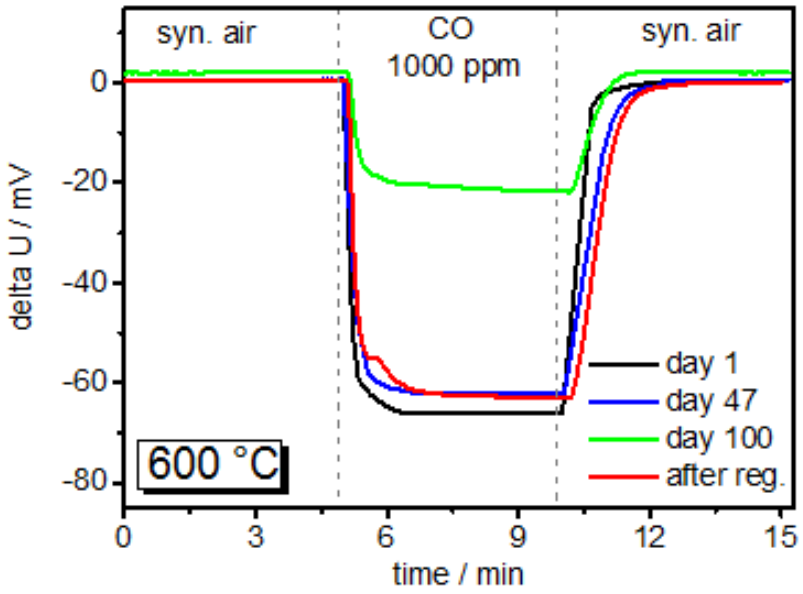

Fig. 31: *OCP responses of the type-III sensor to CO at 600 °C on the 1st, 47th and 100th day, and after polarization of the APE*

These changes of the ΔU values in the OCP measurements (Fig. 31) are well correlated with the changes of the EIS measurements recorded after each OCP test, as shown in Fig. 32. A quasi-semicircle with a polarization resistance (R_p) of 7.1 kΩ was measured on the 1st day in synthetic air at 600 °C. After 47 days' operation, the Nyquist plot measured under the same condition held the shape of a quasi-semicircle, but the R_p was enlarged to about 35 kΩ. However, only an incomplete semicircle was measured after 100 days, and the R_p was calculated to be 434 kΩ after a numerical complementation of the semicircle, which was drastically increased compared to those measured before.

By applying cyclic negative potential scans to the APE (Sec. 3.4), the ΔU measured at the CO concentration of 1000 ppm (Fig. 31) was almost recoverd to the value measured on the 47th day, and the baseline in synthetic air was varied back as well. Simultaneously, an EIS characteristic very similar to the state on 47th day was measured after this polarization procedure (Fig. 32). The effect of the cyclic cathodic polarization on the APE is found to be strongly influenced by both the temperature and the number of potential scans. This aspect will be discussed in detail in the next section.

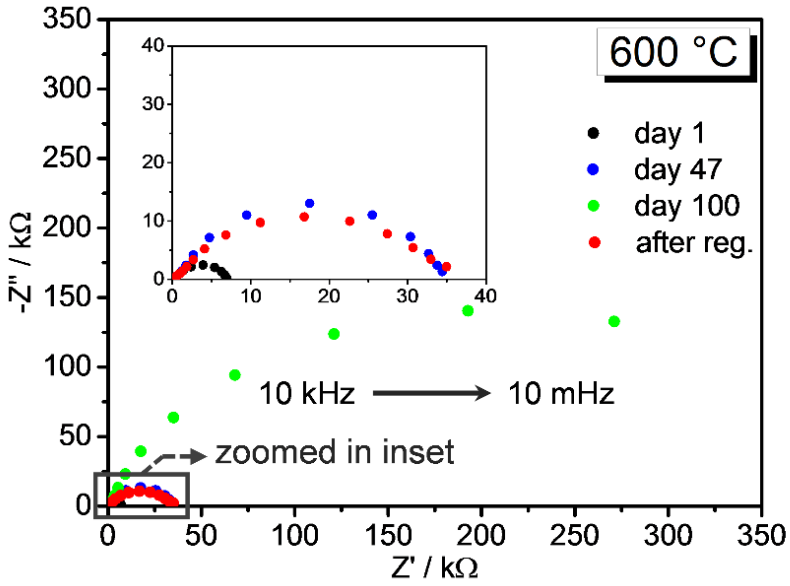

Fig. 32: *EIS characteristics of the type III-sensor in synthetic air at 600 °C on the 1st, 47th and 100th day, and after polarization*

From these OCP and EIS measurements, it can be concluded that the APE/YSZ interface, i.e the location of potential generation, is changed over time by operating the sensor at 600 °C in ambient air. The change of the APE/YSZ interface seems to proceed at a relatively slower rate in the first 47 days, which is reflected by a moderate increase of R_p in the EIS measurement and a slight reduction of response in the OCP measurement (Fig. 31). But then this change proceeds at a much faster rate from 47th day to 100th day indicated by a drastic increase of R_p and a correspondingly considerable reduction of OCP response. The application of the negative potential scans only results in very similar electrochemical behaviors (OCP response (Fig. 31) and EIS characteristics (Fig. 32)) of the APE as measured on 47th day, but cannot yield the initial characteristics as measured on 1st day.

Based on these results, it can be infered that the aging process brings about both irreversible (from 1st to 47th day) and reversible changes (from 47th to 100th day) at the APE/YSZ interface. Hypothetically, the irreversible changes might be caused by accumulation/ agglomeration of impurities at the electrode/electrolyte interface or redistribution of Au within the electrode layer, while the reversible changes are probably related to an oxidation phase of the metallic parts of the APE at the TPB [64, 88-90].

According to the results reported in [64, 88, 89], the increased R_p and the change of the shape in the EIS characteristics, which can be restored by cathodic polarization, are related to those reversible changes at the APE/YSZ interface and indicate the oxidation of the metallic parts of the APE at the TPB. This would result in a decrease of the concenration of the active electrochemical reaction sites in the potential forming processes, and accordingly depress the mixed potential formation under exposure to CO and positively shift the base-line in air. These oxidized parts seem to be reduced again to the metallic state by cathodic polarization at 700 °C. As a result, those blocked reaction sites

are assumed to be reactivated as well, and accordingly very similar OCP (Fig. 31) and EIS characteristics (Fig. 32) are observed as those before the aging was started.

4.3.2 Effect of cathodic polarization on the layered Au,Pt-YSZ electrodes at different temperatures

As already briefly discussed in the last section (Sec. 4.2.1), the application of cyclic cathodic polarization on the APE at 700 °C enables regeneration of its response to CO, when a reduction of response had been found after a 100 days' aging procedure in ambient air. Further experiments revealed that the temperature, at which the polarization is conducted, and the number of potential scans both play an important role on the efficiency of the response regeneration.

Fig. 33 shows the OCP responses of an aged type III-sensor to 1000 ppm CO in air measured before and after the application of cathodic polarization sequences at different temperatures between 600 – 700 °C at 5 vol.% O_2. A small enhancement of the OCP response to CO is found after five cathodic potential scans in the range between 0 and -0.6 V at 600 °C. The response enhancement gets more and more enlarged by increasing the temperature during polarization. A significant response enhancement is obeserved after polarizing the APE at 700 °C with five potential scans, and the response is even further raised to almost the initial value of this sensor before aging by another 25 potential scans at the same temperature (Fig. 33).

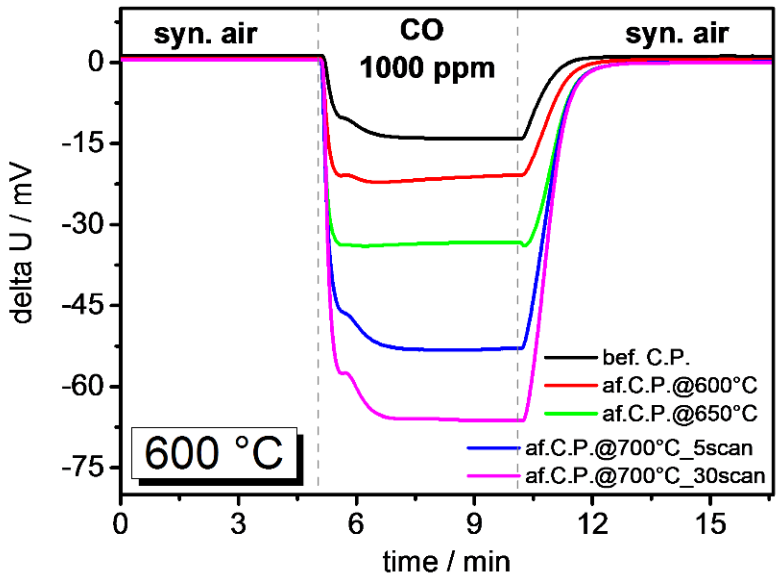

Fig. 33: *OCP responses of the aged type III-sensor under exposure to CO (1000 ppm) in air before and after polarization at 600, 650 and 700 °C*

According to the other electrochemical investigations of Pt/YSZ and Au/YSZ interfaces in [64, 73, 77, 88, 89, 118], it is assumed that the cathodic polarization applied on the APE could not only induce the oxygen reduction reaction (reaction (6), Chap. 2) but also reduce the oxidized metallic parts of the APE at the TPB, which is assumed to be formed in the aging process, in an electrochemical way according to the following reaction:

$$AuPtO_x + 2xe^- \rightarrow AuPt + xO^{2-} \tag{35}$$

This would increase the concenration of the active electrochemical reaction sites at the TPB, and therefore enhance the charge transfer processes proceeding there, for example the mixed potential formation, as discussed in Sec. 4.2.1.

With respect to the role of temperature, the reason for the better response enhancement by polarization at higher temperatures could be two-fold: i) the kinetics of the electrochemical reduction of $AuPtO_x$ at the TPB is increased by raising the temperature, and accordingly result in a faster decomposition of $AuPtO_x$ by cathodic polarization at the higher temperature; ii) the formation of $AuPtO_x$ becomes less and less stable at more and more elevated temperatures, which enables an easier and relatively thorough electrochemical reduction of $AuPtO_x$ at the TPB. The latter aspect is in good consistency with the results reported in [89].

To prove these hypotheses, complementary CV and EIS measurements were carried out on the sensor as well. These studies bring a deeper knowledge about the effects of the cathodic polarization and the role of temperature during the polarization on the electrochemical characteristics of the electrode/electrolyte interface. Fig. 34 shows the currents measured over the 1^{st}, 3^{rd}, 5^{th} and 30^{th} potential scan of the cyclic cathodic polarization on the APE at 5 vol.% O_2 and 700 °C, separately. Slight rise of current is observed from the 1^{st} to the 5^{th} scan, while the current is found to be considerably increased in the 30^{th} scan compared to those measured in the first five scans. This means, the rate of the charge transfer process (herein, the oxygen reduction reaction ORR(reaction (6), Chap. 2)) rises by polarizing the APE cathodically, and is more and more raised by increasing the number of scans.

Moreover, it is noted that the hysterisis of these i-U envelope curves becomes also significantly smaller with increasing the number of potential scans. The relatively larger hysterisis of the i-U curves in the 1^{st}, 3^{rd}, and 5^{th} scan is an indication of a capacitive characteristic at the APE/YSZ interface, which is propably induced by the oxidation of the metallic parts of the APE at the TPB during the aging process. As already discussed above, the cathodic polarization is assumed to enable the electrochemical reduction of those oxidized metallic parts at the TPB, and accordingly lower the capacitive characteristic of the APE/YSZ interface, which is reflected by the diminished i-U hysterisis and the increased current in the measurement.

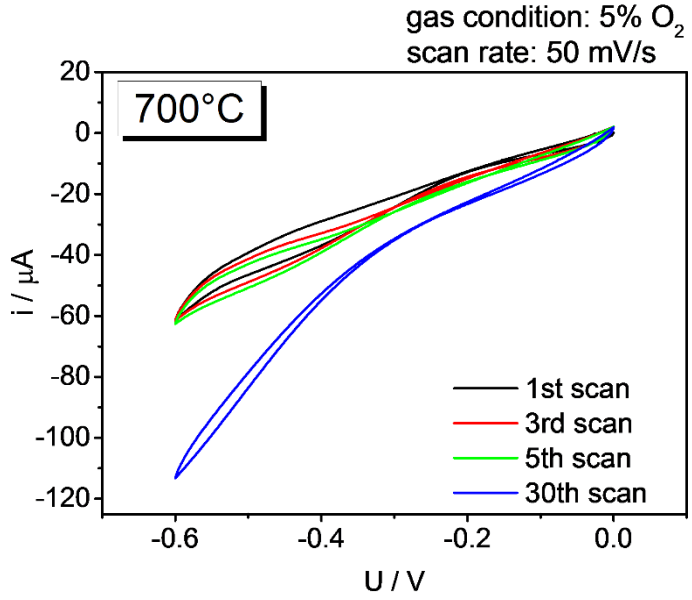

Fig. 34: *Cyclic voltammogram sampled in the 1st, 3rd, 5th and 30th scan in the cathodic polarization of the type III-APE at 5 vol.% O_2 and 700 °C*

The EIS measurements were carried out at the same intermediate states of the cathodic polarization treatment. Fig. 35 shows EIS characteristics of the aged type III sensor measured at 600 °C in synthetic air before and after the cathodic polarizations at different temperatures between 600 – 700 °C at 5 vol.% O_2. Before polarization, the Nyquist plot depicts the shape of an incomplete quasi-semicircle with the largest R_p in synthetic air at 600 °C compared to those measured after polarization under the same condition.

By cathodically polarizing the APE at higher temperatures and later increasing the number of scans at 700 °C, the shape of the Nyquist plot develops more and more to a complete semicircle, while the value of the corresponding R_p gets smaller and smaller. The opening at the incomplete semicircle is an indication of the phase shift between the AC-perturbance and the yielding AC-current across the TPB. This phase shift is determined by the capacitive characteristic of the APE/YSZ interface. The shape change of the Nyquist plot from the incomplete to the complete quasi-semicircle and the reduction of the R_p reveals that the APE/YSZ interface becomes less capacitive after polarization, while the exchange current density for the oxygen thermodynamic equilibrium (reaction (4), Chap. 2) gets increased. These measurements again confirm the correlation of the better OCP response to CO (Fig. 33) with the less capacitive but more conductive characteristics of the APE/YSZ interface.

The changes of the EIS (Fig. 35) and the CV characteristics (Fig. 34) induced by polarization, and their corresponding correlation with the OCP response (Fig. 33) support well the assumptions discussed above: the APE/YSZ interface is electrochemically reduced by the cathodic polarization, and this results in a higher concentration of the active electrochemical reaction sites at the TPB and correlates with a larger mixed-potential formation under CO exposure, namely, a higher OCP response to CO. The enhancement of the effect of the cathodic polarization on the APE by raising the

temperature is attributed to the instability of the $AuPtO_x$ at the TPB and the fast kinetics of the corresponding electrochemical reduction reaction (reaction (35)) at higher temperatures.

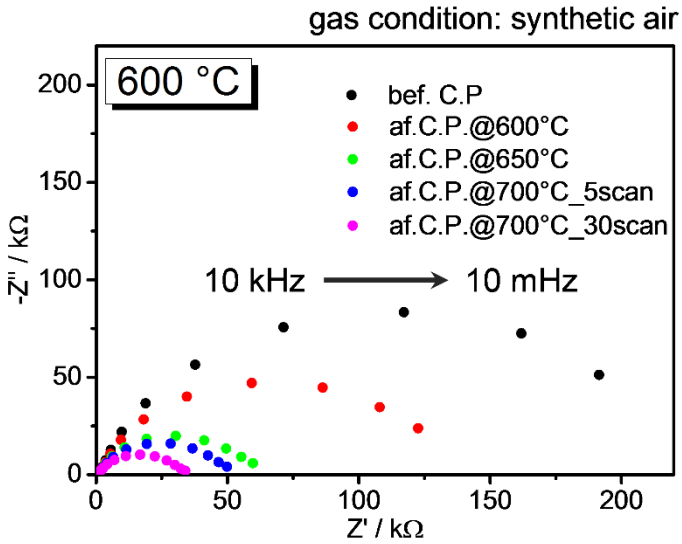

Fig. 35: *EIS characteristics of the aged type III-sensor at 600 °C in synthetic air before and after polarization*

In order to further separate the role of temperature and cathodic polarization in the response regeneration, another individual of type III-sensor, which was aged in ambient air at 600 °C over approx. three months and afterwards lost sensitivity, was tried to be regenerated in two steps: i) heating up the sensor to 700 °C in synthetic air for 2h; ii) in a later step cathodically polarizing the sensor at 700 °C in synthetic air. Fig. 36 shows the response change of this sensor (noted as 11#) by temperature treatment and polarization in synthetic air separately. In addition, this is compared with the response regeneration of the other sensor (noted as 9#) discussed above, which was polarized at a reduced oxygen concentration (5 vol.%). The response change is calculated according to the following equation:

$$response\ change = \frac{\Delta\ U\ (measured)}{\Delta\ U\ (initial)} * 100\% \tag{36}$$

where the ΔU is measured under exposure to 1000 ppm CO in air at 600 °C. The response of the 11# sensor was reduce to approx.15% of the initial value after the aging process. By heating up the sensor to 700 °C in synthetic air for 2h, the reduced response was raised to about 32%, probably due to the partially thermal decomposition of $AuPtO_x$ at the TPB, which blocks the mixed potential formation.

A significant regeneration from 32% to almost 100% was observed by additional polarization under the same temperature and gas condition within only twelve minutes. These regenerations by different methods indicate that, the cathodic polarization at 700 °C is the major driving force for the decomposition of the $AuPtO_x$ than meerly elevating the temperature. That is to say, a small portion of the $AuPtO_x$ at the TPB is thermally decomposed by elevating the temperature to 700 °C, but a thorough decompostion is achieved via electrochemical reduction induced by cathodic polarization.

Moreover it was found that, the effect of the polarization and the corresponding response regeneration are independent on the oxygen concentration. The response can be nearly 100% regenerated, no matter whether the polarization is conducted in synthetic air with 20.5 vol.% O_2 (11#) or at a reduced concentration of 5 vol.% O_2 (9#).

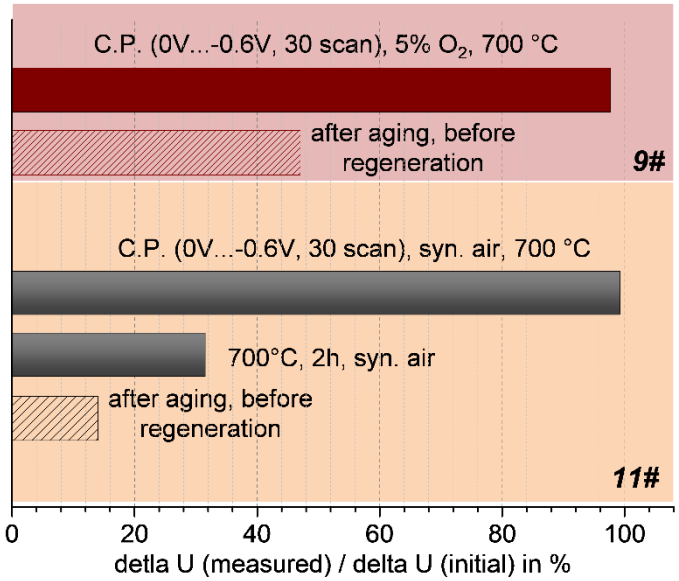

Fig. 36: *Response regeneration of two type III-individuals by temperature treatment and polarization under different conditions*

4.4 Effect of temperature on electrochemical characteristics of the sensor

The effect of operation temperature on the electrochemical characteristics of a type II-sensor was studied by OCP, CV and EIS measurements. The sensing response to CO is decreased by elevating temperatures (Fig. 37). At variation of temperature in steps of ΔT=50 K, a more remarkable reduction of the response is observed when the temperature is increased from 550 °C to 600 °C compared to the change at the temperature step from 500 °C to 550 °C (Fig. 37). Only very slight response to CO is found at 650 °C, and it gets nearly vanished at 700 °C.

From the CV measurements under exposure to dry synthetic air, it is found that the current measured both in the anodic and the cathodic region first increases slightly from 500 °C to 550 °C, and then rises considerably when raising the temperature to 600 °C (Fig. 38 a). By further elevating the temperature to 650 °C and 700 °C, much higher currents are observed compared to those measured below 600 °C. In other words, the rate of the electrochemical reaction involving oxygen is raised at elevated temperatures as expected, but shows a sharp rising when the temperature is higher than 550 °C.

The reason for the decline of the response at elevated temperatures (Fig. 37) could be two-fold: i) the enhanced gas phase reaction of carbon monoxide (reaction (3), Chap. 2), and ii) the increased rate of the oxygen reduction reaction (reaction (6), Eq. (8) Chap. 2). Due to the fact that the currents measured at 500 °C and 550 °C vary only slightly, the response reduction might be mainly related to the enhancement of the CGR (reaction (3), Chap. 2) in this temperature range. However, the sharp reduction of the response from 550 °C to 600 °C might probably be a consequence of both processes. The almost vanished OCP response to CO (Fig. 37) but together with the significantly increased current in the CV measurement in synthetic air (Fig. 38) disclose a very strong domination of the ORR (reaction (6), Chap. 2) in the mixed potential formation in relation to the EOC (reaction (5), Chap. 2) at 650 °C and 700 °C.

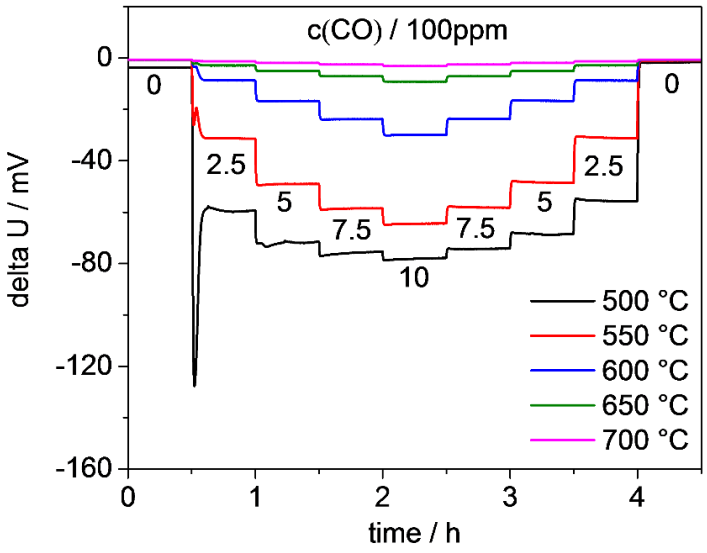

Fig. 37: *Response behaviors of a type II sensor under exposure to CO balanced with 20.vol.% O_2/N_2 between 500°C and 700°C.*

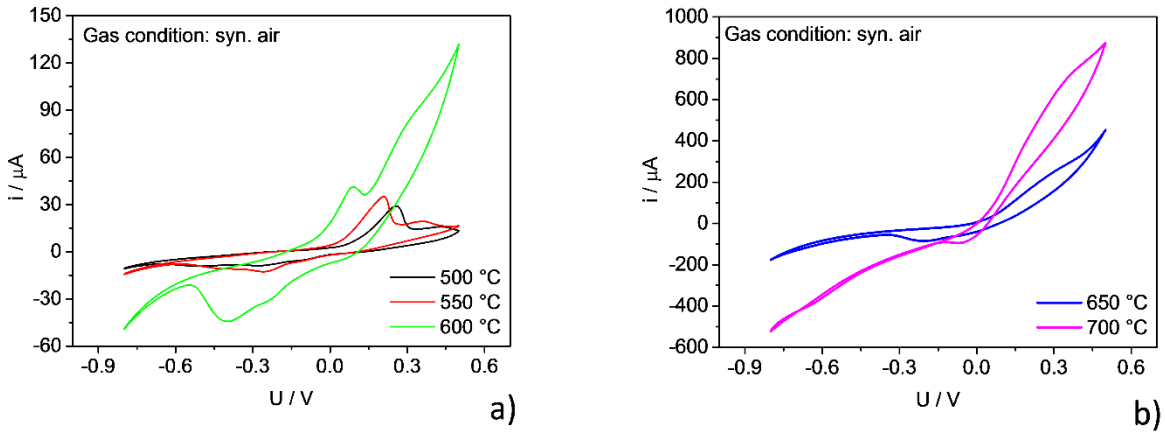

Fig. 38: *cyclic voltammograms of the type II-sensor sampled in synthetic air at (a) 500 °C, 550 °C, 600 °C, (b) 650°C and 700 °C*

The EIS data measured in the same temperature range (500 °C – 700 °C) at synthetic air (Fig. 39) show a good correlation with the results of the OCP and the CV measurements, and also support the interpretation of the response reduction at elevated temperatures as discussed above. As shown in Fig. 39, Nyquist plots of the impedance of the electrochemical cell Au,Pt-YSZ/YSZ/Au,Pt-YSZ were measured in the range from 10 kHz to 10 mHz in synthetic air at 500 °C, 550 °C, 600 °C, 650°C and 700 °C, separately. These Nyquist plots show only one quasi-semicircle, and neither Warburg impedance nor electrode blockage is observed.

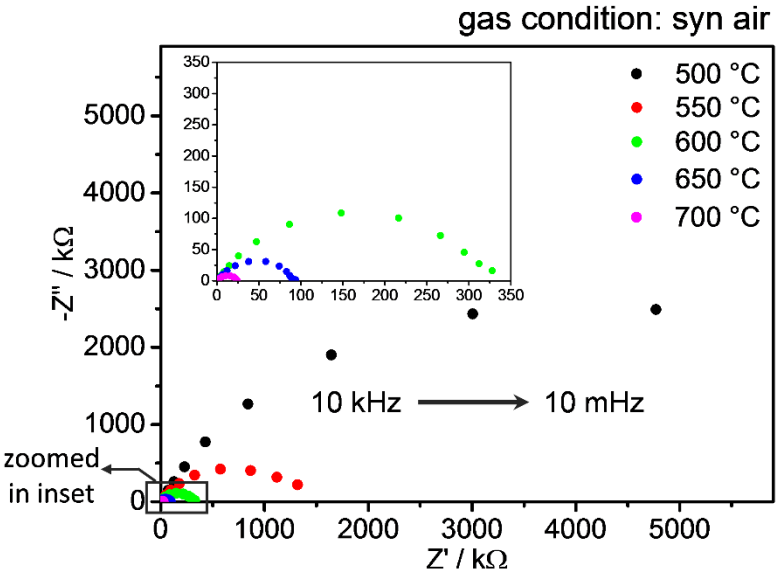

Fig. 39: *EIS characteristics of the electrochemical cell Au,Pt-YSZ/YSZ/Au,Pt-YSZ in synthetic air at 500 °C, 550 °C, 600 °C, 650°C and 700 °C*

The impedance of the YSZ-based electrochemical cell is a synthesis of an interfacial contribution (electrode/electrolyte) and a bulk contribution (electrolyte), which are determined by the charge transfer process at the electrode/YSZ interface and the transport of O^{2-} ion in the YSZ, respectively. According to McDonald et al. [113], the O^{2-} ion transport in YSZ is related to the part of the Nyquist plot in the high frequency regime, while the charge transfer process at the electrode/YSZ interface is represented in the low frequency regime. This means in the electrochemical cell, the rate of the O^{2-} ion transport in YSZ is faster than that of the interfacial charge transfer process. In some cases, the

Nyquist plot shows two semicircular arcs, which depends strongly on the selection of the electrode material. This observation of two semicircular arcs in the Nyquist plot indicates that, even though the O^{2-} ion transport in YSZ proceeds faster than the interfacial charge transfer process, the rate difference of these two processes in the electrochemical cell is not significant but to some extent comparable. However, the finding of only one quasi-semicircle (Fig. 39) in the impedance spectra of the electrochemical cell Au,Pt-YSZ/YSZ/Au,Pt-YSZ reveals that the rate of the charge transfer process at the Au,Pt-YSZ/YSZ interface is drastically slower than that of the O^{2-} ion transport in YSZ. In other words this means, the impedance of the electrochemical cell Au,Pt-YSZ/YSZ/Au,Pt-YSZ is strongly dominated by the Au,Pt-YSZ/YSZ interfacial contribution.

With regard to the influence of temperature, the radius of the Nyquist plots gets reduced by raising the temperature (Fig. 39), which is well correlated with the increase of current in the CV measurement at elevated temperatures (Fig. 38). These changes of the EIS and the CV characteristics in response to the temperature increase are attributed to the enhancement of both the O^{2-} ion transport in YSZ and the charge transfer process at the Au,Pt-YSZ/YSZ interface at higher temperatures. Furthermore, these Nyquist plots measured at different temperatures are extrapolated to the real axis, and logarithms of the corresponding interceptions are plotted over 1000/T (Arrhenius plots), as shown in Fig. 40. Due to the strong domination of the Au,Pt-YSZ/YSZ interfacial contribution in the impedance of the electrochemical cell, these interceptions can be taken as good approximations of the interfacial charge transfer resistances. Accordingly, the activation energy of the charge transfer process can be calculated from the Arrhenius plot according to the following equation:

$$\frac{R^o}{R} = \exp(-\frac{E_a}{kT}) \tag{37}$$

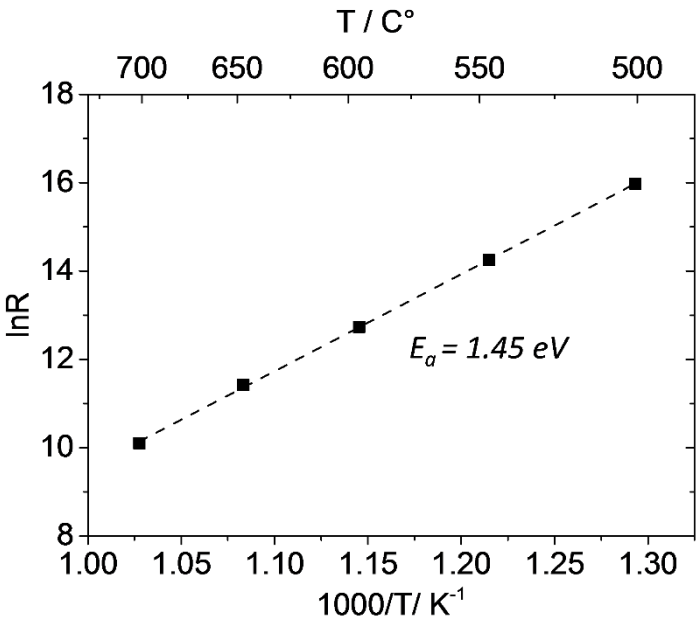

Fig. 40: *Arrhenius plot of the real axis-interceptions of the Nyquist plots measured under synthetic air conditions*

where E_a is the activation energy, k is the Boltzmann constant and T is the absolute temperature in K. The activation energy E_a is then estimated to be 1.89 eV for the charge transfer process at the Au,Pt-YSZ/YSZ interface, which is larger than that (1.45 eV) at the Pt/YSZ interface reported in [119] as expected.

Moreover, by analyzing the potential steps of the type II-sensor measured at different temperatures in Fig. 37, it is found that at 500 °C and 550 °C, the delta U is logarithmically changed with the variation of CO concentration at 20 vol.% O_2 (Fig. 41 a&b). However, this logarithmic dependence of ΔU on CO concentration is lost at temperatures not lower than 600 °C (Fig. 41 c-e, inset). By replotting these data on a linear concentration scale (Fig. 41 c-e), a clear change from the logarithmic to a linear dependence of delta U on CO concentration is disclosed. This change of the ΔU dependence on CO concentration indicates a transition from the charge transfer reaction kinetics controlled to the transport controlled mixed-potential formation at the electrode between 500 °C and 700 °C. That is to say at the lower temperatures (500 °C and 550 °C), the rate-determining step in the potential formation at the electrode is the limitation of the electrochemical reactions occurring at the TPB. However when the temperature is elevated not lower than 600 °C, this changes to the diffusion limitation of the CO transport to the TPB. The reason for this transition of the rate-determining step in the mixed potential formation can be two-fold: The increase of the temperature probably results in i) a higher consumption of CO via the gas phase reaction (reaction (3), Chap. 2) at elevated temperatures, and ii) a steeper rise of the EOC (reaction (5), Chap. 2) kinetics compared to that of the diffusion coefficient of CO ($D_{CO}(T)$) with temperature.

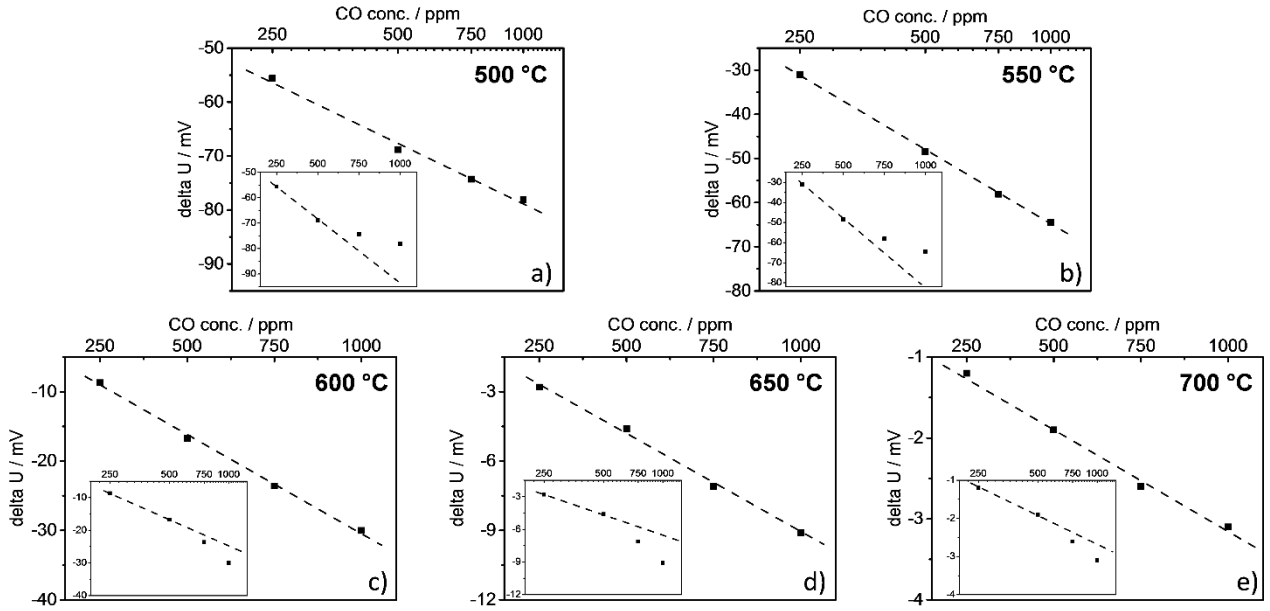

Fig. 41: *ΔU dependence of the type II-sensor on CO concentration under fixed oxygen concentration (20 vol.%) at different temperatures. A logarithmic scale is used for 500 °C and 550°C with linear scaled insets (a&b), while a linear scale is used for 600 °C, 650 °C and 700 °C with logarithmic scaled insets (c-e).*

4.5 Sensing characteristics at thermo-cyclic operation

In order to study sensing response behaviors at thermo-cyclic operation, a fresh type II-sensor was used for the first time. This type II-sensor was first characterized at different but constant working temperatures at exposure to model gases. In a second step, at the same gas conditions the temperature dependent dynamic ΔU-data were sampled, when the sensor was thermo-cyclically operated. The ΔU-measurements at thermo-cyclic operation compared to those at isothermal operation at different temperatures (Fig. 42 c&d) yielded some unexpected results: First, the ΔU-temperature profiles (ΔUTPs) for H_2 and CO are very reproducible (Fig. 42 a&b), but considerably different. They represent different potential generating electrode processes and different temperature behaviors of the contributing reaction steps involved, like gas adsorption/desorption, surface/pores diffusion and potential forming reaction kinetics.

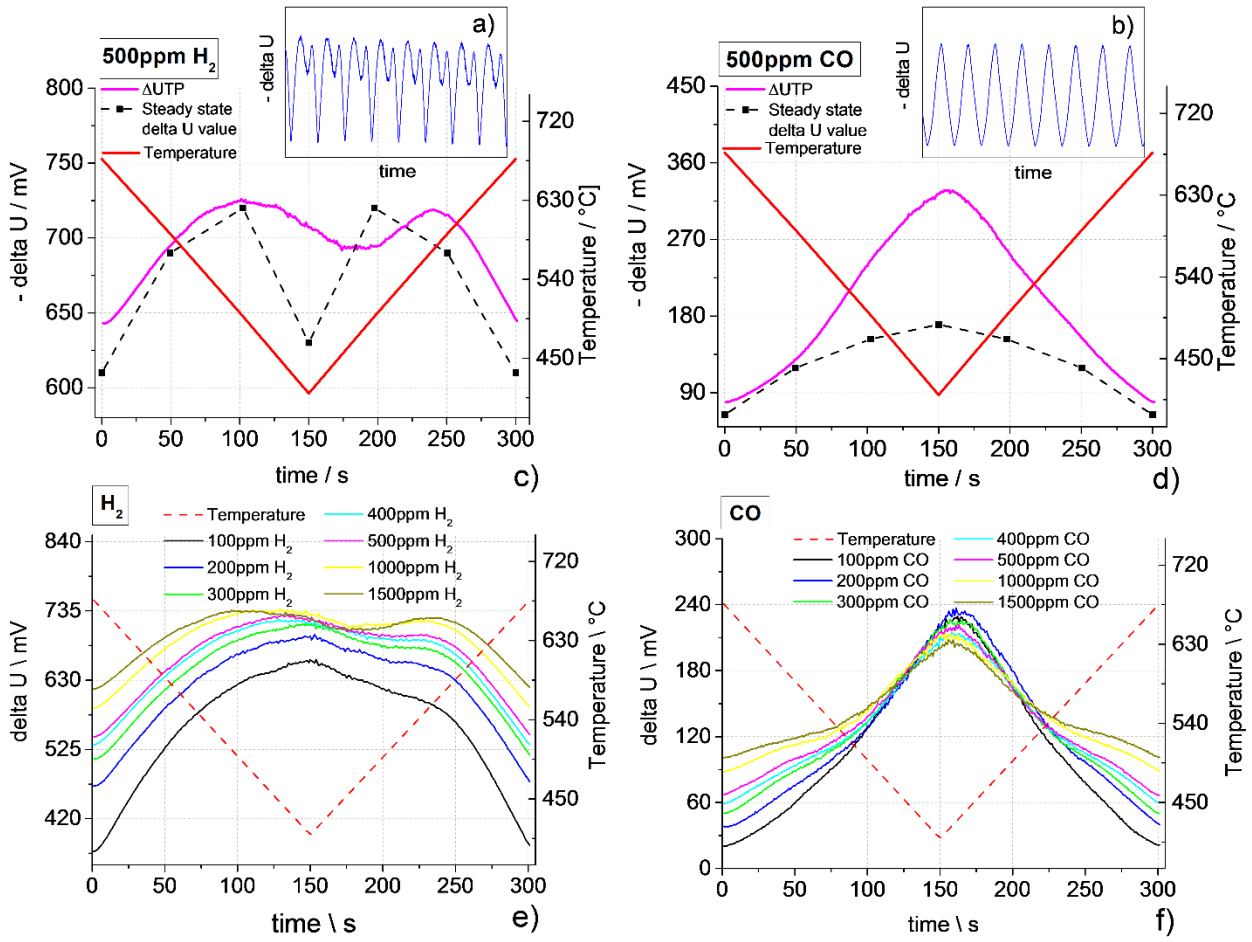

Fig. 42: *Response behavior of a type II-sensor element at thermo-cyclic operation. (a,b) Overview of ΔUTP-repeatability. (c,d) Temperature, dynamically measured delta U data in a thermo-cycle and corresponding delta U-values measured at isothermal conditions. (e) and (f) ΔUTPs representing different concentrations of H_2 and CO, respectively.*

Secondly, there is a remarkable difference between the thermo-cyclic data and the corresponding ΔU-values measured at isothermal conditions. This indicates that even at rather slow temperature rate (dT/dt = 52 K/min) the thermo-cyclic measurements seem to be far away from steady state situation. Moreover, it can be seen in Fig. 42 e&f that, the ΔUTPs show an unsymmetrical behavior in relation to

the temperature variation in the thermo-cycles. These differences between the thermo-cyclic and isothermal data (Fig. 42 c&d) and the asymmetry of the ΔUTPs relative to the thermo-cycle (Fig. 42 e&f) probably point out relatively slow mixed potential generation processes and the influence of gas diffusion effects involved in the half-cell potential formation which may be a consequence of the porous electrode morphology (Sec. 4.1.1). Surprisingly, the absolute ΔU in a temperature cycle is highest for CO (Fig. 42 f) at around the minimum temperature and for H_2 the ΔUTP shows a clear peak and a shoulder at low concentrations (100ppm and 200ppm), which develops into a second peak with increase of the concentration. However, for both gases the sensitivity (dΔUTP/dc(gas)) is highest at maximum temperature (Fig. 42 e&f).

Additional experiments were carried out to study the ΔUTP stability and reversibility, when the sensor was thermo-cyclically operated. The sensor response behaviors of the type II sensor under exposure to different concentrations of H_2, CO and C_3H_6 are shown in Fig. 43. Model gas concentrations were increased step-by-step from 0 ppm up to 2000 ppm and then decreased stepwise to 0 ppm. At H_2 and CO exposure roughly stable and reversible sensor responses at high temperatures of a thermo-cycle (lower edge of the ΔUTPs in Fig. 43 a&b) are observed, reflecting stepwise changes of gas concentrations. At low temperatures, where the potentials of a ΔUTP are high, the potential steps are not so clearly formed under H_2 exposure (Fig. 43 a), but the potential reversibility is quite good. This low temperature potential stability and reversibility is not observed in case of CO exposure, and there is a continuous potential change observed over the whole sequence of gas exposure. For comparison, potential reversibility is completely lost at all temperatures of a thermo-cycle, when the sensor is exposed to C_3H_6 (Fig. 43 c). This might be correlated with the worse stability under exposure to C_3H_6 at isothermal operation as discussed above (Fig. 29&30, Sec. 4.2.1).

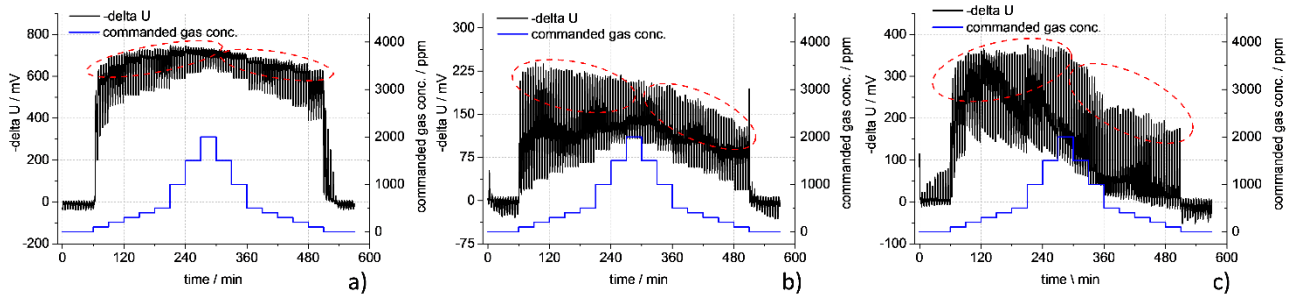

Fig. 43: *Overview of dynamic response behaviors of the type II sensor under exposure to H_2 (a), CO (b) and C_3H_6 (c) at thermo-cyclic operation, respectively. The dashed circles indicate the low-temperature behavior of the ΔUTPs*

5. SUMMARY

In recent developments of mixed potential gas sensors based on Yttrium Stabilized Zirconia (YSZ), the combination of Au/AuPt-admixtures and oxides was found to be promising electrode materials. With this material combination, satisfactory sensing characteristics were achieved, but the role of Au addition, especially its effect on the processes contributing to the mixed potential formation, has not yet been well understood. Deeper insights of the influence of Au on the electrochemical behaviors of this kind of electrodes are necessary for better understanding of the sensing behaviors and for achieving further technological improvements, as for instance, enhancement of the long-term stability.

This situation motivated studies of a layered Au,Pt-YSZ mixed potential gas sensing electrode and its dependence on the thickness of the Au-layer and the sintering conditions. In this work, for the first time three variations of this kind of electrode, which generally comprises a thick-film Pt-YSZ electrode and a thin-film Au layer deposited on top, were studied by different kinds of material analytical approaches and electrochemical methods. These studies elucidated the correlation among the electrochemical behaviors of the electrodes, the amount of gold deposition and its non-uniform distribution over the electrode. Based on these structural and electrochemical data, a qualitative model for the first time is proposed to interpret the sensing mechanism of the layered Au,Pt-YSZ electrodes. In the past such a theory was only available for the electrodes at which the Au was homogeneously admixed with the Pt-YSZ composite.

From the structural studies including the ESEM, the XRD and the Glow Discharge-Optical Emission Spectroscopy analysis (GD-OES), it was shown that the thin film Au layer at the layered Au,Pt-YSZ electrodes is not uniformly admixed with the Pt-YSZ bulk after firing, but results in a non-uniform lateral distribution on the electrode surface and a concentration gradient of Au from top over the thickness of the electrode. This Au distribution is strongly affected by the sintering temperature. The higher sintering temperature (1050 °C) results in not only a more uniform morphology of the electrode surface without a separate crystalline phase of gold , but also a better alloying of Au and Pt in the inner parts of the electrode during the sintering process, compared to the electrodes sintered at a lower temperature (850 °C). These clear structural differences of the electrodes fired at different temperatures are related to different catalytic activities over the electrode layer, and accordingly affect their open circuit potential (OCP) sensing behaviors and other electrochemical properties.

Clear correlation between the cathodic processes with oxygen and the CO sensitivity has been discovered by OCP combined with cyclic voltammetry (CV) measurements. The response to CO at 600 °C was found to be lower for the electrode with the thinner Au layer (type I) than the electrode with the thicker Au layer (type II), both sintered at 850 °C for 10min. After increasing of the sintering temperature and time, the electrode with the thicker Au layer (type III, sintered at 1050 °C for 240min) showed the highest response to CO at the same temperature. These best sensing characteristics of

the type III-electrode are assumed to be related to (i) lower gas phase reaction and better kinetics of CO electrochemical oxidation at this type of electrode and (ii) its reduced catalytic activity for the oxygen reduction reaction as confirmed by CV measurements.

Interestingly, the rate-determining step of the mixed-potential formation at the layered Au,Pt-YSZ mixed-potential electrode was found to be highly affected by i) the experimental conditions and ii) the technological parameters of fabrication. Transitions of the rate-determining step from transport control to reaction kinetics control was found by reducing the oxygen conc. from 20 to 5 vol.% or decreasing the temperature from 700 to 500 °C. These transitions were discussed in context with i) the influence of the oxygen conc. and the temperature on the electrode processes involved in the mixed potential formation, and ii) the effect of the Au layer thickness and the corresponding sintering conditions on the catalytic activities of the electrodes.

In addition, the OCP measurements on an electrode with thicker Au layer sintered at 850 °C (type II) conducted under isothermal conditions from 500 to 700 °C show that the CO sensing response is decreased by elevating the temperature. The reduction of the response at increased temperatures is probably induced by both the enhanced gas phase reaction of CO and the oxygen reduction reaction as well. These OCP results and the interpretations are well complemented and correlated with the CV and the electrochemical impedance spectroscopy (EIS) data measured in the same temperature range. The enhancement of the oxygen-involved electrochemical reaction is confirmed by both the increase of the CV currents and the reduction of the EIS impedance at the elevated temperatures

Further CV studies at 600°C showed that the current peaks in the CV profiles tended to become less pronounced by decrease of O_2 conc. with an exception of the cathodic peak at 15 vol.% O_2. By taking the interaction of the electron transfer reaction with oxygen species at the TPB with the O^{2-} transport between the TPB and the YSZ bulk into account, a possible mechanism for the CV peak formation was discussed. Surprisingly, the CV behaviors under CO exposures at a much lower scale of conc. (0 – 1000ppm, 21 vol.% O_2) were very similar to those at variation of O_2 conc. from 5 to 21 vol.%. However, the dependence of the current peaks on CO conc. is opposite to that on O_2 conc. These observations motivate the assumption that with and without the CO exposures, the same types of processes dominate the formation of the current peaks of the CV profiles

From the EIS behaviors (600 °C) at different O_2 conc., it was found that all the measured Nyquist plots showed two semi-circular arcs. The semi-circular arcs in the high frequency regime were smaller than the ones in the low frequency regime, and almost not influenced by the variation of O_2 conc. In good agreement with literature, they are assumed to be related to the O^{2-} transport in the solid electrolyte. By decreasing the O_2 conc., the radiuses of semicircular arcs in the low frequency regime were clearly increased. These arcs are presumed to be attributed to the electron transfer reactions with oxygen species at the TPB. The further analysis of the EIS data indicates that the electrode processes may include a four-electron transfer step with associatively adsorbed oxygen species.

At thermo-cyclic operation, the ΔU measurements revealed gas specific ΔU-temperature-profiles (ΔUTP). The ΔUTP stability and reversibility depend on operation temperature and are specific characteristics of the individual gas component. The data disclosed clearly, that the well accepted model of mixed potential formation, which is valid at constant temperature, cannot explain the behaviors of the thermo-cycled cell. Obviously, the non-steady state processes probably including rather low reaction rates, diffusion processes and perhaps catalytic conversion of the gas molecules within the electrode layer have to be taken into consideration for interpretation of the data under thermo-cyclic conditions. Such a theory is still missing up to now.

With respect to selectivity and stability of the sensors, the highest sensing response was observed in the H_2 containing gases compared to the other gas species like CO, CH_4, and C_3H_6 for both the type II (low temperature sintered) and the type III (high temperature sintered) sensors. However, clear response and potential stability losses were observed at exposure to C_3H_6. Formation of coking layers on the electrode seems to be correlated with this response decrease.

Surprisingly, the response degradation was even observed by aging the sensors at 600 °C in ambient air. Combined OCP, CV and EIS studies revealed that, the aging process results in some minor irreversible but mainly reversible changes at the electrode/electrolyte interface. Both induce the response degradation which is well correlated with an impedance increase and a CV current decrease. The reversible changes are assumed to be attributed to the formation of an oxidation phase of the metallic parts at the TPB, which is well described in literature. Now, for the first time in this work it could be demonstrated that this reversible response degradation can be nearly fully recovered by the application of cathodic polarization sequences.

Consequently, due to the strong correlation between the OCP response to CO and the dynamic electrochemical behaviors ((EIS and CV)) at ambient air, both the EIS and the CV method can be used as efficient tools to check the sensitivity of the sensor at ambient air conditions. In case of OCP response degradation, the sensitivity can be almost fully regenerated by application of cathodic polarization at enhanced temperatures (T≥700°C). This combination of OCP measurements with dynamic electrochemical methods and the application of cathodic polarization procedures is of enormous practical relevance and was filed for a patent. It excited high interest of the sensor chip producer (Lamtec Meß- und Regeltechnik für Feuerungen GmbH, Walldorf) because it allows sensitivity estimation and regeneration of layered Au,Pt-YSZ gas sensing electrodes whenever ambient air conditions are given. For instance, in case of long-term CO/HC-monitoring for improvement of automated combustion process control of firing appliances, this procedure could be carried out in breaks between firing batches without the need of de-installation of the sensor and, indeed, without any exposure to model gases.

REFERENCE

[1] P.K. Sekhar, E.L. Brosha, R. Mukundan, W. Li, M.A. Nelson, P. Palanisamy, F.H. Garzon, Application of commercial automotive sensor manufacturing methods for NOx/NH3 mixed potential sensors for on-board emissions control, Sens Actuators B Chem. 144 (2010) 112-119.
[2] P. Butschbach, F. Hammer, H. Kohler, A. Potreck, T. Trautmann, Extensive reduction of toxic gas emissions of firewood-fueled low power fireplaces by improved in situ gas sensorics and catalytic treatment of exhaust gas, Sens Actuators B Chem. 137 (2009) 32-41.
[3] E.L. Brosha, R. Mukundan, R. Lujan, F.H. Garzon, Mixed potential NOx sensors using thin film electrodes and electrolytes for stationary reciprocating engine type applications, Sens Actuators B Chem. 119 (2006) 398-408.
[4] J. Riegel, H. Neumann, H.M. Wiedenmann, Exhaust gas sensors for automotive emission control, Solid State Ionics. 152–153 (2002) 783-800.
[5] E.L. Brosha, R. Mukundan, D.R. Brown, F.H. Garzon, J.H. Visser, Development of ceramic mixed potential sensors for automotive applications, Solid State Ionics. 148 (2002) 61-69.
[6] M. Fleischer, M. Lehmann, Solid State Gas Sensors-Industrial Application, Springer Science & Business Media, 2012.
[7] S. Zhuiykov, N. Miura, Development of zirconia-based potentiometric NOx sensors for automotive and energy industries in the early 21st century: What are the prospects for sensors?, Sens Actuators B Chem. 121 (2007) 639-651.
[8] N. Yamazoe, Toward innovations of gas sensor technology, Sens Actuators B Chem. 108 (2005) 2-14.
[9] R. Moos, A brief overview on automotive exhaust gas sensors based on electroceramics, International Journal of Applied Ceramic Technology. 2 (2005) 401-413.
[10] S. Capone, A. Forleo, L. Francioso, R. Rella, P. Siciliano, J. Spadavecchia, D. Presicce, A. Taurino, Solid state gas sensors: state of the art and future activities, Journal of Optoelectronics and Advanced Materials. 5 (2003) 1335-1348.
[11] U. Guth, W. Vonau, J. Zosel, Recent developments in electrochemical sensor application and technology—a review, Measurement Science and Technology. 20 (2009) 042002.
[12] C. Park, J. Fergus, N. Miura, J. Park, A. Choi, Solid-state electrochemical gas sensors, Ionics. 15 (2009) 261-284.
[13] K. Rajeshwar, J.G. Ibanez, Environmental electrochemistry: Fundamentals and applications in pollution sensors and abatement, Academic Press, 1997.
[14] E. Comini, G. Faglia, G. Sberveglieri, Solid state gas sensing, Springer Science & Business Media, 2008.
[15] M.J. Madou, S.R. Morrison, Chemical sensing with solid state devices, Elsevier, 2012.
[16] A.J. Bard, G. Inzelt, F. Scholz, Electrochemical dictionary, Springer Science & Business Media, 2008.
[17] P.T. Moseley, Solid state gas sensors, Taylor & Francis, 1987.
[18] S. Zhuiykov, Electrochemistry of zirconia gas sensors, CRC Press, 2007.
[19] R. Moos, K. Sahner, M. Fleischer, U. Guth, N. Barsan, U. Weimar, Solid state gas sensor research in Germany–a status report, Sensors. 9 (2009) 4323-4365.
[20] N. Miura, T. Sato, S. Anggraini, H. Ikeda, S. Zhuiykov, A review of mixed-potential type zirconia-based gas sensors, Ionics. 20 (2014) 901-925.
[21] N. Miura, G. Lu, N. Yamazoe, Progress in mixed-potential type devices based on solid electrolyte for sensing redox gases, Solid State Ionics. 136–137 (2000) 533-542.
[22] F.H. Garzon, R. Mukundan, E.L. Brosha, Solid-state mixed potential gas sensors: theory, experiments and challenges, Solid State Ionics. 136–137 (2000) 633-638.
[23] Y. Liu, J. Parisi, X. Sun, Y. Lei, Solid-state gas sensors for high temperature applications–a review, Journal of Materials Chemistry A. 2 (2014) 9919-9943.
[24] P. Moseley, BC Tofield Solid State Gas Sensors, Adam Hilger, Bristol. (1987) 17-31.
[25] A. Vogel, G. Baier, V. Schüle, Non-Nernstian potentiometric zirconia sensors: screening of potential working electrode materials, Sens Actuators B Chem. 15 (1993) 147-150.
[26] M. Breedon, N. Miura, Augmenting H2 sensing performance of YSZ-based electrochemical gas sensors via the application of Au mesh and YSZ coating, Sens Actuators B Chem. 182 (2013) 40-44.

[27] X. Zhang, H. Kohler, M. Schwotzer, U. Guth, Mixed-potential gas sensor with PtAu-8YSZ sensing electrode: Electric potential difference measurements at isothermal and thermo-cyclic operation, Sens Actuators B Chem. 217 (2015) 107-112.
[28] J. Zosel, K. Ahlborn, R. Müller, D. Westphal, V. Vashook, U. Guth, Selectivity of HC-sensitive electrode materials for mixed potential gas sensors, Solid State Ionics. 169 (2004) 115-119.
[29] J. Zosel, R. Müller, V. Vashook, U. Guth, Response behavior of perovskites and Au/oxide composites as HC-electrodes in different combustibles, Solid State Ionics. 175 (2004) 531-533.
[30] J. Zosel, G. Schiffel, F. Gerlach, K. Ahlborn, U. Sasum, V. Vashook, U. Guth, Electrode materials for potentiometric hydrogen sensors, Solid State Ionics. 177 (2006) 2301-2304.
[31] J. Zosel, D. Westphal, S. Jakobs, R. Müller, U. Guth, Au–oxide composites as HC-sensitive electrode material for mixed potential gas sensors, Solid State Ionics. 152–153 (2002) 525-529.
[32] L. Chevallier, E. Di Bartolomeo, M.L. Grilli, M. Mainas, B.M. White, E.D. Wachsman, E. Traversa, Non-nernstian planar sensors based on YSZ with an Nb2O5 electrode: discussion on sensing mechanism, ECS Transactions. 1 (2006) 163-171.
[33] E. Bartolomeo, M.L. Grilli, J.W. Yoon, E. Traversa, Zirconia - Based Electrochemical NOx Sensors with Semiconducting Oxide Electrodes, Journal of the American Ceramic Society. 87 (2004) 1883-1889.
[34] N.F. Szabo, P.K. Dutta, Correlation of sensing behavior of mixed potential sensors with chemical and electrochemical properties of electrodes, Solid State Ionics. 171 (2004) 183-190.
[35] N. Miura, G. Lu, N. Yamazoe, High-temperature potentiometric/amperometric NO x sensors combining stabilized zirconia with mixed-metal oxide electrode, Sens Actuators B Chem. 52 (1998) 169-178.
[36] N. Miura, S. Zhuiykov, T. Ono, M. Hasei, N. Yamazoe, Mixed potential type sensor using stabilized zirconia and ZnFe 2 O 4 sensing electrode for NO x detection at high temperature, Sens Actuators B Chem. 83 (2002) 222-229.
[37] J. Park, B. Yoon, C.O. Park, W.-J. Lee, C.B. Lee, Sensing behavior and mechanism of mixed potential NO x sensors using NiO, NiO (+ YSZ) and CuO oxide electrodes, Sens Actuators B Chem. 135 (2009) 516-523.
[38] N. Miura, T. Raisen, G. Lu, N. Yamazoe, Highly selective CO sensor using stabilized zirconia and a couple of oxide electrodes, Sens Actuators B Chem. 47 (1998) 84-91.
[39] N. Miura, G. Lu, N. Yamazoe, H. Kurosawa, M. Hasei, Mixed potential type NO x sensor based on stabilized zirconia and oxide electrode, Journal of the Electrochemical Society. 143 (1996) L33-L35.
[40] N. Li, T. Tan, H. Zeng, High - Temperature Carbon Monoxide Potentiometric Sensor, Journal of the Electrochemical Society. 140 (1993) 1068-1073.
[41] D. Narducci, A. Ornaghi, C.M. Mari, CO determination in air by YSZ-based sensors, Sens Actuators B Chem. 19 (1994) 566-568.
[42] E.L. Brosha, R. Mukundan, D.R. Brown, F.H. Garzon, J. Visser, M. Zanini, Z. Zhou, E. Logothetis, CO/HC sensors based on thin films of LaCoO 3 and La 0.8 Sr 0.2 CoO $3-\delta$ metal oxides, Sens Actuators B Chem. 69 (2000) 171-182.
[43] R.-J. Wu, C.-H. Hu, C.-T. Yeh, P.-G. Su, Nanogold on powdered cobalt oxide for carbon monoxide sensor, Sens Actuators B Chem. 96 (2003) 596-601.
[44] T. Striker, V. Ramaswamy, E.N. Armstrong, P.D. Willson, E.D. Wachsman, J.A. Ruud, Effect of nanocomposite Au–YSZ electrodes on potentiometric sensor response to NO x and CO, Sens Actuators B Chem. 181 (2013) 312-318.
[45] A. Morata, J.-P. Viricelle, A. Tarancon, G. Dezanneau, C. Pijolat, F. Peiro, J. Morante, Development and characterisation of a screen-printed mixed potential gas sensor, Sens Actuators B Chem. 130 (2008) 561-566.
[46] Y. Fujio, V.V. Plashnitsa, M. Breedon, N. Miura, Construction of sensitive and selective zirconia-based CO sensors Using ZnCr2O4-based sensing electrodes, Langmuir. 28 (2011) 1638-1645.
[47] F. Sun, X. Li, L. Liu, J. Wang, Novel Zn–M–O (M= Sn, Co) sensing electrodes for selective mixed potential CO/C 3 H 8 sensors, Sens Actuators B Chem. 184 (2013) 220-227.
[48] S.A. Anggraini, V.V. Plashnitsa, P. Elumalai, M. Breedon, N. Miura, Stabilized zirconia-based planar sensor using coupled oxide (+ Au) electrodes for highly selective CO detection, Sens Actuators B Chem. 160 (2011) 1273-1281.

[49] J.Y. Park, S.J. Song, E.D. Wachsman, Highly Sensitive/Selective Miniature Potentiometric Carbon Monoxide Gas Sensors with Titania - Based Sensing Elements, Journal of the American Ceramic Society. 93 (2010) 1062-1068.
[50] M.D. Argyle, C.H. Bartholomew, Heterogeneous catalyst deactivation and regeneration: A review, Catalysts. 5 (2015) 145-269.
[51] G. Lu, N. Miura, N. Yamazoe, High-temperature hydrogen sensor based on stabilized zirconia and a metal oxide electrode, Sens Actuators B Chem. 35 (1996) 130-135.
[52] X. Zhang, H. Kohler, M. Schwotzer, Y.H. Wu, U. Guth, Mixed-potential gas sensor with layered Au,Pt-YSZ electrode: Investigating the sensing mechanism with steady state and dynamic electrochemical methods, Sens Actuators B Chem. 252 (2017) 554-560.
[53] T. Ueda, H. Abe, K. Kamada, S.R. Bishop, H.L. Tuller, T. Hyodo, Y. Shimizu, Enhanced sensing response of solid-electrolyte gas sensors to toluene: Role of composite Au/metal oxide sensing electrode, Sens Actuators B Chem. 252 (2017) 268-276.
[54] I. Romanytsia, J.-P. Viricelle, P. Vernoux, C. Pijolat, Application of advanced morphology Au–X (X = YSZ, ZrO2) composites as sensing electrode for solid state mixed-potential exhaust NOx sensor, Sens Actuators B Chem. 207, Part A (2015) 391-397.
[55] J. Zosel, M. Schelter, W. Oelßner, C. Vonau, U. Enseleit, U. Guth, M. Mertig, V. Voshook, D. Tuchtenhagen, K. Wienand, Recent developments in materials for potentiometric sensors, Proceedings IMCS 2012. (2012) 569-572.
[56] A. Hetznecker, H. Kohler, U. Guth, Enhanced studies on the mechanism of gas selectivity and electronic interactions of SnO2/Na+-ionic conductors, Sens Actuators B Chem. 120 (2007) 378-385.
[57] M. Haruta, When gold is not noble: catalysis by nanoparticles, The chemical record. 3 (2003) 75-87.
[58] T. Takei, T. Akita, I. Nakamura, T. Fujitani, M. Okumura, K. Okazaki, J. Huang, T. Ishida, M. Haruta, C. Bruce, Heterogeneous catalysis by gold, Advances in Catalysis, Academic Press. (2013) 1.
[59] M. Haruta, M. Daté, Advances in the catalysis of Au nanoparticles, Applied Catalysis A: General. 222 (2001) 427-437.
[60] L.Y. Woo, L.P. Martin, R.S. Glass, W. Wang, S. Jung, R.J. Gorte, E.P. Murray, R.F. Novak, J.H. Visser, Effect of electrode composition and microstructure on impedancemetric nitric oxide sensors based on YSZ electrolyte, Journal of the Electrochemical Society. 155 (2008) J32-J40.
[61] H. Popke, E. Mutoro, B. Luerssen, J. Janek, Oxidation of Platinum in the Epitaxial Model System Pt (111)/YSZ (111): Quantitative Analysis of an Electrochemically Driven PtO x Formation, The Journal of Physical Chemistry C. 116 (2012) 1912-1920.
[62] A.K. Opitz, M.P. Hörlein, T. Huber, J. Fleig, Current-voltage characteristics of platinum model electrodes on yttria-stabilized zirconia, Journal of The Electrochemical Society. 159 (2012) B502-B513.
[63] T. Ryll, H. Galinski, L. Schlagenhauf, P. Elser, J.L. Rupp, A. Bieberle - Hutter, L.J. Gauckler, Microscopic and Nanoscopic Three - Phase - Boundaries of Platinum Thin - Film Electrodes on YSZ Electrolyte, Advanced Functional Materials. 21 (2011) 565-572.
[64] H. Pöpke, E. Mutoro, C. Raiß, B. Luerßen, M. Amati, M.K. Abyaneh, L. Gregoratti, J. Janek, The role of platinum oxide in the electrode system Pt(O2)/yttria-stabilized zirconia, Electrochimica Acta. 56 (2011) 10668-10675.
[65] H. Pöpke, E. Mutoro, B. Luerßen, J. Janek, The potential of in situ-scanning electron microscopy — Morphology changes of electrically polarized thin film Pt(O2)/YSZ model electrodes, Solid State Ionics. 189 (2011) 56-62.
[66] A.K. Opitz, A. Lutz, M. Kubicek, F. Kubel, H. Hutter, J. Fleig, Investigation of the oxygen exchange mechanism on Pt|yttria stabilized zirconia at intermediate temperatures: Surface path versus bulk path, Electrochimica Acta. 56 (2011) 9727-9740.
[67] A. Kumar, F. Ciucci, A.N. Morozovska, S.V. Kalinin, S. Jesse, Measuring oxygen reduction/evolution reactions on the nanoscale, Nature chemistry. 3 (2011) 707.
[68] G. Beck, H. Pöpke, B. Luerßen, J. Janek, Microstructure of platinum films on YSZ prepared by pulsed laser deposition, Journal of Crystal Growth. 322 (2011) 95-102.
[69] A.K. Opitz, A. Schintlmeister, H. Hutter, J. Fleig, Visualization of oxygen reduction sites at Pt electrodes on YSZ by means of 18O tracer incorporation: The width of the electrochemically active zone, Physical Chemistry Chemical Physics. 12 (2010) 12734-12745.

[70] A.K. Opitz, J. Fleig, Investigation of O2 reduction on Pt/YSZ by means of thin film microelectrodes: The geometry dependence of the electrode impedance, Solid State Ionics. 181 (2010) 684-693.
[71] E. Mutoro, N. Baumann, J.r. Janek, Janus-faced SiO2: Activation and passivation in the electrode system platinum/yttria-stabilized zirconia, The Journal of Physical Chemistry Letters. 1 (2010) 2322-2326.
[72] N. Baumann, E. Mutoro, J. Janek, Porous model type electrodes by induced dewetting of thin Pt films on YSZ substrates, Solid State Ionics. 181 (2010) 7-15.
[73] E. Mutoro, B. Luerßen, S. Günther, J. Janek, The electrode model system Pt(O2)|YSZ: Influence of impurities and electrode morphology on cyclic voltammograms, Solid State Ionics. 180 (2009) 1019-1033.
[74] J.L. Hertz, A. Rothschild, H.L. Tuller, Highly enhanced electrochemical performance of silicon-free platinum–yttria stabilized zirconia interfaces, Journal of Electroceramics. 22 (2009) 428-435.
[75] G. Fóti, A. Jaccoud, C. Falgairette, C. Comninellis, Charge storage at the Pt/YSZ interface, Journal of electroceramics. 23 (2009) 175.
[76] C. Falgairette, G. Fóti, Oxygen storage in O2/Pt/YSZ cell, Catalysis Today. 146 (2009) 274-278.
[77] E. Mutoro, S. Günther, B. Luerßen, I. Valov, J. Janek, Electrode activation and degradation: Morphology changes of platinum electrodes on YSZ during electrochemical polarisation, Solid State Ionics. 179 (2008) 1835-1848.
[78] S. Koc, G.J. La O, T. Golfinopoulos, Y. Shao-Horn, Impedance Spectroscopy Studies of Oxygen Reduction Reaction on Thin Film Platinum Microelectrodes Supported on YSZ, ECS Transactions. 7 (2007) 1271-1277.
[79] J. Janek, B. Luerßen, E. Mutoro, H. Fischer, S. Günther, In situ imaging of electrode processes on solid electrolytes by photoelectron microscopy and microspectroscopy–the role of the three-phase boundary, Topics in Catalysis. 44 (2007) 399-407.
[80] R. Radhakrishnan, A.V. Virkar, S.C. Singhal, Estimation of charge-transfer resistivity of Pt cathode on YSZ electrolyte using patterned electrodes, Journal of The Electrochemical Society. 152 (2005) A927-A936.
[81] N. Kotsionopoulos, S. Bebelis, Electrochemical promotion of the oxidation of propane on Pt/YSZ and Rh/YSZ catalyst-electrodes, Journal of applied electrochemistry. 35 (2005) 1253-1264.
[82] S.B. Adler, Factors governing oxygen reduction in solid oxide fuel cell cathodes, Chemical reviews. 104 (2004) 4791-4844.
[83] N.Q. Minh, Ceramic fuel cells, Journal of the American Ceramic Society. 76 (1993) 563-588.
[84] C. Vayenas, S. Bebelis, I. Yentekakis, P. Tsiakaras, H. Karasali, Non-faradaic electrochemical modification of catalytic activity, Platinum Metals Review. 34 (1990) 122-130.
[85] C. Vayenas, S. Bebelis, S. Ladas, Dependence of catalytic rates on catalyst work function, Nature. 343 (1990) 625-627.
[86] A. Mitterdorfer, L. Gauckler, Identification of the reaction mechanism of the Pt, O2 (g)| yttria-stabilized zirconia system: Part II: Model implementation, parameter estimation, and validation, Solid State Ionics. 117 (1999) 203-217.
[87] A. Mitterdorfer, L. Gauckler, Identification of the reaction mechanism of the Pt, O2 (g)| yttria-stabilized zirconia system: Part I: General framework, modelling, and structural investigation, Solid State Ionics. 117 (1999) 187-202.
[88] H. Pöpke, E. Mutoro, B. Luerßen, J. Janek, Oxygen reduction and oxidation at epitaxial model-type Pt(O2)/YSZ electrodes – On the role of PtOx formation on activation, passivation, and charge transfer, Catalysis Today. 202 (2013) 12-19.
[89] M.P. Hörlein, A.K. Opitz, J. Fleig, On the variability of oxygen exchange kinetics of platinum model electrodes on yttria stabilized zirconia, Solid State Ionics. 247 (2013) 56-65.
[90] S. Sridhar, V. Stancovski, U.B. Pal, Effect of oxygen-containing species on the impedance of the Pt/YSZ interface, Solid State Ionics. 100 (1997) 17-22.
[91] M. Mori, H. Nishimura, Y. Itagaki, Y. Sadaoka, E. Traversa, Detection of sub-ppm level of VOCs based on a Pt/YSZ/Pt potentiometric oxygen sensor with reference air, Sens Actuators B Chem. 143 (2009) 56-61.
[92] L. Chevallier, E. Di Bartolomeo, M.L. Grilli, E. Traversa, High temperature detection of CO/HCs gases by non-Nernstian planar sensors using Nb2O5 electrode, Sens Actuators B Chem. 130 (2008) 514-519.

[93] E.L. Brosha, R. Mukundan, D.R. Brown, F.H. Garzon, Mixed potential sensors using lanthanum manganate and terbium yttrium zirconium oxide electrodes, Sensors and Actuators B: Chemical. 87 (2002) 47-57.
[94] J. Zosel, D. Franke, K. Ahlborn, F. Gerlach, V. Vashook, U. Guth, Perovskite related electrode materials with enhanced NO sensitivity for mixed potential sensors, Solid State Ionics. 179 (2008) 1628-1631.
[95] N. Miura, J. Wang, M. Nakatou, P. Elumalai, S. Zhuiykov, M. Hasei, High-temperature operating characteristics of mixed-potential-type NO2 sensor based on stabilized-zirconia tube and NiO sensing electrode, Sensors and Actuators B: Chemical. 114 (2006) 903-909.
[96] S. Zhuiykov, T. Ono, N. Yamazoe, N. Miura, High-temperature NOx sensors using zirconia solid electrolyte and zinc-family oxide sensing electrode, Solid State Ionics. 152–153 (2002) 801-807.
[97] K. Frank, H. Kohler, U. Guth, Influence of the measurement conditions on the sensitivity of SnO2 gas sensors operated thermo-cyclically, Sensors and Actuators B: Chemical. 141 (2009) 361-369.
[98] K. Frank, V. Magapu, V. Schindler, H. Kohler, H.B. Keller, R. Seifert, Chemical Analysis with Tin Oxide Gas Sensors: Choice of Additives, Method of Operation and Analysis of Numerical Signal, Sensor Letters. 6 (2008) 908-911.
[99] H. Kohler, J. Röber, N. Link, I. Bouzid, New applications of tin oxide gas sensors: I. Molecular identification by cyclic variation of the working temperature and numerical analysis of the signals, Sensors and Actuators B: Chemical. 61 (1999) 163-169.
[100] R. Seifert, H.B. Keller, K. Frank, H. Kohler, ProSens—An Efficient Mathematical Procedure for Calibration and Evaluation of Tin Oxide Gas Sensor Data, Sensor Letters. 9 (2011) 7-10.
[101] A.D. McNaught, A.D. McNaught, Compendium of chemical terminology, Blackwell Science Oxford, 1997.
[102] K. Cammann, Working with ion-selective electrodes: chemical laboratory practice, Springer Science & Business Media, 2012.
[103] W.J. Fleming, Physical principles governing nonideal behavior of the zirconia oxygen sensor, Journal of the Electrochemical Society. 124 (1977) 21-28.
[104] P. Atkins, J. De Paula, J. Keeler, Atkins' physical chemistry, Oxford university press, 2018.
[105] T.B. Massalski, H. Okamoto, P. Subramanian, L. Kacprzak, Binary alloy phase diagrams. vol. 3, ASM International, 1990. (1990) 1485.
[106] T. Ono, M. Hasei, A. Kunimoto, N. Miura, Improvement of sensing performances of zirconia-based total NOx sensor by attachment of oxidation-catalyst electrode, Solid State Ionics. 175 (2004) 503-506.
[107] G. Ertl, H. Knözinger, J. Weitkamp, Handbook of heterogeneous catalysis. (1997).
[108] L. Chevallier, E. Di Bartolomeo, M.L. Grilli, M. Mainas, B. White, E.D. Wachsman, E. Traversa, Non-Nernstian planar sensors based on YSZ with a Nb2O5 electrode, Sens Actuators B Chem. 129 (2008) 591-598.
[109] A.J. Bard, L.R. Faulkner, J. Leddy, C.G. Zoski, Electrochemical methods: fundamentals and applications, wiley New York, 1980.
[110] D.A. Brownson, C.E. Banks, The handbook of graphene electrochemistry, Springer, 2014.
[111] C. Vayenas, S. Ladas, S. Bebelis, I. Yentekakis, S. Neophytides, J. Yi, C. Karavasilis, C. Pliangos, Electrochemical promotion in catalysis: non-faradaic electrochemical modification of catalytic activity, Electrochimica Acta. 39 (1994) 1849-1855.
[112] J. Yi, A. Kaloyannis, C.G. Vayenas, High temperature cyclic voltammetry of Pt catalyst-electrodes in solid electrolyte cells, Electrochimica Acta. 38 (1993) 2533-2539.
[113] J.R. Macdonald, W.R. Kenan, Impedance Spectroscopy: Emphasizing Solid Materials and Systems, Wiley, 1987.
[114] H. Okamoto, G. Kawamura, T. Kudo, Study of oxygen adsorption on platinum through observation of exchange current in a solid electrolyte concentration cell, Electrochimica Acta. 28 (1983) 379-382.
[115] W.-F. Zhang, P. Schmidt-Zhang, U. Guth, Electrochemical studies on cells M/YSZ/Pt (M= Pt, Pt–Ga2O3) in NO, O2, N2 gas mixtures, Solid State Ionics. 169 (2004) 121-128.
[116] J.E. Huheey, E.A. Keiter, R.L. Keiter, O.K. Medhi, Inorganic chemistry: principles of structure and reactivity, Pearson Education India, 2006.
[117] C.H. Bartholomew, Mechanisms of catalyst deactivation, Applied Catalysis A: General. 212 (2001) 17-60.

[118] L.Y. Woo, L.P. Martin, R.S. Glass, R.J. Gorte, Impedance Characterization of a Model Au / Yttria-Stabilized Zirconia / Au Electrochemical Cell in Varying Oxygen and NO x Concentrations, Journal of the Electrochemical Society. 154 (2007) J129-J135.
[119] S. Badwal, H. De Bruin, Electrode Kinetics at the Pt/Yttria - Stabilized Zirconia Interface by Complex Impedance Dispersion Analysis, physica status solidi (a). 54 (1979) 261-270.

LIST OF APPENDIX

APPENDIX

Appendix 1: Working principle of Glow Discharge Optical Spectrometry

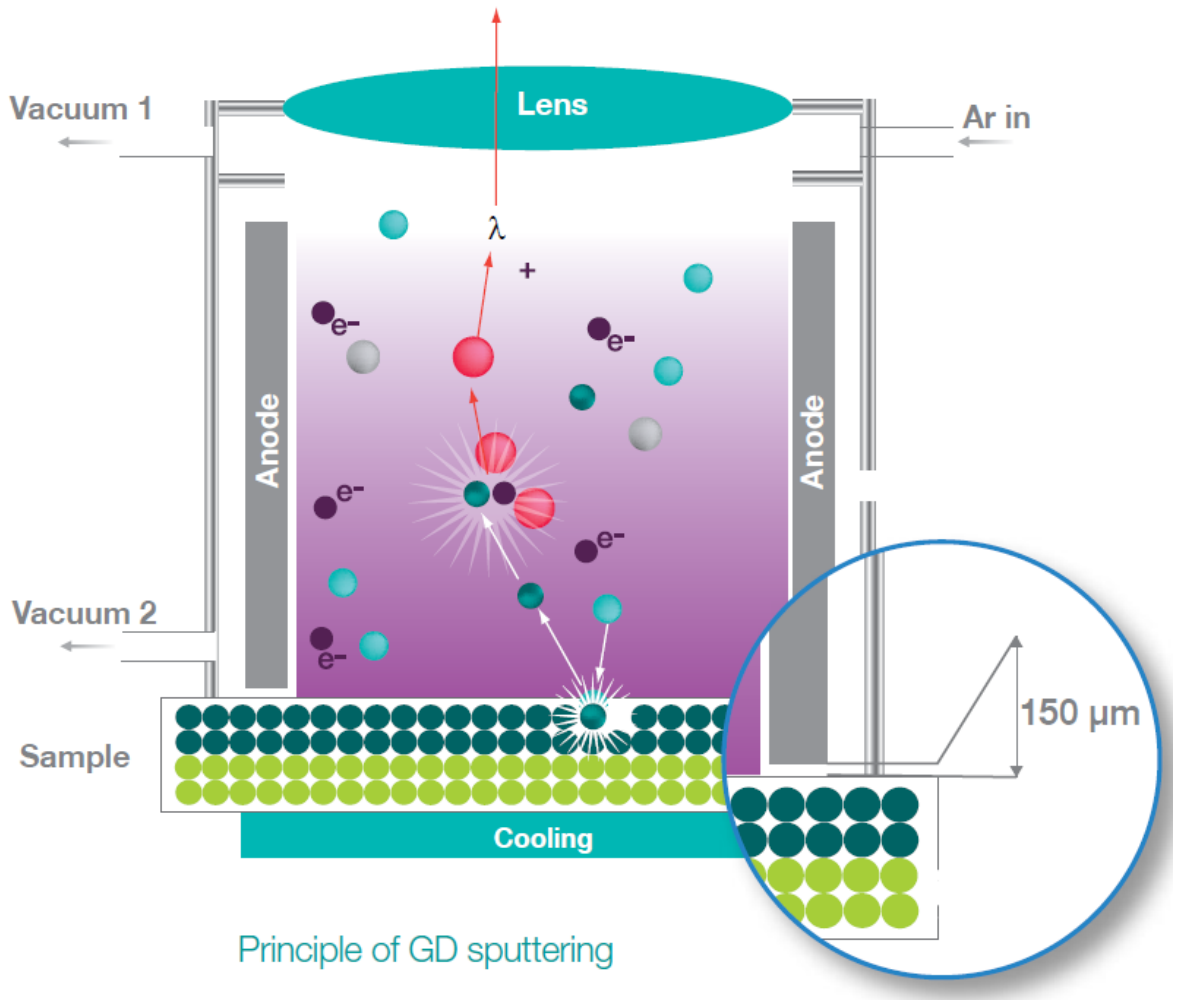

Schematic illustration of working principle of Glow Discharge Optical Spectrometry (reproduced from User manual of GD-OES, HORIBA Scientific)

Principle:

Glow Discharge Optical Spectrometry is based on sputtering technique and used to perform chemical analysis and quantitative depth profile of thin and thick films. In a GD-OES analysis, a sample is placed on a copper electrode (cathode). The discharge is applied between the anode and the cathode, which triggers off the sample surface erosion. Atoms ejected are then excited by an Argon plasma. The excited atoms finally come back to their fundamental energy level, and emit characteristic photons. The emitted photons, whose energy are dependent on characteristics of the energy level of the chemical elements in the sample, are then detected by optical sensors. As a consequence of these processes, a quantification of the elemental composition of the sample with in-depth information can be achieved.

Appendix 2: Technical specification of PalmSens3 system

System specifications

Controlled potential mode (potentiostat)	
▪ dc-potential range	± 5.000 V
▪ compliance voltage	± 8.0 V
▪ dc-potential resolution	0.15 mV
▪ applied potential accuracy	≤ 0.2 % with max. 2 mV offset error
▪ current ranges	100 pA to 10 mA (9 ranges)
▪ maximum measured current	± 30 mA (typical)
▪ current resolution	0.01 % of current range
▪ accuracy	≤ 5 % at 100 pA ≤ 1 % of current range at 1 nA ≤ 0.5 % at 10 nA ≤ 0.2 % at 100 nA to 1 mA ≤ 0.5 % at 10 mA all with max. 0.2 % offset error
▪ max. acquisition rate	200 000 data points/s
Controlled current mode (galvanostat)	
▪ current ranges	1 µA to 10 mA
▪ dc-current range	± 3.000 times selected current range
▪ dc-current resolution	0.01 % of selected current range
▪ max. dc-offset error	≤ 0.2 %
▪ current accuracy (deviation)	≤ 0.4 %
▪ maximum output voltage	± 8 V
Impedance measurements	
▪ frequency range	100 µHz to 50 kHz
▪ ac- amplitude range	1 mV to 0.3 V (rms)
General	
▪ electrometer amplifier input	> 100 Gohm // 4 pF
▪ rise time	programmable from min. 0.5 µs
Other	
▪ keypad	run, skip, abort, backlight and power
▪ housing	aluminium: 155 mm x 85 mm x 35 mm
▪ weight	430 g
▪ temperature range	0° C to + 40° C
▪ power supply	USB or internal Li-ion battery
▪ battery time	>10 hours idle time >9 hours idle time with Bluetooth extension
▪ communication	USB, RS232 or TTL (via auxiliary port)
Auxiliary port (D-Sub 15)	
▪ analog input	0-3 V, 12 bit
▪ analog output	0-3 V, 16 bit
▪ 4 digital outputs and 1 digital input	0-3.3 V
▪ I-out and E-out	raw output of current and potential
▪ serial comms	Rx / Tx (RS232 or TTL)
▪ power	5 V output (max. 50 mA)

Appendix 3: Technical specification of PalmSens3 system

System specifications

	MultiEmStat3
- compliance voltage	± 5 V
- dc-potential range	± 3.000 V
- applied dc-potential resolution	0.1 mV
- applied dc-potential accuracy	≤ 0.2 % with max 2 mV offset
- current ranges	1 nA to 10 mA (8 ranges)
- maximum measured current	± 20 mA typical and ± 15 mA minimum

Current is measured using a ZRA (zero resistance ammeter)

- current resolution	0.1 % of current range 1 pA on lowest current range
- accuracy	≤ 0.5 % of current range at 10 nA and ≤ 1 % at 1 nA ≤ 0.2 % at 100 nA to 100 uA ≤ 0.5 % at 1 mA, 10 mA and 100 mA all with additional 0.2 % offset error
- electrometer amplifier input	> 100 Gohm // 4 pF
- rise time	approx. 100 µs

Housing for MultiEmStat3 - 4 channel:

- material:	aluminum
- dimensions:	115 mm x 85 mm x 35 mm
- weight:	+/- 260 g
- power:	5V external adapter

Housing for 8 and 12 channels:

- material:	aluminum
- dimensions:	120 mm x 210 mm x 75 mm
- weight:	+/- 2000 g
- power:	9V external adapter

- interfacing	USB
- sensor connection	shielded cable with circular connector for WE, Sense (MultiEmStat3+ only), RE and CE.
- external I/O options[2]	analog: 1 input and 1 output channel (both 0 V - 4.096 V) digital: 1 input/output and 3 output lines (maximum rating: -0.3 V to 5.3 V)

Appendix 4: Technical specification of the commercial Pt paste used for the model samples

ESL ELECTROSCIENCE
CERAMIC TAPES & THICK-FILM MATERIALS
416 EAST CHURCH ROAD
KING OF PRUSSIA, PA 19406-2625, U.S.A
T: 610-272-8000
F: 610-272-6759
www.electroscience.com

CO-FIRING POROUS PLATINUM CONDUCTOR 5570

RoHS compliant* conductor designed for use as an electrode in planar sensors

ESL 5570 is designed to be co-fired with partially stabilized zirconia tape at high temperatures.

PASTE DATA

RHEOLOGY:	Thixotropic, screen-printable paste
VISCOSITY: (Brookfield HBT, cone/plate, 38.4 sec^{-1} at 20.0°C ± 0.5°C)	70 ± 20 Pa•s
SHELF LIFE:	6 months

TYPICAL PROPERTIES

SCREEN MESH/EMUSLION:	325 mesh / 25 ± 5 µm
RESISTIVITY: (12.5 µm fired thickness)	30 ± 10 mΩ/square
FIRING RANGE:	1500°C ± 10°C
	see profile on back
TIME AT PEAK TEMPERATURE:	120 min.
SODIUM CONCENTRATION:	≤ 50 ppm
SUBSTRATE OF CALIBRATION:	partially stabilized zirconia tape

Appendix 5: Binary phase diagram of platinum and gold alloy

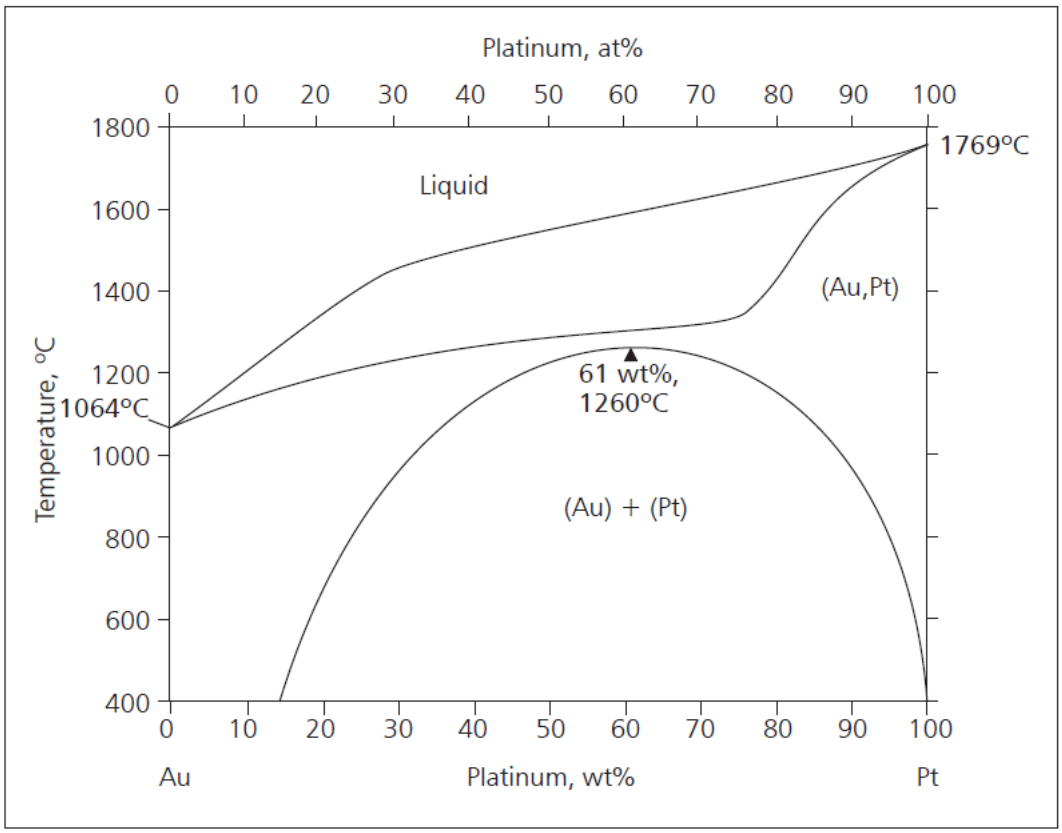

Binary phase diagram of platinum and gold alloy (reproduced from [105])

Declaration

I herewith declare that I have produced this paper without the prohibited assistance of third parties and without making use of aids other than those specified; notions taken over directly or in-directly from other sources have been identified as such. This paper has not previously been presented in identical or similar form to any other German or foreign examination board.

The submitted dissertation has been produced at Karlsruhe University of Applied Sciences and been scientifically supervised by Prof. Dr.rer.nat. habil. Ulrich Guth and Prof. Dr.rer.nat. Heinz Kohler

Date, signature